

Measurement of the $t\bar{t}W$ and $t\bar{t}Z$ Cross Sections
using Proton-Proton Collisions at $\sqrt{s} = 8$ TeV
with the ATLAS Detector

by

Chen Zhou

Department of Physics
Duke University

Date: _____
Approved:

Mark Kruse, Supervisor

Albert Chang

Alfred Goshaw

Roxanne Springer

Stephen Teitsworth

Dissertation submitted in partial fulfillment of the requirements for the degree of
Doctor of Philosophy in the Department of Physics
in the Graduate School of Duke University
April 18, 2016

ABSTRACT

Measurement of the $t\bar{t}W$ and $t\bar{t}Z$ Cross Sections using
Proton-Proton Collisions at $\sqrt{s} = 8$ TeV with the ATLAS
Detector

by

Chen Zhou

Department of Physics
Duke University

Date: _____
Approved:

Mark Kruse, Supervisor

Albert Chang

Alfred Goshaw

Roxanne Springer

Stephen Teitsworth

An abstract of a dissertation submitted in partial fulfillment of the requirements for
the degree of Doctor of Philosophy in the Department of Physics
in the Graduate School of Duke University

April 18, 2016

Copyright © 2016 by Chen Zhou
All rights reserved except the rights granted by the
Creative Commons Attribution-Noncommercial Licence

Abstract

A measurement of the production cross sections of top quark pairs in association with a W or Z boson is presented. The measurement uses 20.3 fb^{-1} of data from proton-proton collisions at $\sqrt{s} = 8\text{ TeV}$ collected by the ATLAS detector at the Large Hadron Collider. Four different final states are considered: two opposite-sign leptons, two same-sign leptons, three leptons, and four leptons. The $t\bar{t}W$ and $t\bar{t}Z$ cross sections are simultaneously extracted using a maximum likelihood fit over all the final states. The $t\bar{t}Z$ cross section is measured to be $176^{+58}_{-52}\text{ fb}$, corresponding to a signal significance of 4.2σ . The $t\bar{t}W$ cross section is measured to be $369^{+100}_{-91}\text{ fb}$, corresponding to a signal significance of 5.0σ . The results are consistent with next-to-leading-order calculations for the $t\bar{t}W$ and $t\bar{t}Z$ processes.

Contents

Abstract	iv
List of Tables	x
List of Figures	xii
Acknowledgements	xvi
1 Introduction	1
1.1 Documentation Outline	3
1.2 Units and Conventions	4
2 The Standard Model	5
2.1 Fundamental Particles	6
2.1.1 Quarks	6
2.1.2 Leptons	7
2.1.3 Bosons	8
2.2 Quantum Chromodynamics	9
2.3 Electroweak Theory	12
2.4 Parton Distribution Functions	19
2.5 Comments on the Standard Model	21
2.6 Standard Model Processes in Dilepton and Multilepton Final States .	24
2.6.1 Drell-Yan Process	24
2.6.2 Diboson Production	25

2.6.3	Top Quark Pair and Single Top Quark Production	26
2.6.4	$t\bar{t}V$ Production	27
2.6.5	Higgs Production	28
2.6.6	Small Processes	29
3	The Large Hadron Collider and ATLAS Experiment	31
3.1	The Large Hadron Collider	31
3.2	The ATLAS Experiment	33
3.2.1	Inner Detector	34
3.2.2	Calorimeter	37
3.2.3	Muon detectors	40
3.2.4	Forward detectors	42
3.2.5	Trigger and Data Acquisition System	43
4	Data and Simulation Samples	46
4.1	Data Samples	46
4.2	ATLAS Simulation Procedure	47
4.2.1	Matrix Element Generators	47
4.2.2	Parton Showering	48
4.2.3	Hadronization	48
4.2.4	Detector Simulation	49
4.2.5	Digitization	49
4.3	Monte Carlo Samples	50
4.3.1	$t\bar{t}V$ Production	50
4.3.2	$W/Z + jets$ Production	51
4.3.3	Diboson Production	51
4.3.4	$t\bar{t}$ and Single Top production	51

4.3.5	Higgs production	52
4.3.6	Small Background Processes	52
5	Object Reconstruction	54
5.1	Tracks	54
5.2	Electrons	56
5.2.1	Electron Reconstruction	56
5.2.2	Electron Selection	57
5.3	Muons	59
5.3.1	Muon Reconstruction	59
5.3.2	Muon Selection	61
5.4	Jets	62
5.4.1	Jet Reconstruction	63
5.4.2	Jet Selection	64
5.5	B-tagging	66
5.6	Missing Transverse Momentum	68
6	Event Selection and Background Estimation	71
6.1	Common Event Selection and Background Estimation	71
6.2	Two Same-sign Lepton Analysis	75
6.2.1	Event Selection	76
6.2.2	Backgrounds from Charge Mis-identification	78
6.2.3	Background from Fake Leptons	83
6.2.4	Control region	89
6.2.5	Grand signal region	96
6.2.6	Further Analysis strategy	103
6.3	Two Opposite-sign Lepton Analysis	107

6.4	Three Lepton Analysis	110
6.5	Four Lepton Analysis	113
7	Systematic Uncertainties	120
7.1	Luminosity Uncertainties	120
7.2	Uncertainties on Reconstructed Objects	121
7.2.1	Lepton Trigger, Reconstruction, and Identification Efficiencies	121
7.2.2	Lepton Momentum Scale and Resolution	121
7.2.3	Jet Reconstruction Efficiencies	122
7.2.4	Jet Vertex Fraction Efficiencies	122
7.2.5	Jet Energy Scale	122
7.2.6	Jet Energy Resolution	123
7.2.7	Flavor Tagging	123
7.2.8	Soft Terms in Missing Transverse Momentum Calculation . . .	124
7.3	Uncertainties on Signal Modeling	124
7.4	Uncertainties on Background Modeling	126
7.4.1	$Z+jets$ Background	126
7.4.2	$t\bar{t}$ Background	127
7.4.3	Single Top Background	127
7.4.4	Diboson Background	127
7.4.5	$t\bar{t}H$ Background	128
7.4.6	tZ and WtZ Backgrounds	129
7.4.7	Other Physics Backgrounds	129
7.4.8	Charge Mis-identification Background	129
7.4.9	Fake Lepton Background	131

8 Results	133
8.1 Statistical Tools	133
8.2 Expected and Observed Event Rates	137
8.3 Cross Section Results	137
9 Conclusion	143
A Feasibility Study of Extending the Global Fit Method to the Three Lepton Final States for the $t\bar{t}V$ Measurements	145
B ATLAS Phase II Inner Tracker Upgrade	151
B.1 Introduction	151
B.2 Simulation and performance of the ATLAS inner tracker	152
B.3 Building silicon module test stands at Duke/ANL	153
B.4 Testing of silicon detectors at CERN	157
C Search for Association Production of an Upsilon Meson with a W or Z Boson at CDF	158
C.1 Introduction	159
C.2 The CDF Detector	160
C.3 Monte Carlo and Data Samples	161
C.4 Event Selection	163
C.5 Backgrounds	168
C.6 Systematic Uncertainties	169
C.7 Results	171
C.8 Conclusions	172
Bibliography	175
Biography	183

List of Tables

1.1	The decay modes of the $t\bar{t}W$ and $t\bar{t}Z$ processes and the corresponding analysis channels	3
2.1	Properties of quarks	7
2.2	Properties of leptons	8
2.3	Properties of bosons	9
2.4	Higgs production cross sections and decay branching ratios	29
4.1	Summary of Monte Carlo samples used in this study	53
6.1	The fake factors with their statistical uncertainties for electrons and muons measured in data, followed by a cross-check conducted with MC	87
6.2	The fake factors with their statistical uncertainties for electrons and muons measured in low- H_T and high- H_T regions using MC samples .	88
6.3	Selected results of the optimization using the $N_{b\text{-jets}} \geq 1$ events . . .	105
6.4	Selected results of the optimization using the $N_{b\text{-jets}} \geq 2$ events . . .	105
6.5	Selected results of the optimization using the $N_{b\text{-jets}} \geq 2$ events and the alternative (tighter cuts) approach	105
8.1	Expected event rates of signals and backgrounds, as well as observed event rates, in all 5 control regions and 15 signal regions used in the likelihood fit	138
8.2	Breakdown of the uncertainties on the measured $t\bar{t}W$ and $t\bar{t}Z$ cross sections	139
8.3	Expected and observed signal significance of the $t\bar{t}W$ and $t\bar{t}Z$ processes from each analysis channel and the combination of all analysis channels	140
A.1	Selected results of the optimization using 3L events with $N_{b\text{-jets}} \geq 1$.	149

A.2	Selected results of the optimization using 3L events with $N_{b\text{-jets}} \geq 2$	149
C.1	Efficiencies for the $(\Upsilon \rightarrow \mu\mu) + (W \rightarrow \ell\nu)$ selection criteria	167
C.2	Efficiencies for the $(\Upsilon \rightarrow \mu\mu) + (Z \rightarrow \ell\ell)$ selection criteria	167
C.3	Systematic uncertainties associated with the signal expectation	171
C.4	Summary of signal expectation (N_{sig}), background estimations (N_{bg}), and observed events (N_{obs})	172
C.5	Cross-section upper limits for ΥW and ΥZ production	173
C.6	Kinematic properties of the muons in the observed $\Upsilon + Z$ candidate	173

List of Figures

2.1	Fundamental particles of the Standard Model	6
2.2	Standard Model coupling vertices	17
2.3	Higgs coupling vertices	18
2.4	$xf(x)$ distributions	20
2.5	Leading-order diagram for the Drell-Yan process	24
2.6	Leading-order diagrams for Diboson production	25
2.7	Leading-order diagrams for $t\bar{t}$ production	26
2.8	Leading-order diagrams for single top production	27
2.9	Example leading-order diagrams for the $t\bar{t}V$ processes	28
3.1	Overall view of the LHC experiments	32
3.2	Cut-away view of the ATLAS detector	33
3.3	Cut-away view of the ATLAS inner detector	35
3.4	Cut-away view of the ATLAS calorimeter	37
3.5	Cut-away view of the ATLAS muon detectors	41
3.6	Schematic view of the ATLAS TDAQ system	43
6.1	The electron charge mis-ID rates with their statistical uncertainties (in %) measured in data	81
6.2	Results of the closure test performed by comparing the same-sign Z peak observed in data with the same-sign Z peak estimated using the data-driven method	82

6.3	The distributions in jet multiplicity for two same-sign lepton final states: ee , $e\mu$, and $\mu\mu$. The events are required to contain at least one b -tagged jet and $H_T < 240$ GeV	90
6.4	The distributions in b -tagged jet multiplicity for two same-sign lepton final states: ee , $e\mu$, and $\mu\mu$. The events are required to contain at least one b -tagged jet and $H_T < 240$ GeV	91
6.5	The distributions in missing transverse momentum for two same-sign lepton final states: ee , $e\mu$, and $\mu\mu$. The events are required to contain at least one b -tagged jet and $H_T < 240$ GeV	92
6.6	The distributions in H_T for two same-sign lepton final states: ee , $e\mu$, and $\mu\mu$. The events are required to contain at least one b -tagged jet and $H_T < 240$ GeV	93
6.7	The distributions in p_T of the first and second leptons for two same-sign electron final states. The events are required to contain at least one b -tagged jet and $H_T < 240$ GeV	94
6.8	The distributions in p_T of the electrons and muons for same-sign $e\mu$ final states. The events are required to contain at least one b -tagged jet and $H_T < 240$ GeV	94
6.9	The distributions in p_T of the first and second leptons for two same-sign muon final states. The events are required to contain at least one b -tagged jet and $H_T < 240$ GeV	95
6.10	The distributions in jet multiplicity for two same-sign lepton final states: ee , $e\mu$, and $\mu\mu$. The events are required to contain at least one b -tagged jet and $H_T > 240$ GeV	97
6.11	The distributions in b -tagged jet multiplicity for two same-sign lepton final states: ee , $e\mu$, and $\mu\mu$. The events are required to contain at least one b -tagged jet and $H_T > 240$ GeV	98
6.12	The distributions in missing transverse momentum for two same-sign lepton final states: ee , $e\mu$, and $\mu\mu$. The events are required to contain at least one b -tagged jet and $H_T > 240$ GeV	99
6.13	The distributions in H_T for two same-sign lepton final states: ee , $e\mu$, and $\mu\mu$. The events are required to contain at least one b -tagged jet and $H_T > 240$ GeV	100

6.14 The distributions in p_T of the first and second leptons for two same-sign electron final states. The events are required to contain at least one b -tagged jet and $H_T > 240$ GeV	101
6.15 The distributions in p_T of the electrons and muons for same-sign $e\mu$ final states. The events are required to contain at least one b -tagged jet and $H_T > 240$ GeV	101
6.16 The distributions in p_T of the first and second leptons for two same-sign muon final states. The events are required to contain at least one b -tagged jet and $H_T > 240$ GeV	102
6.17 Expected and observed contributions in the ee , $e\mu$ and $\mu\mu$ channels of the 2SSL signal regions with the binning used in the final likelihood fit	106
6.18 The NN discriminant distributions in the 2ℓ -no Z -4j, 2ℓ -no Z -5j, 2ℓ - Z -5j signal regions	110
6.19 The discriminant distributions in the 2ℓ -no Z -3j, 2ℓ - Z -3j, 2ℓ - Z -4j control regions	111
6.20 The distribution of the third lepton p_T in the 3ℓ - Z -1b region	113
6.21 The distribution of missing transverse momentum in the 3ℓ -no Z -1b region	114
6.22 The event yields of different lepton flavor combinations in the 3ℓ - Z signal regions	115
6.23 The distributions of the jet multiplicity and b -tagged jet multiplicity in the 4ℓ - ZZ region	117
6.24 The distributions of the jet multiplicity, b -tagged jet multiplicity, $Z1$ invariant mass, and $Z2$ invariant mass in the 4L signal regions	119
8.1 Expected yields after the likelihood fit compared to observed yields in the control regions and signal regions	140
8.2 The measured results of the $t\bar{t}W$ and $t\bar{t}Z$ cross sections compared with the NLO theoretical calculations	141
A.1 The distributions in jet multiplicity for the 3ℓ - Z region and the 3ℓ -no Z region	147
A.2 The distributions in missing transverse momentum for the 3ℓ - Z region and the 3ℓ -no Z region	147

B.1	The letter of intent (LOI) layout for the ITk detector	153
B.2	The d0 resolutions with different non-active material amounts for electrons, muons and pions	154
B.3	The DAQ system setup for the module test stand at Duke	155
B.4	The results of a 3-point gain scan on the ABCN 250nm single readout chip board at Duke	156
B.5	A module test stand at a radiation lab at CERN	157
C.1	Dimuon invariant-mass spectrum in CDF II data from events contained within the low- p_T dimuon-triggered sample	162
C.2	Missing-transverse-energy distributions predicted for signal $\Upsilon + (W \rightarrow \ell\nu)$ events	165
C.3	Transverse-mass distributions predicted for signal $\Upsilon + (W \rightarrow \ell\nu)$ events	166
C.4	Dilepton invariant-mass distribution predicted for signal $\Upsilon + (Z \rightarrow \ell\ell)$ events	166
C.5	Event display of the observed ΥZ candidate, showing the muon candidates identified from the Υ and Z decays	174

Acknowledgements

First of all, I would like to thank my advisor, Prof. Mark Kruse, for his guidance and support during the past six years. Mark is really a kind and bright advisor: I wish to work with him again.

I would also like to thank Dr. Tony Limosani and Dr. Sasha Paramonov. In 2011, my HEP research started with a CDF analysis, for which I worked with Tony. In 2012, I moved to Argonne for 12 months and worked on a ATLAS SUSY analysis with Sasha. For my thesis analysis, both of them assisted me again. I appreciate their help in both physics and life.

I benefit from working in the Duke ATLAS group (Prof. Al Goshaw, Prof. Ashutosh Kotwal, Prof. Ayana Arce, Dr. Doug Benjamin, Dr. Andrea Bocci, Dr. Bo Jayatilaka, Dr. Shu Li, Dr. Enrique Kajomovitz, Dr. Yu Zeng, Dr. Ben Cerio, Dr. Kevin Finelli, Dr. Chris Pollard, Dr. Mia Liu, Lei Li, David Bjergaard, et al.). In addition, I enjoyed my 12 month stay in the Argonne ATLAS group (Dr. Rik Yoshida, Dr. Jimmy Proudfoot, Dr. Larry Nodulman, el al.), as well as my (in total) 18 month stay at CERN.

My research projects would not be successful without the help from people in the ATLAS and CDF collaborations. For my thesis analysis, I thank the analysis team (Kevin, Tony, Sasha, Dr. Markus Cristinziani, el al.) and the reviewers (Prof. Gustaaf Brooijmans, el al.). For the ATLAS SUSY analysis, I thank the analysis team (Sasha, Prof. Jean-Francois Arguin, Dr. David Cote, et al.) and the reviewers

(Dr. Ximo Poveda, et al.). For the CDF analysis, I thank the analysis team (Tony, et al.) and the reviewers (Prof. Robert Harr, Prof. David Toback, et al.). In addition, for my ATALS service task, I thank Prof. Andreas Korn, Dr. Helen Hayward, Dr. Matt Warren, Dr. Bruce Gallop, Dr. Peter Phillips, Dr. Zhijun Liang, Prof. Richard Teuscher, Dr. Susanne Kuehn, Dr. Sergio Diez, Dr. Steve McMahon, and other silicon tracker experts.

Furthermore, I want to thank all the professors, teachers, staff, colleagues, and friends I met in various places. I apologize that I am not able to include all of their names here.

Finally, I would like to thank my family, for their support during my whole life. I would also like to thank my fiancee, Kelly Lin, for her love.

1

Introduction

For centuries, physicists have been pursuing an understanding of the fundamental particles of the universe, and how they interact. The Standard Model is currently the baseline theory of particle physics. However, there exist several outstanding problems with the Standard Model, which may be solved by new physics theories beyond the Standard Model.

The Large Hadron Collider (LHC) at CERN (in Geneva, Switzerland) is the world's most powerful particle collider, with four main particle detectors. During 2010-2012, the LHC was colliding proton-proton beams at a center-of-mass energy of 7 or 8 TeV. The ATLAS detector is one of the particle detectors at the LHC, exploring the outcomes from these proton-proton collisions. The physics goal of the ATLAS experiment is to test the Standard Model, and search for new physics phenomena.

Quarks (up, down, charm, strange, top, and bottom), leptons (electron, muon, tau, and their three associated neutrinos), gauge bosons (W , Z , γ , and gluon), and the Higgs boson are the fundamental particles in the Standard Model. The top quark is the heaviest of all the known fundamental particles. The top quark

was discovered two decades ago, by the CDF and D0 experiments at Fermilab (in Batavia, Illinois). After the discovery, many measurements of top quark properties have been performed, including the top quark pair production cross sections [1], and the top quark mass [2].

However, some of its properties have not been experimentally measured, including its couplings to the Z boson, and the Higgs boson. These couplings are important for the testing of the Standard Model: certain beyond-Standard-Model models, such as the technicolor model [3, 4], can alter these top quark couplings. If these couplings are measured to be significantly different from the Standard Model predictions, it could be an indication for the existence of new physics.

With the center-of-mass collision energy (8 TeV) and integrated luminosity (20.3 fb^{-1}) at the LHC in 2012, top quark pair production in association with a W boson ($t\bar{t}W$), or a Z boson ($t\bar{t}Z$) become experimentally accessible. The $t\bar{t}Z$ cross section provides a direct test of the top quark coupling to the Z boson: some of the $t\bar{t}Z$ production diagrams contain the top- Z -top vertex. Moreover, the $t\bar{t}W$ and $t\bar{t}Z$ processes are major physics backgrounds for the $t\bar{t}H$ measurements, which directly test the top quark coupling to the Higgs boson, as well as many direct searches for new physics phenomena, including supersymmetry and quantum black hole production. Thus, understanding $t\bar{t}W$ and $t\bar{t}Z$ is necessary for these physics programs. The Standard Model predictions for the $t\bar{t}W$ and $t\bar{t}Z$ cross sections have been calculated at the next-to-leading order in terms of the strong coupling constant [5, 6].

This dissertation presents the measurement of the cross sections of the $t\bar{t}W$ and $t\bar{t}Z$ processes with the ATLAS detector. This measurement utilizes the proton-proton (pp) collision data at $\sqrt{s} = 8$ TeV collected by the ATLAS detector in 2012, corresponding to an integrated luminosity of $\int \mathcal{L} dt = 20.3 \text{ fb}^{-1}$. Depending on the decay models of the top quarks, W bosons, and Z bosons, the $t\bar{t}W$ and $t\bar{t}Z$ processes produce events with zero to four leptons (in this study, lepton indicates electron or

muon). The sensitivity of the final states with zero or one lepton does not significantly contribute to this measurement, due to the overwhelming backgrounds for these channels. Thus, four final states are analyzed in this study: two opposite-sign leptons (2OSL), two same-sign leptons (2SSL), three leptons (3L), and four leptons (4L). Most of the sensitivity of the $t\bar{t}W$ measurement comes from the 2SSL and 3L channels, while the $t\bar{t}Z$ sensitivity is mostly due to the 2OSL, 3L, and 4L channels. The decay modes of the $t\bar{t}W$ and $t\bar{t}Z$ processes and the corresponding analysis channels are shown in Table 1.1.

Table 1.1: The decay modes of the $t\bar{t}W$ and $t\bar{t}Z$ processes and the corresponding analysis channels. Here $\ell = e$ or μ .

Process	$t\bar{t}$ decay	Boson decay	Signature
$t\bar{t}W^\pm$	$(\ell^\mp\nu b)(q\bar{q}b)$	$\ell^\pm\nu$	2OSL
	$(\ell^\pm\nu b)(q\bar{q}b)$	$\ell^\pm\nu$	2SSL
	$(\ell^\pm\nu b)(\ell^\mp\nu b)$	$\ell^\pm\nu$	3L
$t\bar{t}Z$	$(\ell^\pm\nu b)(\ell^\mp\nu b)$	$q\bar{q}$	2OSL
	$(q\bar{q}b)(q\bar{q}b)$	$\ell^+\ell^-$	2OSL
	$(\ell^\pm\nu b)(q\bar{q}b)$	$\ell^+\ell^-$	3L
	$(\ell^\pm\nu b)(\ell^\mp\nu b)$	$\ell^+\ell^-$	4L

Finally, the cross sections of the $t\bar{t}W$ and $t\bar{t}Z$ processes are simultaneously extracted using a maximum likelihood fit over all the four channels. The likelihood fit takes all the statistical and systematic uncertainties into account. This study is one of the first published measurements of the $t\bar{t}W$ and $t\bar{t}Z$ cross sections.

1.1 Documentation Outline

This dissertation is organized as follows. Chapter 2 discusses the Standard Model, including the fundamental particles and interactions, as well as the Standard Model processes with final states of two, three, and four leptons. Chapter 3 describes the experimental apparatus: the LHC and the ATLAS detector. Chapter 4 discusses the data and simulation samples used in this study, including the simulation procedure.

Chapter 5 describes how the physics objects are reconstructed and selected. Then, Chapter 6 talks about the event selection used in this study, and Chapter 7 the background estimation. Both Chapter 6 and 7 contain the general analysis strategy for all channels, as well as the specific analysis details for each channel. The author of this dissertation is the main analyzer of the two same-sign lepton (2SSL) channel, so the description of this channel will be more detailed. After Chapter 6 and 7, Chapter 8 explains the systematic uncertainties in this study, including the uncertainties on the reconstruction of physics objects, as well as the modeling of the signals and backgrounds. Chapter 9 talks about the results of this study, such as the $t\bar{t}W$ and $t\bar{t}Z$ cross sections, and how they are extracted. Finally, Chapter 10 gives a conclusion and outlook for this study.

1.2 Units and Conventions

The experimental particle physics uses units based on the Standard International (SI) units. However, with the original SI units, the numerical values of particle physics quantities are often very large or small. Thus, the SI units are modified for more convenient usage, by simply setting the Planck constant (\hbar) and the speed of light (c) to be 1 ($\hbar = c = 1$). These are the so-called “Natural units,” which are also used in this dissertation. One important example is the units of energy, momentum, and mass. A SI unit of energy is electron volt (eV). 1 eV is the energy gained or lost by moving an electron across an electric potential difference of 1 volt. The units of momentum and mass are then both eV, by multiplying by c and c^2 (the original units are eV/c and eV/c^2).

2

The Standard Model

The Standard Model (SM) is currently the baseline theory of fundamental particles and interactions. The fundamental particles of the SM are six quarks (and their anti-particles), six leptons (and their anti-particles), and five bosons (photon, W , Z , gluon, Higgs). The fundamental interactions of the SM are the electromagnetic interaction (mediated by the photon), the weak interaction (mediated by the W and Z bosons), and the strong interaction (mediated by the gluon). Gravity has not yet been able to be incorporated into the SM. The SM is a relativistic quantum field theory and its formulation is derived from the local gauge symmetries. The electromagnetic interaction and weak interaction are unified in the $SU(2) \times U(1)$ electroweak theory, while the strong interaction is described by the $SU(3)$ quantum chromodynamic (QCD) theory. The breaking of the electroweak symmetry is introduced by the Brout-Englert-Higgs mechanism, which predicts the existence of a scalar Higgs boson and gives rise to the masses of the W and Z bosons. The SM works well within the currently attainable energy domain: there has been no experiment or observation that has significantly contradicted the SM's predictions.

2.1 Fundamental Particles

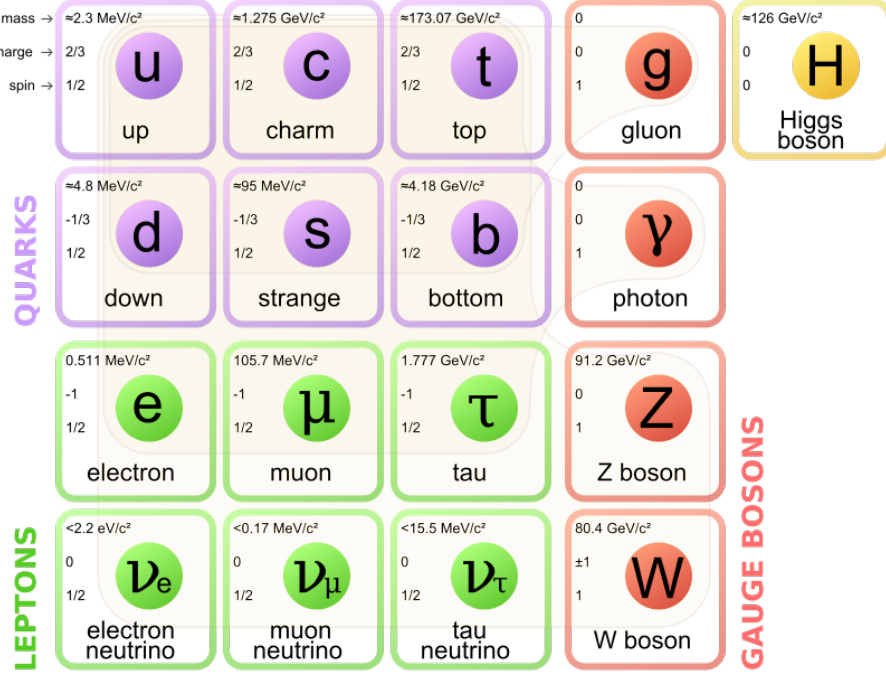


FIGURE 2.1: Fundamental particles of the Standard Model [7]

2.1.1 Quarks

There are six flavors of quarks: up (u), down (d), charm (c), strange (s), top (t), and bottom (b). The six quark flavors are grouped into three generations: the 1st generation (u and d quarks), the 2nd generation (c and s quarks), and the 3rd generation (t and b quarks). All matter is made up of fermions, that is, spin $1/2$ quarks and leptons. The quark masses vary significantly, in a range from several MeV to about 175 GeV [8]. Quarks carry fractional electric charges, which are $+2/3$ for u, c, and t quarks, and $-1/3$ for d, s, and b quarks. Quarks also carry color charge, which is a unique property for quarks, and is the charge on which the strong nuclear force acts. The three possible color charges are red (r), green (g), and blue (b). The properties of quarks are summarized in Table 2.1. In addition, every quark has

its anti-particle (anti-quark), which has the same properties, but opposite electric charge. Considering the flavors, color charges, and anti-quarks, there are $6 \times 3 \times 2 = 36$ types of quarks in total.

Table 2.1: Properties of quarks.

Generation	Flavor	Charge	Mass (GeV)
1st	up	+2/3	2.3×10^{-3}
	down	-1/3	4.8×10^{-3}
2nd	charm	+2/3	1.275
	strange	-1/3	0.095
3rd	top	+2/3	173.2
	bottom	-1/3	4.18

Quarks can not exist freely but only as bound states with other quarks due to color confinement (see section 2.2). Quarks constitute baryons (bound states of three quarks or three anti-quarks, for example protons and neutrons) or mesons (bound states of one quark and one anti-quark). Quarks can interact via the strong, weak, and electromagnetic interactions.

2.1.2 Leptons

There are six flavors of leptons: the charged electron (e), muon (μ), and tau (τ); and their associated neutral neutrinos, the electron neutrino (ν_e), muon neutrino (ν_μ), and tau neutrino (ν_τ). The six leptons are also grouped into three generations: the 1st generation (e and ν_e), the 2nd generation (μ and ν_μ), and the 3rd generation (τ and ν_τ). By convention, electrons, muons, and taus carry -1 electric charge, and their anti-particles +1 electric charge. The neutrinos (ν_e , ν_μ , and ν_τ) are neutral charged particles. The leptons do not carry color charges, and thus do not interact via the strong interaction. The masses of the charged leptons vary from about 0.5 MeV to about 1.8 GeV [8]. The masses of the neutrinos are very small, but have been shown to be non-zero by recent neutrino experiments [9, 10]. The properties

of leptons are summarized in Table 2.2. In addition, every lepton has its anti-particle. Therefore, assuming the anti-particles of the neutrinos are not themselves (Dirac particles), there are $6 \times 2 = 12$ types of leptons in total. However, it might be that the neutrinos are their own anti-particles (Majorana particles). Under that assumption, the number of lepton types will then be 9.

Table 2.2: Properties of leptons.

Generation	Flavor	Charge	Mass (GeV)
1st	e	-1	0.511×10^{-3}
	ν_e	0	$< 2 \times 10^{-9}$
2nd	μ	-1	0.106
	ν_μ	0	$< 2 \times 10^{-9}$
3rd	τ	-1	1.777
	ν_τ	0	$< 2 \times 10^{-9}$

The charged leptons interact via the weak interaction and the electromagnetic interaction. But the neutrinos (not having electric charge) interact via only the weak interaction. The electrons can form atoms with protons and neutrons (which themselves are made up of up and down quarks). The atoms constitute almost all observable matter in the universe.

2.1.3 Bosons

There are five basic types of bosons: the photon (γ), W , Z , gluon (g), and Higgs (H). The first four bosons are the force mediators: the photon mediates the electromagnetic interaction, the W and Z bosons mediate the weak interaction, and the gluon mediates the strong interaction. The Higgs boson results from the electroweak symmetry breaking in the SM.

The force mediators are all spin-1 vector bosons and the Higgs boson is a spin-0 scalar boson. The W boson carries ± 1 electric charge, while all the other bosons are neutral charged particles. The gluon (as a consequence of mediating the strong

Table 2.3: Properties of bosons.

	Interaction	Spin	Charge	Mass (GeV)
photon	Electromagnetic	1	0	0
W	Weak	1	± 1	80.4
Z	Weak	1	0	91.2
gluon	Strong	1	0	0
Higgs	-	0	0	125.7

interaction) is a color octet with 8 distinct color combination states. The photon and gluon are the only massless bosons, with the other bosons all having masses around 100 GeV [8]. The properties of bosons are summarized in Table 2.3. Considering the electric charge of the W boson and the color states of the gluon, there are $1+2+1+8+1 = 13$ bosons in total.

2.2 Quantum Chromodynamics

Quantum Chromodynamics (QCD) is the Standard Model theory for the strong interaction among quarks and gluons. The strong interaction is one of the fundamental interactions and is mediated by gluons.

Color is one of the most important concepts in QCD. Color, or color charge, is the QCD analogue of the electric charge. There are three color charges in QCD, named as red (r), green (g), and blue (b). Every quark (antiquark) carries one color (anticolor) charge. Gluons are bi-colored, having color-anticolor states. The three color charges provide nine independent color-anticolor states: one singlet state $((r\bar{r} + g\bar{g} + b\bar{b})/\sqrt{3})$ and eight octet states. The singlet state is colorless and not able to mediate the short-range strong interaction. Therefore, there are 8 possible gluons in nature.

The strong interaction is fully determined by the QCD Lagrangian, that is

$$\mathcal{L}_{QCD} = -\frac{1}{4}(F_{\mu\nu})_a(F^{\mu\nu})_a + \bar{\psi}_j(i\gamma^\mu(D_\mu)_{jk} - m\delta_{jk})\psi_k$$

(2.1)

The first term describes the propagation of the gluon fields, while the second term describes the interactions of quarks with the gluon fields.

The details about the QCD Lagrangian are discussed as follows, with Equation 2.2 to Equation 2.7.

In the QCD Lagrangian, $(F_{\mu\nu})_a$ is the field tensor of gluons

$$(F_{\mu\nu})_a = \partial_\mu G_\nu^a - \partial_\nu G_\mu^a - g_s f_{abc} G_\mu^b G_\nu^c$$

(2.2)

and $(D_\mu)_{jk}$ is the covariant derivative

$$(D_\mu)_{jk} = \delta_{jk}\partial_\mu + ig_s(T_a)_{jk}G_\mu^a$$

(2.3)

Furthermore, ψ_k is the spinor wave function of a quark with a specific flavor and color k . k can be r, b, or g. ψ_k forms a 3 component column vector ψ for the quark flavor, and $\bar{\psi}$ is defined as $\psi^+ \gamma^0$, a row vector.

$$\Psi = \begin{pmatrix} \psi_r \\ \psi_b \\ \psi_g \end{pmatrix}$$

(2.4)

G_μ^a is the gluon field with color structure a . μ can be 1-4, corresponding to the indices of the spacetime 4-vectors. a can be 1-8, corresponding to the eight gluon color structures.

g_s is the strong coupling constant. γ^μ is the gamma matrices. T_a is the eight 3×3 generator matrices of the SU(3) group. f_{abc} is defined from the commutation relations of T_a :

$$[T_a, T_b] = if_{abc}T_c$$

(2.5)

It can be shown that, the QCD Lagrangian is invariant under the SU(3) transformation:

$$\psi \rightarrow [1 - ig_s\alpha_a(x)T_a]\psi \quad (2.6)$$

$$G_\mu^a \rightarrow G_\mu^a + \partial_\mu\alpha_a(x) + g_s f_{abc}\alpha_b(x)G_\mu^c \quad (2.7)$$

where $\alpha_a(x)$ is eight arbitrary functions of spacetime.

In fact, the formula of the QCD Lagrangian is obtained by requiring its invariance under the SU(3) transformation. Therefore, the QCD theory is regarded as a (local) SU(3) gauge theory.

Starting from the QCD Lagrangian, we can calculate all the strong interaction couplings, that are qqg coupling, ggg coupling, and gggg coupling, shown in Figure 2.2. The qqg coupling, changing the quark color charge by a gluon, is introduced by the second term (the fermion part) of Equation 2.1. The ggg coupling and gggg coupling, that are gluon self interactions, are introduced by the first term (the field part) of Equation 2.1.

The strong interaction has several features:

- Color confinement

No free quark has been observed. They are only observed in bound states such as baryons and mesons, which are colorless. This is because the strong force increases when the distance between quarks gets larger. Therefore, when separating two quarks, it costs less energy to create a new quark-antiquark pair, than allowing the two original quarks to be separated further.

- Asymptotic freedom

The coupling constant of the strong interaction varies with the energy (Q) used to evaluate the coupling. The evolution of the coupling constant with the

energy can be predicted by QCD. To the lowest order, the coupling constant is

$$\alpha_s(Q) = \frac{4\pi}{(11 - \frac{2}{3}n_f)\ln(Q^2/\Lambda^2)} \quad (2.8)$$

where n_f is the number of quark flavors and Λ is a constant in QCD. At high energies, the coupling strength becomes weaker and the perturbative calculations provide precise predictions. While at low energies, the coupling strength becomes stronger and the perturbative calculations are no longer usable.

2.3 Electroweak Theory

The other two fundamental interactions, the weak interaction and the electromagnetic interaction, is unified and described by the Standard Model electroweak (EWK) theory. The weak interaction is mediated by the W and Z bosons, while the electromagnetic interaction is mediated by the photon. In addition, the electroweak symmetry breaking is provided by the Brout-Englert-Higgs mechanism, without which the W and Z bosons would have zero mass.

The Lagrangian of the SM electroweak theory (without the Yukawa coupling terms) is

$$\begin{aligned} \mathcal{L}_{EWK} = & -\frac{1}{4}B_{\mu\nu}B^{\mu\nu} - \frac{1}{4}W_{\mu\nu} \cdot W^{\mu\nu} + \bar{\psi}(i\gamma^\mu D_\mu)\psi \\ & + (D_\mu\phi^+)(D^\mu\phi) - [-\mu^2\phi^+\phi + \lambda(\phi^+\phi)^2] \end{aligned} \quad (2.9)$$

The first and second terms describe the propagation of the fields of the photon, W boson, and Z boson, while the third term is about the EWK interactions of fermions with the fields. In addition, the fourth term describes the propagation of the Higgs boson (which breaks the electroweak symmetry), while the last term is the Higgs potential term.

The details about the EWK Lagrangian are discussed as follows, with Equation 2.10 to Equation 2.35.

In the EWK Lagrangian, D_μ is the covariant derivative

$$D_\mu = \partial_\mu + ig(W_\mu^+ T_L^+ + W_\mu^- T_L^-) + ig_z Z_\mu (T_{3L} - \sin^2(\theta_W) Q) + ie Q A_\mu \quad (2.10)$$

Furthermore, e , g , and g_z are the coupling constants and θ_W is the electroweak mixing angle. They are related by

$$g = e / \sin(\theta_W) \quad (2.11)$$

$$g_z = e / (\sin(\theta_W) \cos(\theta_W)) \quad (2.12)$$

T_1 , T_2 , T_3 are the three 2×2 generator matrices of the SU(2) group. T^+ and T^- are then defined as

$$T^\pm = (T_1 \pm iT_2) / 2^{1/2} \quad (2.13)$$

T_L^+ is defined as

$$T_L^+ = T^+ [1/2(1 - \gamma^5)] \quad (2.14)$$

and T_L^- and T_{3L} have similar notations.

Q is the electric charge operator. Y , the hypercharge operator, is then defined using

$$Q = T_{3L} + Y/2 \quad (2.15)$$

$B_{\mu\nu}$ and $W_{\mu\nu}$ are the field tensors in the electroweak theory, as

$$B_{\mu\nu} = \partial_\mu B_\nu - \partial_\nu B_\mu \quad (2.16)$$

$$W_{\mu\nu} = \partial_\mu W_\nu - \partial_\nu W_\mu - g W_\mu(x) \times W_\nu(x) \quad (2.17)$$

B_μ and W_μ (including $W_{1\mu}$, $W_{2\mu}$, and $W_{3\mu}$) are the four electroweak fields. μ can be 1-4, corresponding to the indices of the spacetime 4-vectors.

We then further define W^+ , W^- , Z and A fields as

$$W^\pm = (W_1 \mp iW_2)/2^{1/2} \quad (2.18)$$

$$Z = \cos(\theta_W)W_3 - \sin(\theta_W)B \quad (2.19)$$

$$A = \sin(\theta_W)W_3 + \cos(\theta_W)B \quad (2.20)$$

ψ is the wave function of the fermions, as a weak isospin doublet. There are six weak isospin doublets in total:

$$\psi = \begin{pmatrix} \nu_e \\ e^- \end{pmatrix}, \begin{pmatrix} \nu_\mu \\ \mu^- \end{pmatrix}, \begin{pmatrix} \nu_\tau \\ \tau^- \end{pmatrix} \quad (2.21)$$

and

$$\psi = \begin{pmatrix} u \\ d' \end{pmatrix}, \begin{pmatrix} c \\ s' \end{pmatrix}, \begin{pmatrix} t \\ b' \end{pmatrix} \quad (2.22)$$

The neutrinos and the up-type quarks have $+1/2$ weak isospin, while the charged leptons and the down-type quarks have $-1/2$ weak isospin. $\bar{\psi}$ is defined as $\psi^+\gamma^0$.

d' , s' , and b' are the weak eigenstates of quarks, and they are related to the mass eigenstates of quarks (d , s , and b) by a 3×3 Cabibbo-Kobayashi-Maskawa (CKM) matrix, as

$$\begin{pmatrix} d' \\ s' \\ b' \end{pmatrix} = \begin{pmatrix} V_{ud} & V_{us} & V_{ub} \\ V_{cd} & V_{cs} & V_{cb} \\ V_{td} & V_{ts} & V_{tb} \end{pmatrix} \begin{pmatrix} d \\ s \\ b \end{pmatrix} \quad (2.23)$$

Although the CKM matrix has nine complex elements, it has only 4 free real parameters.

ϕ is a weak doublet of the complex Higgs fields.

$$\phi = \begin{pmatrix} [\phi_1(x) + i\phi_2(x)]/2^{1/2} \\ [\phi_3(x) + i\phi_4(x)]/2^{1/2} \end{pmatrix} \quad (2.24)$$

μ and λ are the two parameters to describe the potential of the fields.

It can be shown that, the EWK Lagrangian is invariant under the SU(2) transformation:

$$\psi_L \rightarrow [1 - ig\alpha(x) \cdot T]\psi_L \quad (2.25)$$

$$\psi_R \text{ unchanged} \quad (2.26)$$

$$B_\mu \text{ unchanged} \quad (2.27)$$

$$W_\mu(x) \rightarrow W_\mu(x) + \partial_\mu\alpha(x) + g\alpha(x) \times W_\mu(x) \quad (2.28)$$

where ψ_L (ψ_R) is the left-handed (right-handed) part of ψ , and $\alpha(x)$ are three arbitrary functions of spacetime.

It is also invariant under the U(1) transformation:

$$\psi \rightarrow [1 - \frac{i}{2}(g \sin(\theta_W)/\cos(\theta_W))\beta(x)Y]\psi \quad (2.29)$$

$$B_\mu \rightarrow B_\mu + \partial_\mu\beta \quad (2.30)$$

$$W_\mu(x) \text{ unchanged} \quad (2.31)$$

where $\beta(x)$ is an arbitrary function of spacetime.

The formula of the EWK Lagrangian is also obtained by requiring its invariance under the SU(2) and U(1) transformation. Therefore, the electroweak theory is regarded as a (local) $SU(2) \times U(1)$ gauge theory.

Furthermore, we can choose specific $\alpha_i(x)$ of the SU(2) transformation to eliminate ϕ_1 , ϕ , and ϕ_3 . Then ϕ can be written as

$$\phi = \begin{pmatrix} 0 \\ [v + H(x)]/2^{1/2} \end{pmatrix} \quad (2.32)$$

where v is $(\mu^2/\lambda)^{1/2}$.

From the fourth and fifth terms of Equation 2.9, we can identify the masses for the W , Z , and Higgs bosons, which are

$$m_W = gv/2 \quad (2.33)$$

$$m_Z = gzv/2 \quad (2.34)$$

$$m_H = (2\mu^2)^{1/2} \quad (2.35)$$

The masses of the fermions are produced by adding terms of the Yukawa coupling of fermions with the Higgs field, to the EWK Lagrangian. The Yukawa coupling terms are determined by the fermion doublets, the Higgs doublet, and the fermion masses. After adding the Yukawa coupling terms, the EWK Lagrangian is still invariant under the previous $SU(2)$ and $U(1)$ transformations. In this way, the fermion mass terms can then be identified in the Lagrangian.

Starting from the EWK Lagrangian, we can calculate all the weak and electromagnetic interaction couplings, shown in Figure 2.2 and Figure 2.3. There exists the ffW (weak charged current), ffZ (weak neutral current), and $ff\gamma$ (electromagnetic) couplings, corresponding to the second, third, and fourth terms of Equation 2.10, derived from the third term of Equation 2.9. There also exist the triple and quartic couplings among the W , Z , and γ bosons, derived from the first and second terms of Equation 2.9.

In addition, the fourth and fifth terms of Equation 2.9 predict the couplings of the Higgs boson to the gauge bosons and its self couplings, which include the HWW , HZZ , HHH , $HHWW$, $HHZZ$, and $HHHH$ couplings. The Yukawa coupling terms also predict the Higgs-fermion-fermion couplings, which are proportional to the fermion masses.

Standard Model Interactions (Forces Mediated by Gauge Bosons)

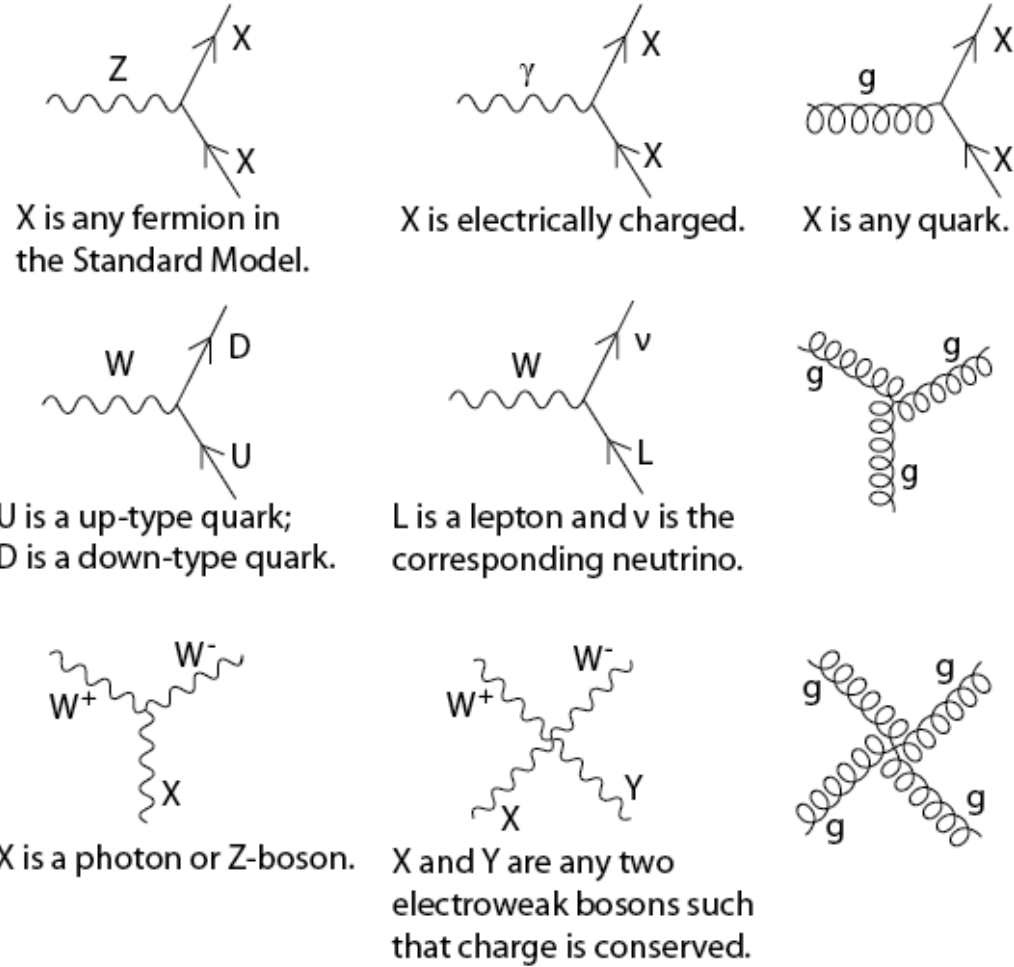


FIGURE 2.2: Standard Model coupling vertices, mediated by gauge bosons [7]. The first column includes the ffZ , qqW , and $WWZ(\gamma)$ couplings (from top to bottom). The second column includes the $ff(WW)\gamma$ coupling, $Wl\nu$ coupling, and quartic couplings among the electroweak gauge bosons (from top to bottom). The third column includes the strong interaction couplings: qgq , ggg , $gggg$ (from top to bottom).

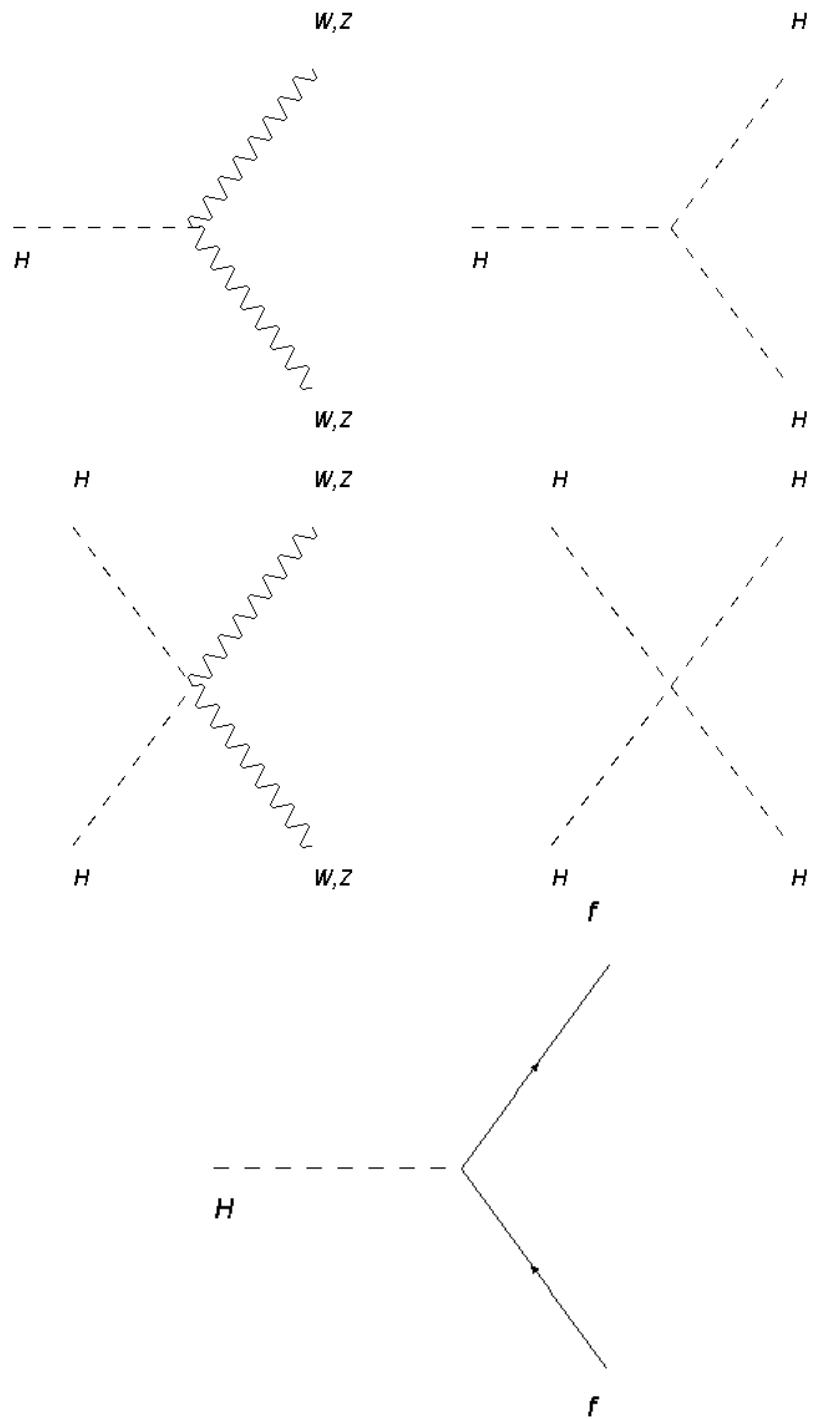


FIGURE 2.3: Higgs coupling vertices. The first row includes the $HWW(ZZ)$ and HHH couplings. The second row includes the $HHWW(ZZ)$ and $HHHH$ couplings. The third row includes the Hff couplings.

2.4 Parton Distribution Functions

Using the knowledge of the QCD and electroweak theories, we can calculate the differential cross sections using partons (quarks and gluons) as initial state particles. However, quarks and gluons are not free particles and the current experiments typically collide hadrons like protons, which consist of several quarks and gluons. To make prediction for the experimental results, differential cross sections using hadrons as initial state particles should be calculated, and the flux of the quarks and gluons in the hadrons needs to be known.

In the hadron collider experiments, the hadrons are usually accelerated to a specific momentum. The momentum is actually carried by the quarks and gluons in the hadrons. Let x_i be the fraction of the total momentum carried by the i -th parton, we have

$$\sum_i x_i = 1 \quad (2.36)$$

Furthermore, we define $f(x)$ to be the number density of momentum fraction x for parton flavor f , which are called parton distribution functions (PDFs). f can be $u, \bar{u}, d, \bar{d}, s, \bar{s}, c, \bar{c}, b, \bar{b}, t, \bar{t}$, and g (for gluons).

Then, the previous equation turns into

$$\int_0^1 dx x \sum_a f_a(x) = 1 \quad (2.37)$$

PDFs are usually extracted from experimental measurements, by fitting the parameters of PDFs to the data from several experiments. There exist several working sets of PDFs, such as the ones provided by the MSTW collaboration [11] and the CTEQ collaboration [12], all of which are an approximation of the true PDFs. Distributions of $xf(x)$ for each parton flavor, provided by the MSTW collaboration, are

shown in Figure 2.4.

An important feature of the PDFs is that, they depend not only on the flavor of the parton, but also on the probe energy, Q . The evolution of the PDFs with the probe energy can be calculated by the QCD theory. Thus, we can measure the PDFs using a specific probe energy and extrapolate to the needed energy.

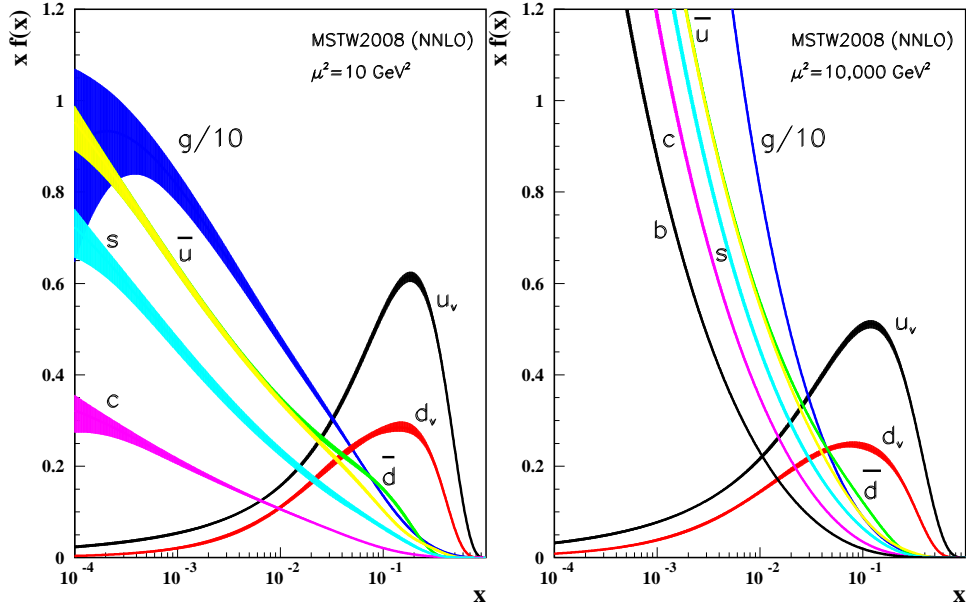


FIGURE 2.4: Distributions of $xf(x)$ for each parton flavor [8], provided by the MSTW collaboration.

With the working PDFs, we can calculate the differential cross sections of interest in hadron collider experiments, by first calculating the parton level differential cross sections, and then integrating over the parton flux given by the PDFs. Therefore, we are able to compare the experimental measurements with the theoretical calculations. However, the limited precision of PDFs is usually the major source of the theoretical calculation uncertainty.

2.5 Comments on the Standard Model

The Standard Model is an extremely successful theory. Within the currently attainable energy domain, there has been no experiment or observation that has significantly contradicted the SM’s predictions. Taking the collider experiments as an example, by the time of writing this thesis, all of the measurements of the SM processes agree with the theoretical calculations (considering the theoretical and experimental uncertainties), and none of the theorized beyond-Standard-Model (BSM) processes have been observed. Besides, all of the SM fundamental particles have now presumably been discovered. Most recently, the top quark was discovered by the CDF and D0 experiments at Fermilab in 1995 [13, 14], the ν_τ lepton by the DONUT experiment at Fermilab in 2000 [15], and the Higgs boson by the ATLAS and CMS experiments at CERN in 2012 [16, 17].

However, although the SM is successful, there exist some serious problems with the theory:

- Hierarchy problem:

The Planck energy scale (10^{19} GeV) and the electroweak symmetry breaking scale (100 GeV) are very different. One consequence of the Hierarchy problem is a predicted divergence of the Higgs mass. Certain one-loop diagrams, which contain the couplings between a fermion and the Higgs boson with a $-\lambda_f H \bar{f} f$ term in the Lagrangian can yield a correction of the Higgs mass as

$$\Delta m_h^2 = -(1/8\pi^2) |\lambda_f|^2 \Lambda_{UV}^2 \quad (2.38)$$

Λ_{UV} is a momentum cutoff used in the loop integral, and its value should be comparable with the Planck energy scale. Thus, the SM Higgs mass diverges after this correction, which requires further “fine tuning.”

- Grand unification:

The electroweak and strong interactions are not unified in the SM. To describe them, we need to utilize two different sets of Lagrangians. In addition, the coupling strength constants of the strong, weak, and electromagnetic interactions vary with the probe energy. The theoretical calculation shows that the three constants will not converge at any probe energy. The inability of unifying the electroweak and strong interactions at some higher energy than the currently attainable makes the SM an “unnatural” theory.

- Gravity:

Gravity is one of the fundamental interactions in the universe, which is an attractive force between two physics objects. In modern physics, gravity is described by the theory of general relativity: the 3-dimentional space and 1-dimensional time are combined to form a 4-dimentional spacetime, which is distorted by the masses of all objects. Therefore, gravity is a geometric effect of mass. In the view of the SM, every macroscopic force is the result of fundamental interactions among the fundamental particles. Physicists have tried to describe gravity like the other three fundamental interactions, through the exchange of a graviton (a spin-2 boson) between fundamental particles. However, this kind of efforts fail in the technical details of completing the description. Therefore, the SM has not been able to incorporate gravity.

- Dark matter and dark energy:

Astrophysical and cosmological observations have shown that, dark matter and dark energy account for about 95% of the mass/energy of the universe. However, the SM has no candidate for dark matter or explanation for dark energy. One BSM candidate of dark matter is the Weakly Interacting Massive

Particles (WIMP), which interact only via the weak interaction and gravity [18].

There are prospects for its detection in the near future.

Therefore, the SM should not be the ultimate theory of the fundamental particles and fields. There are several extensions of the SM, aiming to solving the problems of the SM. Below is some of the possible theorized extensions.

- Supersymmetry

Supersymmetry (SUSY) requires the symmetry of the transformation which turns a boson into a fermion, and vice versa (changing a particle's spin by $\frac{1}{2}$).

The SM particle and its transformed analog are called superpartners. SUSY is able to solve the Hierarchy problem, and include gravity and dark matter in the theoretical framework. However, none of the many additional SUSY particles have been discovered.

- Grand Unification Theories

Grand Unification Theories (GUTs) unify the strong and electroweak interactions. In GUTs, the SM symmetry groups ($SU(3)$ and $SU(2) \times U(1)$) are subgroups of a larger symmetry group (which can be $SU(5)$, $SO(10)$, $E6$, etc). GUTs predict more quarks and leptons, as well as new heavy bosons like W' and Z' . GUTs also predict baryon number violation, which can result in proton decay. However, no such phenomena predicted by GUTs have been observed.

- String Theory

String theory regards the fundamental particles as strings, rather than points. String theory needs a 10-dimension space and is able to derive the current quantum field theory after compacting the space to 4 dimensions. One difficulty of string theory is to design experiments to test the theory.

2.6 Standard Model Processes in Dilepton and Multilepton Final States

The measurement of $t\bar{t}V$ cross sections at ATLAS is performed using events with two, three, or four charged leptons. Several Standard Model processes are able to produce such events, which are discussed in this section.

2.6.1 Drell-Yan Process

In the Drell-Yan process [19], a quark and an anti-quark annihilate to create a virtual photon (γ^*) or Z boson, which decays into a pair of opposite-charged same-flavor leptons. In terms of the dilepton mass, the contribution through a Z boson peaks around 91 GeV (the Z boson mass), while the contribution through a γ^* dominates in the low mass region. The leading-order diagram for the Drell-Yan process is shown in Figure 2.5. The cross section of the Drell-Yan process at $\sqrt{s} = 8$ TeV is calculated at NNLO (next-to-next-to-leading order) [20], which is $\sigma(pp \rightarrow Z/\gamma^* \rightarrow \ell^+\ell^-) = 1122$ pb, where ℓ refers to only one lepton flavor. For a specific calculation of this process, a mass range needs to be given. Here $66 \text{ GeV} < m_{\ell\ell} < 116 \text{ GeV}$ is used.

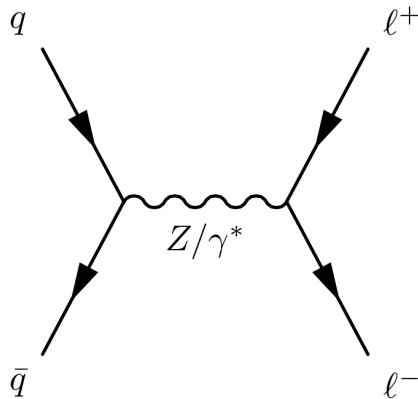


FIGURE 2.5: Leading-order diagram for the Drell-Yan process.

In the Drell-Yan process, ℓ can be an electron, muon, or tau lepton. In collider experiments, electrons and muons are regarded as stable particles, while tau leptons

decay before entering the inner detector. A tau lepton can decay to an electron or muon, an electron, muon or tau neutrino, with a branching ratio of about 17% each. Otherwise it decays hadronically. Therefore, the Drell-Yan process is able to produce opposite-charged ee , $\mu\mu$, and $e\mu$ events, although the $e\mu$ events are less likely than ee or $\mu\mu$. When studying ee and $\mu\mu$ final states, the Drell-Yan process is usually the dominant process.

2.6.2 Diboson Production

Diboson production includes the W^+W^- , WZ , and ZZ processes. The leading-order diagrams for those processes are shown in Figure 2.6. The leading-order diagrams are separated into the t-channel, u-channel, and s-channel, for all of the three processes. The s-channel diagrams contain the triple gauge boson coupling vertex. Both the WZ and ZZ processes include contributions of virtual photons. The cross sections at $\sqrt{s} = 8$ TeV of the diboson processes are calculated at NLO (next-to-leading order) [21], which are $\sigma(WW) = 54.71$ pb, $\sigma(WZ) = 33.31$ pb, and $\sigma(ZZ) = 11.17$ pb, where a cut of $m_{Z/\gamma^*} > 12$ GeV is applied. At the currently attainable collision energies, $\sigma(WW) > \sigma(WZ) > \sigma(ZZ)$.

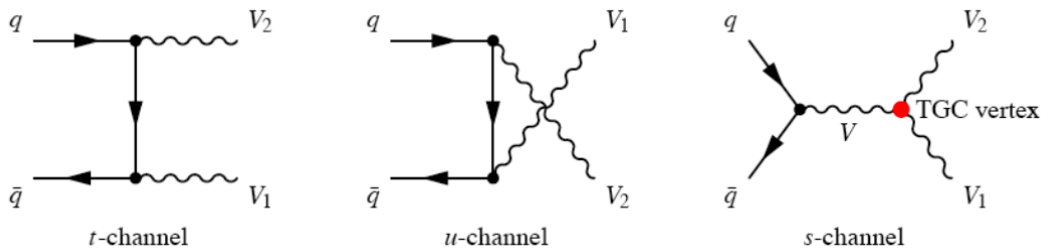


FIGURE 2.6: Leading-order diagrams for Diboson production. V , V_1 , V_2 can be a W or Z boson.

A W boson can decay to an electron, muon, or tau lepton, and the associated neutrino, with a branching ratio of about 11% each. Otherwise, it decays hadronically

(to an up-type quark and a down-type quark). A Z boson can decay to a pair of opposite-charged electrons, muons, or tau leptons, with a branching ratio of about 3.4% each. It can also decay to a pair of neutrinos with a branching ratio of about 20%. Otherwise, it decays hadronically (to a quark and its antiquark). Therefore, the W^+W^- production is able to produce events with two opposite-charged leptons. The WZ production is able to produce events with two or three leptons. In addition, the ZZ production is able to produce events with two, three, or four leptons.

2.6.3 Top Quark Pair and Single Top Quark Production

Top quark pair production originates from gluon-gluon fusion and quark-antiquark annihilation. At the LHC, the gluon-gluon fusion mechanism dominates. The leading-order diagrams for top quark pair production are shown in Figure 2.7. The $t\bar{t}$ cross section at $\sqrt{s} = 8$ TeV is calculated at NLO [22, 23], to be $\sigma(t\bar{t}) = 252.9$ pb, where the top quark mass is set at 172.5 GeV.

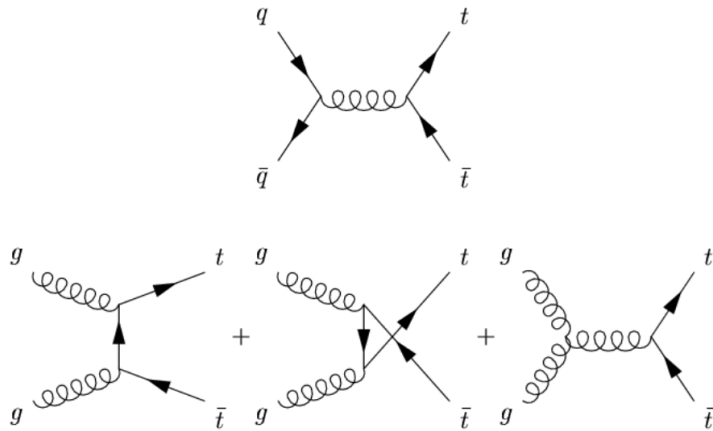


FIGURE 2.7: Leading-order diagrams for $t\bar{t}$ production.

Due to the large V_{tb} parameter in the CKM matrix (almost 1), the top quark decays to a W boson and a b quark at almost 100%. Therefore, the final state of top quark pair production is similar to that of W^+W^- production, except for the

existence of two b quarks. Inclusively, the two W bosons from the top quark pair can decay dileptonically ($\ell^+\nu\ell^-\nu$), semileptonically ($\ell\nu jj$), or hadronically ($jjjj$).

Single top production can be achieved through the s-channel, t-channel, and Wt channel. The leading-order diagrams for single top production are shown in Figure 2.8. The s-channel and t-channel produce events with at most one charged lepton. Only the Wt channel is able to produce events with two charged leptons, from the leptonic decay mode of two W bosons (one W boson is from the top quark decay). The Wt cross section at $\sqrt{s} = 8$ TeV is calculated at NLO [24], to be $\sigma(Wt) = 22.37$ pb, where the top quark mass is set at 172.5 GeV.

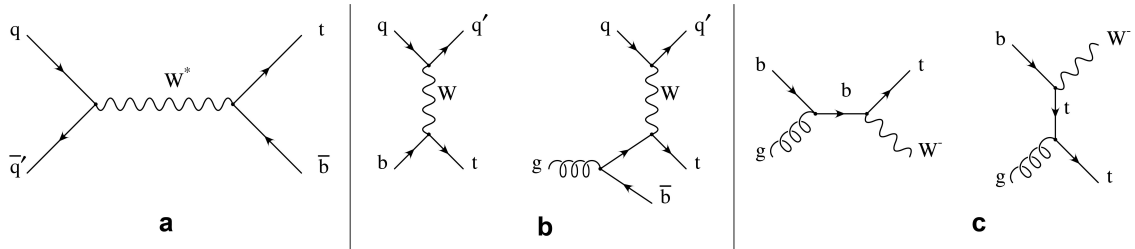


FIGURE 2.8: Leading-order diagrams for single top production. The left diagram corresponds to the s-channel. The middle diagrams correspond to the t-channel. The right diagrams correspond to the Wt channel.

The final state of Wt production is similar to that of W^+W^- production, except for the existence of one b quark. Thus, Wt production is also able to produce events with two opposite-charged leptons.

2.6.4 $t\bar{t}V$ Production

The production of a top quark pair in association with a vector boson, $t\bar{t}V$, includes both the $t\bar{t}W$ and $t\bar{t}Z$ processes. The $t\bar{t}Z$ process has contributions of virtual photons in the final state. Example leading-order diagrams for these processes are shown in Figure 2.9. The $t\bar{t}W$ process is achieved by radiating a W boson from an initial state parton (shown on the left of Figure 2.9). The $t\bar{t}Z$ process can use this same

production mechanism, and can also be achieved by radiating a Z boson from a final state top quark (shown on the right of Figure 2.9). This latter production mechanism for $t\bar{t}Z$ is sensitive to the top- Z coupling. The cross sections of the $t\bar{t}V$ processes at $\sqrt{s} = 8$ TeV are calculated at NLO [5, 6] to be $\sigma(t\bar{t}W) = 0.232 \pm 0.32$ pb, $\sigma(t\bar{t}Z) = 0.215 \pm 0.30$ pb, where a requirement of $m_{Z/\gamma^*} > 5$ GeV is applied. The uncertainties include renormalization and factorization scale uncertainties, and PDF uncertainties. The calculated $t\bar{t}W$ and $t\bar{t}Z$ cross sections are of the same order, and significantly smaller than the $t\bar{t}$ cross section.

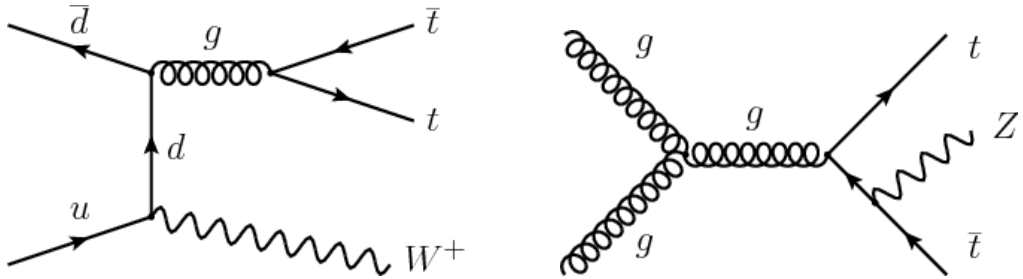


FIGURE 2.9: Example leading-order diagrams for the $t\bar{t}V$ processes.

Considering the decay modes of top quark, W boson, and Z boson, the $t\bar{t}W$ process can result in final states with two or three leptons, and the $t\bar{t}Z$ process can result in final states with two, three, or four leptons. The final states of both processes have at least two b quarks as well. The top quark and W/Z boson decay modes associated with these final states are summarized in Table 1.1.

2.6.5 Higgs Production

The SM Higgs boson was discovered by the ATLAS and CMS experiments in 2012, and its mass measured to be about 125 GeV. Processes involving the Higgs boson need to be considered in this study.

Five Higgs production modes are currently considered at the LHC. The leading production mode at the LHC is gluon-gluon fusion through a heavy-quark loop to

produce a Higgs Boson ($gg \rightarrow H$). The subleading production modes include Higgs boson production through vector boson fusion (VBF), associated production of a Higgs boson with a W boson (WH), associated production of a Higgs boson with a Z boson (ZH), and associated production of a Higgs boson with a top quark pair ($t\bar{t}H$). Setting the Higgs mass at 125 GeV, the cross sections of the above Higgs production modes at $\sqrt{s} = 8$ TeV are calculated to the NNLO in QCD with NLO EWK corrections [25], and shown in Table 2.4.

Table 2.4: Higgs production cross sections and decay branching ratios. The Higgs mass is set at 125 GeV.

production mode	$gg \rightarrow H$	VBF Higgs	WH	ZH	$t\bar{t}H$
cross section	19.27 pb	1.578 pb	0.7046 pb	0.4153 pb	0.1293 pb
decay mode	$H \rightarrow bb$	$H \rightarrow WW$	$H \rightarrow ZZ$	$H \rightarrow gg$	$H \rightarrow \tau\tau$
branching ratio	57.7%	21.6%	2.66%	8.55%	6.37%
decay mode	$H \rightarrow c\bar{c}$	$H \rightarrow \gamma\gamma$	$H \rightarrow Z\gamma$		
branching ratio	2.67%	0.23%	0.16%		

The Higgs boson decays almost instantaneously via various decay modes. Setting the Higgs mass at 125 GeV, the leading decay mode is $H \rightarrow b\bar{b}$, and the subleading decay modes are $H \rightarrow WW$, $H \rightarrow ZZ$, $H \rightarrow gg$, $H \rightarrow \tau\tau$, $H \rightarrow c\bar{c}$, $H \rightarrow \gamma\gamma$, and $H \rightarrow Z\gamma$. The branching ratios of the above Higgs decay modes are also shown in Table 2.4. Considering various decay modes of the Higgs boson, all the five Higgs production modes are able to produce events with two or more charged leptons.

2.6.6 Small Processes

There are several additional processes that we consider for this analysis. Their cross sections are smaller than other processes, although their contributions might be important in certain kinematic regions.

The production of a single top in association with a Z boson can occur through the t-channel, s-channel, and WtZ channel diagrams. The cross section at $\sqrt{s} = 8$ TeV,

calculated to NLO [26], is $\sigma(tZ) = 0.236$ pb, including both t and \bar{t} contributions. The tZ production is able to contribute to the final states with two or three leptons. In this analysis, the contribution of tZ is smaller than $t\bar{t}Z$, due to the kinematic features and selection requirements.

The production of two same-sign W bosons ($W^\pm W^\pm$) includes pure electroweak diagrams with sixth-order electroweak couplings (α_{EW}^6), as well as QCD mediated diagrams with fourth-order electroweak couplings and second-order QCD couplings ($\alpha_{EW}^4 \alpha_s^2$). The cross section at $\sqrt{s} = 8$ TeV, calculated at LO (leading order) by the **MADGRAPH** generator [27], is $\sigma(W^\pm W^\pm) = 0.3784$ pb, considering both α_{EW}^6 and $\alpha_{EW}^4 \alpha_s^2$ diagrams. Two same-sign W boson production is able to contribute to the final states with two same-sign leptons.

Triboson production includes the WWW , WWZ , and ZZZ processes. Their production mechanism contains the SM quartic gauge boson couplings. The cross sections of the triboson processes at $\sqrt{s} = 8$ TeV, are calculated at LO by the **SHERPA** generator [28] to be $\sigma(WWW) = 0.1498$ pb, $\sigma(WWZ) = 0.1467$ pb, and $\sigma(ZZZ) = 0.1630$ pb. Triboson production is able to contribute to the final states with two, three, or four leptons.

The SM also predicts four-top quark production ($t\bar{t}t\bar{t}$). The cross section at $\sqrt{s} = 8$ TeV, calculated at LO by the **MADGRAPH** generator, is $\sigma(t\bar{t}t\bar{t}) = 0.0007$ pb. The $t\bar{t}t\bar{t}$ process is able to contribute to the final states with two, three, or four leptons, with the existence of four b quarks from the top quark decays.

3

The Large Hadron Collider and ATLAS Experiment

3.1 The Large Hadron Collider

The Large Hadron Collider (LHC) [29] is currently the largest particle collider in the world, with the highest collision energies. It is hosted by the European Organization for Nuclear Research (CERN) and located on the boarder of Switzerland and France. The LHC is in a circular tunnel with a circumference of 26.7 kilometers and between 45 and 170 meters underground. The tunnel was originally constructed for CERN’s Large Electron-Positron (LEP) collider, which was decommissioned in 2000.

The LHC tunnel contains two parallel beampipes that intersect at four interaction points (around which the main detectors are built). In each beampipe, up to 2808 proton bunches circulate simultaneously, at close to the speed of light. The proton bunches are accelerated by electric fields oscillating at radio frequencies, and steered around the LHC ring by magnetic fields of up to 8.3 Tesla, provided by superconducting magnets. The proton bunches in the two beampipes travel in opposite directions, and collide at the four interaction points.

Before being injected into the LHC beampipes, the protons first go through the LINAC2 linear accelerator, Proton Synchronous Booster (PSB), Proton Synchrotron (PS), and Super Proton Synchrotron (SPS), in order to reach an energy of 450 GeV.

For proton-proton collisions, the design center-of-mass collision energy is 14 TeV and the design peak luminosity is $10^{34} \text{ cm}^{-2} \text{ s}^{-1}$. During Run 1 (2010-2012), the LHC was operated below the design parameters, due to some temporary technical issues. In 2012, the center-of-mass collision energy was 8 TeV and the peak luminosity was $7.7 \times 10^{33} \text{ cm}^{-2} \text{ s}^{-1}$. The design parameters will be achieved during Run 2 (2015-), after a long shutdown (2013-2014).

In addition, the LHC is also designed to collide heavy ions (Pb) with an energy of 2.8 TeV per nucleon and a peak luminosity of $10^{27} \text{ cm}^{-2} \text{ s}^{-1}$.

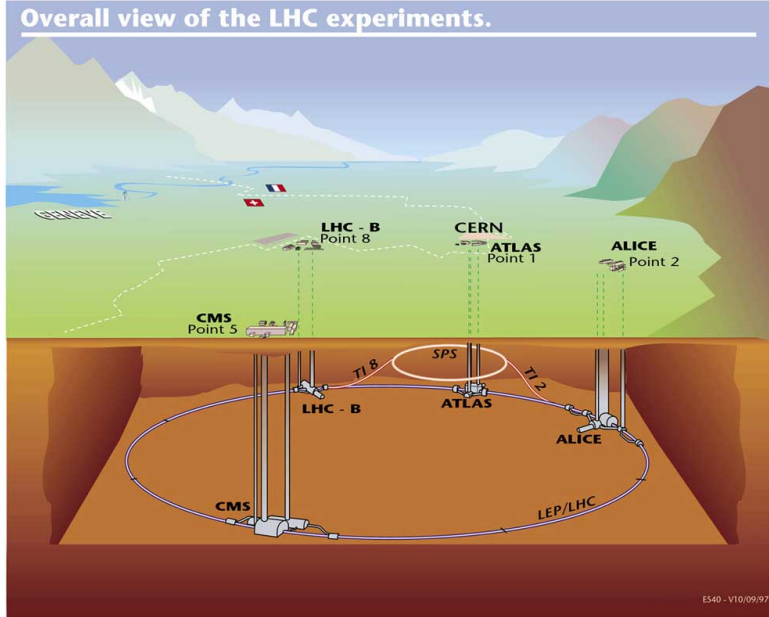


FIGURE 3.1: Overall view of the LHC experiments

Four particle detectors have been constructed at the intersections points of the LHC: ATLAS, CMS, LHCb, and ALICE. The ATLAS and CMS detectors are both large detectors which have general physics purposes, including measurements of the

Higgs boson and searches for beyond-Standard-Model physics. The LHCb and ALICE detectors are smaller and have more specific roles. The LHCb detector is specialized for B-physics, most notably measurements of CP violation. The ALICE detector is specialized for heavy ion physics, most notably quark-gluon plasma.

3.2 The ATLAS Experiment

The ATLAS (A Toroidal LHC ApparatuS) detector [30] collects the collision data at the Interaction Point 1 of the LHC. It is nominally forward-backward symmetric with respect to the interaction point. The dimensions of the detector are 25 meters in height and 44 meters in length. A cut-away view of the ATLAS detector is shown in Fig. 3.2. The ATLAS detector consists of three main sub-systems: inner detector, calorimeters, and muon detectors, from inside to outside. In addition, it has a complicated trigger and data acquisition system.

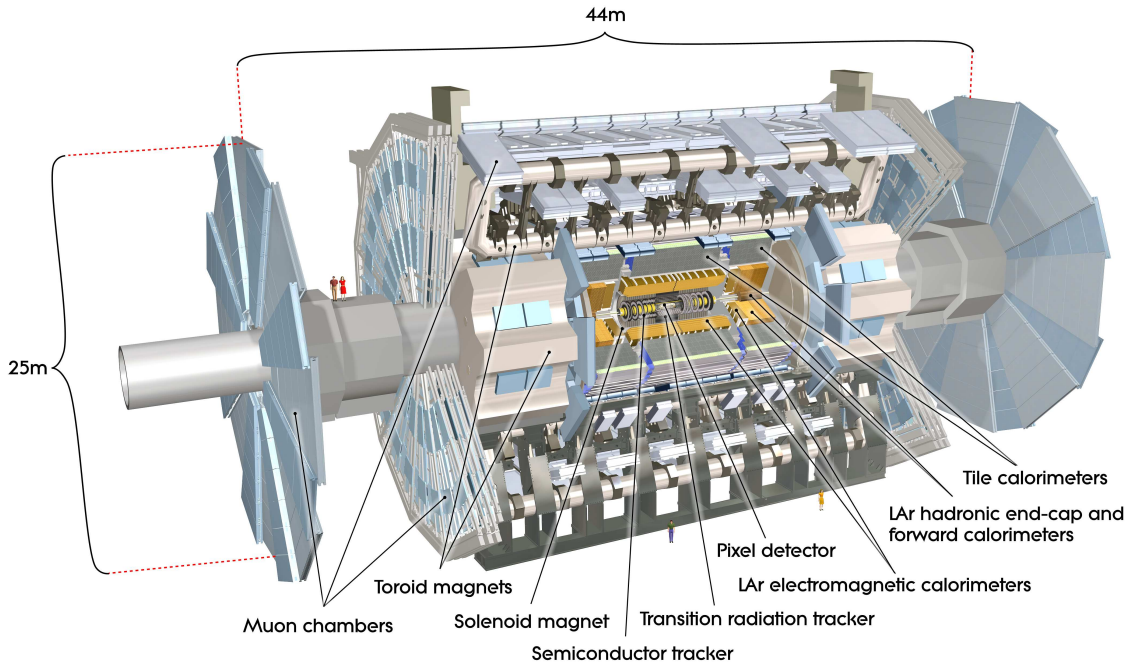


FIGURE 3.2: Cut-away view of the ATLAS detector

The ATLAS coordinate system is briefly documented here. The origin is the center of the detector. The positive x axis points from the origin to the center of the LHC ring. The positive y axis points upwards. The z axis is along the beampipe and its positive direction makes the coordinate system right-handed. Spherical coordinates (r, ϕ, θ) are then defined normally.

The pseudorapidity, η , is defined as

$$\eta = -\ln(\tan \frac{\theta}{2}) \quad (3.1)$$

And the rapidity, y , is defined as

$$y = \left(\frac{1}{2}\right) \ln\left(\frac{E + p_z}{E - p_z}\right) \quad (3.2)$$

where E and p_z is the energy and the z -momentum of a physics object.

Furthermore, the distance in the η - ϕ space, ΔR , is defined as

$$\Delta R = \sqrt{\Delta\eta^2 + \Delta\phi^2} \quad (3.3)$$

3.2.1 Inner Detector

The ATLAS inner detector (ID) precisely measures the tracks of charged particles, for good momentum and vertex resolution, as well as particle identification. It has three components: Pixel detector, Semiconductor Tracker (SCT), and Transition Radiation Tracker (TRT), from inside to outside. A cut-away view of the inner detector is shown in Fig. 3.3.

The inner detector is immersed in a highly uniform 2T magnetic field in the z direction. The magnetic field is provided by a superconducting solenoid magnet, located between the inner detector and the calorimeter. The trajectories of charged particles will be bent by the magnetic field for momentum measurement.

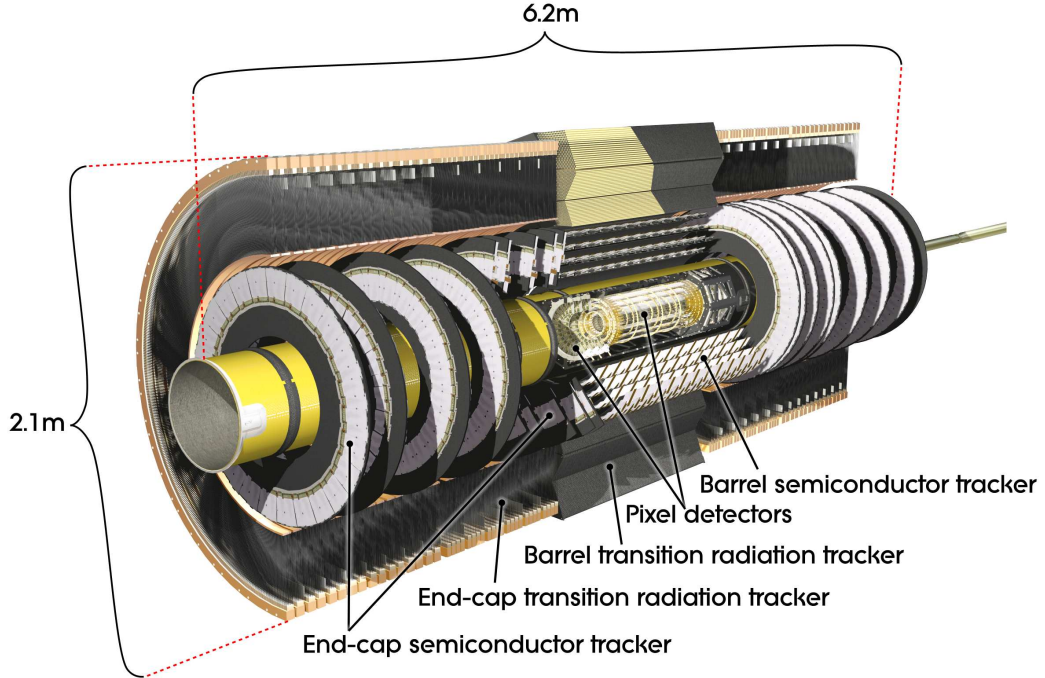


FIGURE 3.3: Cut-away view of the ATLAS inner detector

- **Pixel**

The Pixel detector is only 5cm from the beam axis, and has the highest granularity. It covers the pseudorapidity region of $|\eta| < 2.5$. In the barrel region (with small $|\eta|$), the Pixel detector consists of three cylindrical layers around the beam axis, while in each endcap region (with large $|\eta|$), it consists of three disks perpendicular to the beam axis. The Pixel detector is a silicon detector, generating electronic signals when a charged particle traverses its silicon sensors. The Pixel detector sensors are all identical and have a 2-dimensional size of $50 \mu\text{m} \times 400 \mu\text{m}$. The intrinsic resolution in the barrel region is $10 \mu\text{m}$ ($r-\phi$) and $115 \mu\text{m}$ (z), and that in the endcap region is $10 \mu\text{m}$ ($r-\phi$) and $115 \mu\text{m}$ (r). The Pixel detector has 80.4 million electronic readout channels, dominating the overall ATLAS readout channels. The Pixel detector provides precise position measurements of tracks and information of interaction vertices.

- **SCT**

As with the Pixel detector, the SCT is also a silicon detector, covering $|\eta| < 2.5$. It consists of four barrel layers and nine endcap disks at each end. However, the SCT sensors are 6.4 cm long silicon strip sensors, with a strip pitch of 80 μm . To obtain 2-dimensional position measurements, each SCT module is built with two sets of sensors, and one is rotated by a small angle (40 mrad) with respect to the other. In the barrel layers, one set of sensors is parallel to the beam axis, while in the endcap disks, one set of sensors runs radially. The intrinsic resolution in the barrel region is 17 μm ($r\text{-}\phi$) and 580 μm (z), and that in the endcap region is 17 μm ($r\text{-}\phi$) and 580 μm (z). The SCT has 6.3 million electronic readout channels. It provides precise track position measurements outside the pixel detector volume.

- **TRT**

The TRT consists of 4 mm diameter straw tubes, filled with a gas mixture. It covers the pseudorapidity region of $|\eta| < 2.0$. In the barrel region, the straw tubes are segmented at $z=0$ and run parallel to the beam axis, while in the endcap region, the straw tubes are arranged radially. When a charged particle traverses the TRT straw tubes, the filled gas becomes ionized and the center wires in the tubes collect the resulting signals. The TRT measures track positions in 1-dimension ($r\text{-}\phi$), with an intrinsic resolution of 130 μm , which contributes to overall momentum measurements. In addition, the TRT helps particle identification by detecting transition radiation. The space between the TRT straw tubes is filled by special foam material. A charged particle emits transition radiation when crossing boundaries of this foam, the probability of which depends on the particle's relativistic γ factor. The TRT has 351000 electronic readout channels.

3.2.2 Calorimeter

The ATLAS calorimeter measures the energies of particles. It has two components: the electromagnetic (EM) calorimeter and the hadronic calorimeter (HCAL), from inside to outside. A cut-away view of the calorimeter is shown in Fig. 3.4.

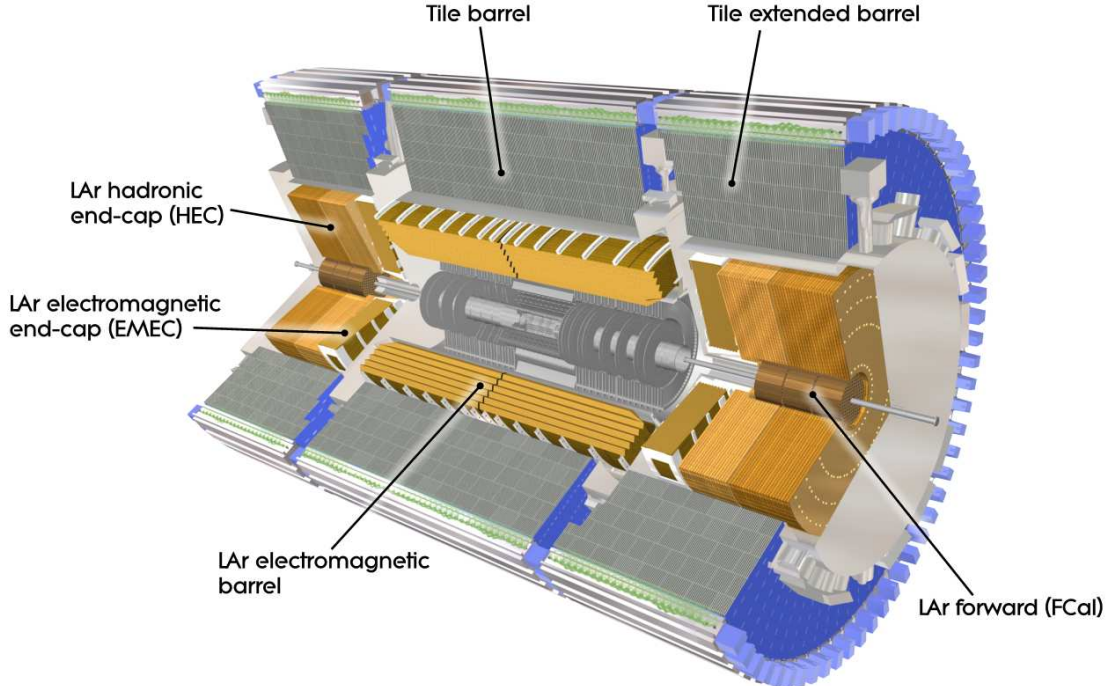


FIGURE 3.4: Cut-away view of the ATLAS calorimeter

EM calorimeter

The EM calorimeter provides precise energy measurements for electrons and photons, with fine granularity. The EM calorimeter is divided into a barrel part ($|\eta| < 1.475$) and two endcap parts ($1.375 < |\eta| < 3.2$). The EM calorimeter is a sampling detector, using liquid Argon in an accordion-shaped configuration as the active material, and lead plates as the absorber. The accordion-shaped configuration provides fine η - ϕ granularity, and complete coverage in ϕ . In depth, the EM calorimeter is

segmented into three layers. The first layer has fine granularity, for the shape of the electromagnetic showers. The second layer has less fine granularity, and collects most of the energies of the electromagnetic showers. The third layer has the least fine granularity, and collects only the tails of the electromagnetic showers. In the region of $|\eta| < 1.8$, a presample detector is placed to correct for the energy loss of electrons and muons before entering the EM calorimeter. The presample detector utilizes an active liquid Argon layer. The overall energy resolution of the EM calorimeter is

$$\frac{\Delta E}{E} = \sqrt{\left(\frac{10\% \sqrt{\text{GeV}}}{\sqrt{E}}\right)^2 + (0.7\%)^2} \quad (3.4)$$

The total thickness of the EM calorimeter is greater than 22 radiation lengths (X_0) for the barrel part, and greater than 24 X_0 for the endcap parts.

Hadronic calorimeter

The hadronic calorimeter contributes to jet reconstruction and E_T^{miss} measurements, with coarser granularity compared to the EM calorimeter. It consists of two different types of hadronic calorimeters: tile calorimeter (for the barrel region) and liquid Argon hadronic calorimeter (for the endcap region).

- **Tile Calorimeter**

The tile calorimeter is the hadronic calorimeter in the central region, which is further divided into a barrel part for $|\eta| < 1.0$ and two extended barrel parts for $0.8 < |\eta| < 1.7$. The tile calorimeter is a sampling detector, using scintillating tiles as the active material, and steel plates as the absorber. The scintillating tiles are read out by photomultiplier tubes. In depth, the tile calorimeter is segmented into three layers, which are 1.4, 4.1 and 1.8 interaction lengths (λ) thick for the barrel part, and 1.5, 2.6 and 3.3 λ for the extended barrel parts.

- Liquid Argon Hadronic Calorimeter

The liquid Argon hadronic calorimeter is located directly behind the EM endcap calorimeter. It covers the endcap region for $1.5 < |\eta| < 3.2$, which has some overlap with the tile calorimeter and the forward calorimeter (described later). The liquid Argon hadronic calorimeter is also a sampling detector, using liquid Argon as the active material, and copper plates as the absorber. In depth, it is segmented into four layers for each endcap. Its total thickness is approximately 10λ .

The overall energy resolution of the hadronic calorimeter is

$$\frac{\Delta E}{E} = \sqrt{\left(\frac{50\% \sqrt{\text{GeV}}}{\sqrt{E}}\right)^2 + (3\%)^2} \quad (3.5)$$

Forward Calorimeter

Besides the EM and hadronic calorimeters described earlier, ATLAS also has a forward calorimeter (FCAL). It provides particle energy measurements in the forward region of $3.1 < |\eta| < 4.9$, and limits the amount of radiation into the muon detectors. The FCAL is integrated inside the endcap EM and hadronic calorimeters, and its front end is recessed by 1.2 meters in order to reduce the reflected neutrons into the inner detector. The FCAL consists of three modules in each side. The first module is the electromagnetic calorimeter component, using copper as the absorber. The second and third modules are the hadronic calorimeter component, using tungsten as the absorber. All these modules use liquid Argon as the sensitive medium. Its total thickness is approximately 10λ , achieved by a high-density design. The overall energy resolution of the forward calorimeter is

$$\frac{\Delta E}{E} = \sqrt{\left(\frac{100\% \sqrt{\text{GeV}}}{\sqrt{E}}\right)^2 + (3\%)^2} \quad (3.6)$$

3.2.3 Muon detectors

The ATLAS muon detectors measure the tracks of muons, and contribute to the muon triggers.

The muon detectors are immersed in toroidal magnetic fields, in order to bend the muon trajectories for momentum measurements. The magnetic fields are provided by three superconducting air-core toroid magnets. Each of the three toroid magnets consists of eight coils that are assembled radially and symmetrically around the beam axis. In the barrel region, magnetic fields of about 0.5 T are provided by the large barrel toroid. In the endcap region, magnetic fields of about 1 T are provided by the two smaller endcap magnets.

Four types of muon chambers are used: Monitored Drift Tubes (MDT), Cathode Strip Chambers (CSC), Resistive Plate Chambers (RPC), and Thin Gap Chambers (TGC). In the barrel region, the chambers are arranged in three cylindrical layers around the beam axis, while in the endcap region, the chambers are installed in three layers perpendicular to the beam axis. A cut-away view of the muon detectors is shown in Fig. 3.5.

- MDT

The MDT provides precise measurements of the muon tracks. It covers the pseudorapidity range of $|\eta| < 2.7$ (except for the innermost endcap layer where its coverage is limited to $|\eta| < 2.0$). The MDT chambers consist of three to eight layers of drift tubes, which achieve an average resolution of 80 μm per tube, and 35 μm per chamber.

- CSC

The CSC is placed in the innermost endcap layer, providing additional track measurements for $2.0 < |\eta| < 2.7$. CSC, instead of MDT, is used in that area

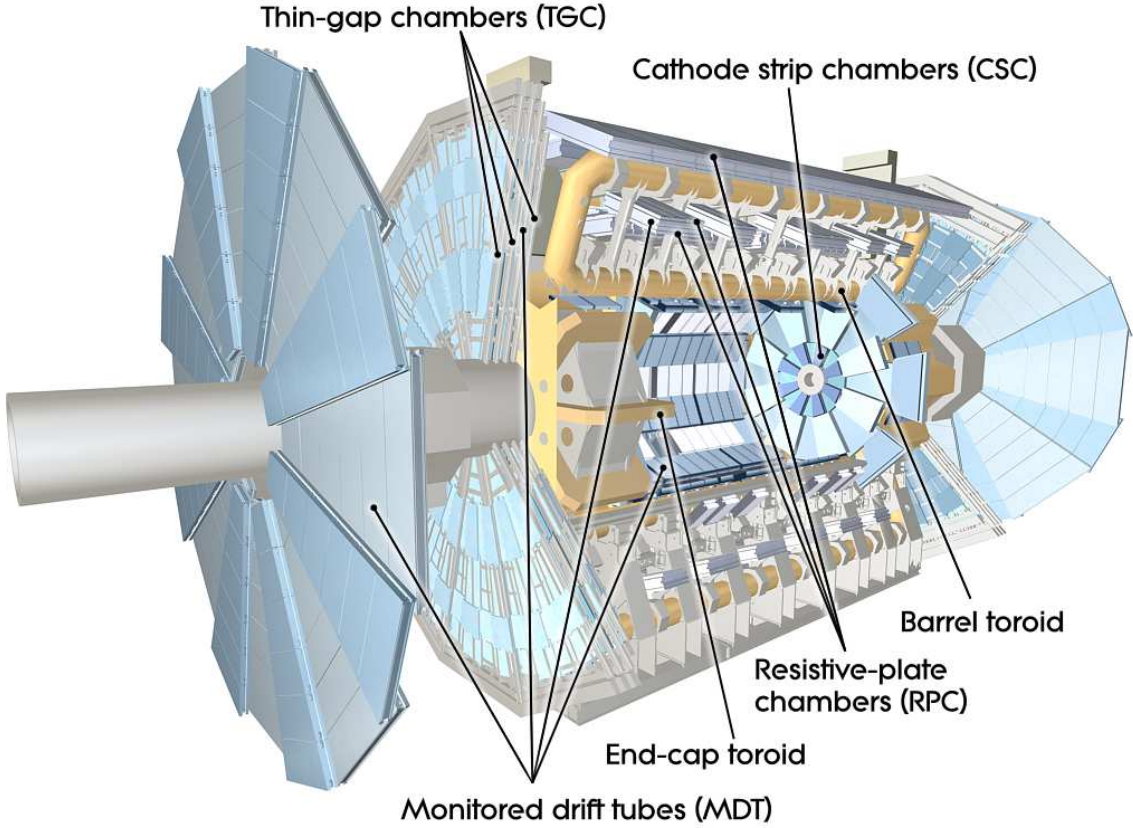


FIGURE 3.5: Cut-away view of the ATLAS muon detectors

due to its high rate capability. The CSC chambers are multiwire proportional chambers with cathodes segmented into strips. The resolution of a CSC chamber is $40 \mu\text{m}$ in the bending plane, and 5 mm in the transverse plane.

- **RPC**

The RPC covers the barrel region of $|\eta| < 1.05$. It provides fast signals for the muon triggers, and also measures the track coordinates to complement the MDT. In the RPC chambers, gas is filled in a gap between two resistive plates (with high voltage), which becomes ionized and induces electronic signals when a muon traverses it. Its position resolution is approximately 1 cm , and its intrinsic time resolution is about 1.5 ns .

- TGC

The TGC covers the endcap region of $1.05 < |\eta| < 2.4$. Similar to the RPC, it contributes to the muon triggers and complements the MDT’s track measurements. The TGC chambers are multiwire proportional chambers with a wire-to-wire distance of 1.8 mm. Its position resolution is several millimeters, and its intrinsic time resolution is about 4 ns. After adding the signal propagation and electronics contributions, the time resolution of both the RPC and the TGC is 15-25 ns, providing the ability for beam-crossing time identification.

3.2.4 Forward detectors

Besides the three main sub-detectors described above, there are several small sub-detectors built in the forward region of the ATLAS detector:

- LUCID

LUCID (LUminosity measurement using Cerenkov Integrating Detector) is located at a distance of ± 17 meters from the interaction point. LUCID is a Cerenkov detector, consisting of aluminum tubes that are around the beampipe and filled with C_4F_{10} . Its main purpose is determining the (relative) integrated luminosity, and monitoring the instantaneous luminosity and beam conditions, via inelastic scattering in the forward region.

- ALFA

ALFA (Absolute Luminosity For ATLAS) is located at a distance of ± 240 meters from the interaction point. It consists of scintillating fibre trackers located inside Roman pots, approaching as close as 1 mm to the beam. Its main purpose is determining the (absolute) luminosity, via elastic scattering in the forward region.

- ZDC

ZDC (Zero-Degree Calorimeter) is located at a distance of ± 140 meters from the interaction point. In each side of ZDC, there are four modules consisting of quartz rods and tungsten plates. Its main purpose is determining the centrality for heavy-ion collision, by detecting forward neutrons.

3.2.5 Trigger and Data Acquisition System

ATLAS relies on its trigger and data acquisition (TDAQ) system to obtain and store the event data from the detectors. A schematic view of the TDAQ system is shown in Fig. 3.6. One thing to note is the design rates and the achieved rates in 2012 are different. For simplicity, this document only refers to the design rates.

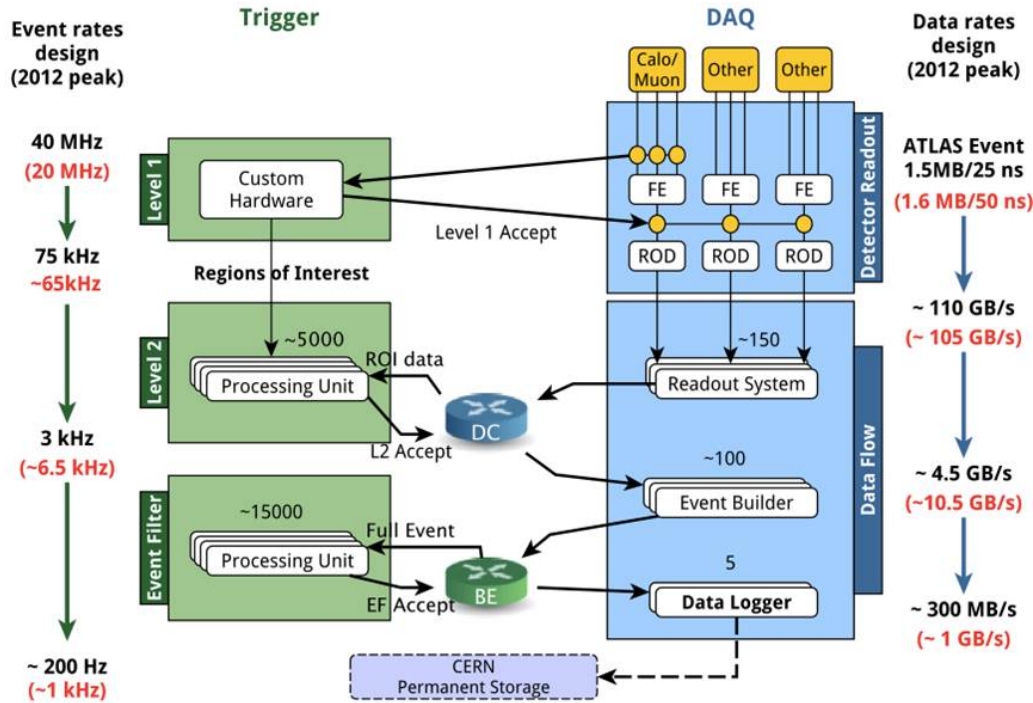


FIGURE 3.6: Schematic view of the ATLAS TDAQ system

Trigger System

The collision rate at the ATLAS detector is 40 MHz but its ability of storing data is only about 200 Hz. Therefore, to select only interesting events, different trigger selections are utilized during the data taking. The ATLAS trigger system consists of three levels: Level 1 (L1), Level 2 (L2), and event filter (EF). Each trigger level refines the selections made by the previous level. The L2 and EF together are also referred to as high level trigger (HLT).

- L1

The L1 is a hardware-based trigger system. It searches for high transverse-momentum particles, as well as large missing/total transverse energy. Its selections are based on information from the muon trigger detectors (the RPC and TGC), as well as all the calorimeters. The L1 muon and calorimeter selections are then processed by the central trigger processor (CPT). The CPT implements a trigger menu, which is made up of different trigger selections, and is set before each data taking run. In addition, the L1 also defines one or more Regions-of-Interest (ROI) for each event, which are the η and ϕ coordinates of the regions which have identified interesting features. The ROI information is later used by the HLT. The output rate of the L1 trigger system is 75 kHz, and the decision time is less than $2.5 \mu\text{s}$.

- HLT

The L2 and EF are software-based trigger systems. The L2 selections utilize all the available detector data (including the inner detector data) within the ROI. The output rate of the L2 trigger system is 3.5 kHz, and the event processing time is about 40 ms. The EF selections use the ATLAS offline analysis software. The output rate of the EF is 200 Hz, and the event processing time is of the

order of four seconds.

Data Acquisition System

The data acquisition (DAQ) system is the bridge between the detectors and the permanent storage. It communicates with the trigger system.

The Readout Drivers (ROD) are functional elements for gathering information from the detector front-end electronics. Although both the front-end electronics and ROD are detector-specific, they are built from standard blocks. Once an event is selected by the L1 trigger system, the event data is transferred from the detector front-end electronics to the ROD. The data is then formatted as raw data at ROD, and further transferred to the main DAQ system via point-to-point links.

The readout system, which is the first stage of the main DAQ system, temporarily stores the data in its local buffers. The data is then utilized by the L2 trigger system. Once the event is selected by the L2, the event data is transferred to the Event Builder (EB). The EB provides information to the EF trigger system for the final trigger selection. Once the event is selected by the EF, the event data is moved to the permanent storage at the CERN computing center.

In addition, the DAQ system also contributes to the configuration, control and monitoring of the ATLAS detector (as an interface between the control room and the detector).

4

Data and Simulation Samples

4.1 Data Samples

This study uses data from proton-proton collisions at $\sqrt{s} = 8$ TeV collected by the ATLAS detector at the LHC, between April and October in 2012. The integrated luminosity delivered by the LHC during this period was $\int \mathcal{L} dt = 21.3 \text{ fb}^{-1}$. From this, the integrated luminosity recorded by the ATLAS detector and marked as “good for physics” (see below) was $\int \mathcal{L} dt = 20.3 \text{ fb}^{-1}$. The uncertainty associated with the luminosity determination is 2.8%. At ATLAS, data is taken in so-called “runs,” each typically lasting for several hours. Data taking runs are further separated into data taking periods.

To ensure good data quality, this study only uses data taking runs belonging to the so-called good runs list (GRL). The GRL contains data taking runs during which the LHC beams are stable, and all sub-systems of the ATLAS detector relevant to this study are operating normally. The sub-systems include the solenoid and toroid magnets, inner detector, electromagnetic and hadronic calorimeters, muon detectors, and triggers.

4.2 ATLAS Simulation Procedure

To predict the behavior of the physics processes at ATLAS, Monte Carlo (MC) simulation samples are used. These are produced in several steps: event generation, detector simulation, and digitization [31]. Typically, the event generation is further divided into matrix element (ME) calculation, parton showering (PS), and hadronization [32]. These steps will be briefly described in this section. After these steps, the MC simulation samples are in a similar format to the real data samples, ready for further object reconstruction.

4.2.1 *Matrix Element Generators*

Matrix element generators calculate the hard scattering part of parton level processes, to a fixed order in terms of α_s (the strong coupling constant). There exist a variety of ME generators, which are typically categorized as Leading-Order (LO) or Next-to-Leading-Order (NLO) generators.

LO generators calculate the tree-level diagrams. They are mostly useful for those processes with well-separated and energetic partons in the final state. Two widely used LO generators are `ALPGEN` [33] and `MADGRAPH` [27]. However, LO generators ignore loop diagram contributions, and have a large uncertainty due to the renormalization and factorization scale choice.

The general trend is moving from LO generators to NLO generators. NLO generators calculate both the tree-level diagrams and loop diagrams. The advantage of NLO generators is that they are more accurate, and have less dependence on the renormalization and factorization scale choice. Two widely used NLO generators are `MC@NLO` [34] and `POWHEG` [35].

Next-to-Next-to-Leading-Order (NNLO) generators exist, but are still under development.

4.2.2 Parton Showering

It is technically difficult to use ME generators in the soft/collinear kinematic regions. To alleviate this difficulty, parton showering is used to approximately describe the QCD interactions to all orders in terms of α_s . In this step, partons at a high energy scale are evolved to a low energy scale by radiating soft partons. This is further applied to the radiated partons until no further radiation is produced. PS is good for soft/collinear kinematic regions, and thus for modeling the structure inside jets. Two common PS generators at ATLAS are PYTHIA [36] and HERWIG [37]. They are general-purpose MC generators and have also matrix element functionality for a wide range of processes.

PS generators need to interface with ME generators, to be able to take the advantages they both can offer. One difficulty with this interface is double-counting the same sub-processes in both the ME and PS generators. Several algorithms have been developed to deal with the problem of double counting.

Besides the primary hard parton interactions, there can be interactions of the remaining partons of the colliding hadrons, leading to so-called underlying events. Such interactions are generally soft and can not be described by perturbative QCD theory. Thus, phenomenological models are utilized to simulate underlying events. At ATLAS, PYTHIA and HERWIG, incorporated with the LHC data, are used to also implement the underlying event simulation.

4.2.3 Hadronization

Recalling the color confinement of QCD, a quark or a gluon is not able to be directly observed. Rather, the quark or gluon will evolve by radiating soft partons, and the partons will combine to form color-neutral hadrons. This will result in a jet, which is a shower of hadrons collimated within a cone around the direction of the original quark or gluon. This process is called hadronization. Hadronization has

not got described by first principles. At ATLAS, PYTHIA and HERWIG contain phenomenological models that are used to simulate hadronization. PYTHIA uses the Lund string model [38], while HERWIG uses the cluster model [39].

In the step of hadronization, some specialized generators are also utilized: tau lepton decays are simulated using TAUOLA [40], and photon radiation is simulated using PHOTOS [41].

4.2.4 *Detector Simulation*

The above steps describe the particles produced from collision events before they enter the inner detector. GEANT4 [42], is then used to describe the detector responses to particles traversing the detectors. The ATLAS geometry, including active detector elements, electronics, and services (cooling, power supply, etc.), is built into a database. By utilizing the database, GEANT4 simulates the detector responses, including any particle decay in the detector volume, and produces a hit file, which contains the energy deposits in all detector elements. The detector simulation also keeps a record of truth information for all particles, including their four momenta.

At ATLAS, several fast simulation programs are also available, which replace the most time consuming parts of the GEANT4 simulation with parameterized detector responses. Fast simulation significantly reduces the computing time, with reasonable simulation accuracy.

4.2.5 *Digitization*

The digitization step converts the energy deposits in the above hit file to digitized detector responses. Typically, a digit is produced when the voltage or current of a readout channel is above certain threshold. The digitization programs are specific for each of the subdetectors. The output of the digitization step has a similar format to that of real data, and is now ready for object reconstruction.

Besides the primary collision, there may exist interactions from other collisions in the same bunch crossing (in-time pileup), and interactions from the preceding bunch crossing (out-of-time pileup). In the digitization step, the effects of in-time and out-of-time pileup, as well as non-collision backgrounds, are overlaid with the primary collision. These effects are typically produced by the general-purpose generators, and the luminosity profile of real data is achieved after the overlay.

4.3 Monte Carlo Samples

In this study, Monte Carlo samples are used for several purposes, including optimizing event selection requirements, modeling kinematic distributions of signal and background processes, estimating systematic uncertainties, and producing templates for the cross section fit. For these samples, all the particle masses are taken from the Particle Data Group [8], except the top quark mass is set at 172.5 GeV, and the Higgs boson mass is set at 125 GeV.

The samples that use HERWIG for parton showering and hadronization are interfaced to JIMMY 4.31 [43] for the underlying event simulation. Furthermore, all pileup events are generated by PYTHIA 8.1 with the MSTW2008 LO PDF set [11].

The detector simulation of most samples is processed by GEANT4. Some background processes, such as tZ , use the ATLFast2 program [44] instead, which is a combination of GEANT4 and a fast simulation for the calorimeter response. After the detector simulation and digitization steps, all the MC samples are processed by the same object reconstruction as the data samples.

4.3.1 $t\bar{t}V$ Production

The $t\bar{t}W$ and $t\bar{t}Z$ production is simulated using the MADGRAPH 5 LO generator, which calculates matrix elements with up to two additional partons. The PS and hadronization are done by PYTHIA 6.425 with the AUETE2B tune [45] for the un-

derlying event simulation. The PDF set used is CTEQ6L1 [12]. The $t\bar{t}Z$ simulation includes the off-shell Z/γ^* contributions (for γ^* masses above 5 GeV). The $t\bar{t}V$ samples are normalized to the NLO cross sections.

4.3.2 $W/Z + jets$ Production

As one of the main backgrounds to $t\bar{t}V$, $W/Z + jets$ production is simulated by the ALPGEN v2.14 generator, which calculates matrix elements with up to five additional partons. We also use PYTHIA 6.425 for the PS and hadronization, as well as the CTEQ6L1 PDF set. The simulation is done separately for $W/Z + light\ jets$, $W/Z + b\bar{b}$, $W/Z + c\bar{c}$, and $W + c$. To avoid overlap among these samples, an algorithm based on the distance in $\eta\text{-}\phi$ space between the quarks is utilized. The $W/Z + jets$ samples are then normalized to the NNLO cross sections.

4.3.3 Diboson Production

Diboson production, including the W^+W^- , WZ and ZZ processes, is simulated using the SHERPA generator [28] with the CT10 PDF set [46]. The LO matrix element calculations of SHERPA use massive b and c quarks, and cover up to three additional quarks. The off-shell Z/γ^* component is included, with a requirement of $m_{ll} > 0.1$ GeV on the outgoing leptons. These samples are normalized to the NLO cross sections. In addition, alternative diboson samples are produced with the POWHEG 2.0 NLO generator, interfaced with PYTHIA 6.425 or PYTHIA 8.1. These alternative samples are used to evaluate modeling uncertainties.

4.3.4 $t\bar{t}$ and Single Top production

The production of top quark pairs and single top quarks (including the t-channel, s-channel, and Wt channel), is simulated by the POWHEG generator with the CT10 PDF set. The samples are then interfaced with PYTHIA 6.425 with the CTEQ6L1

PDF set, which includes the Perugia2011C tune [47] for the underlying event simulation. The $t\bar{t}$ and single top samples are normalized to the NNLO cross sections.

4.3.5 Higgs production

$t\bar{t}H$ production is simulated using NLO matrix elements from the HELAC-ONELOOP package [48]. POWHEG, with the CT10 PDF set, is then used as an interface. The PS and hadronization is done by PYTHIA 8.1 with the CTEQ6L1 PDF set and the AU2 tune [49] for underlying events.

The $gg \rightarrow H$ processes are simulated by POWHEG, interfaced with PYTHIA 8.1. The WH and ZH processes are simulated by PYTHIA 8.1. The CTEQ6L1 PDF set is used for these samples. All the Higgs production samples are normalized to the NNLO QCD cross sections, with the NLO electroweak corrections.

4.3.6 Small Background Processes

The association production of a single top quark and a Z boson, tZ , is simulated with the MADGRAPH 5 generator. The samples are then interfaced with PYTHIA 6.425, which includes the AUET2B tune for underlying events. The CTEQ6L1 PDF set is used. The samples are normalized to the NLO theoretical cross sections.

Triboson production, including the WWW , WWZ , and ZZZ processes, is also simulated by MADGRAPH 5 and PYTHIA 6.425. The LO cross sections calculated by the MADGRAPH generator are used to normalize the triboson samples.

Production of two same-sign W bosons ($W^\pm W^\pm$) is simulated with the SHERPA generator, with the CT10 PDF set. These samples are normalized to the LO cross sections calculated by the generator.

In addition, the SM four top quark production, $t\bar{t}t\bar{t}$, is simulated by MADGRAPH 5 and PYTHIA 8. The LO cross sections calculated by the MADGRAPH generator are used to normalize the $t\bar{t}t\bar{t}$ samples.

Monte Carlo samples used in this study are summarized in Table 4.1. For each process, the generator and cross section are listed. (Some cross sections are calculated with kinematic requirements.)

Table 4.1: Summary of Monte Carlo samples used in this study.

Process	Generator	Cross Section
$t\bar{t}W$	MADGRAPH+PYTHIA	0.232 pb
$t\bar{t}Z$	MADGRAPH+PYTHIA	0.215 pb
$W \rightarrow \ell\nu$	ALPGEN+PYTHIA	12087 pb
$Z/\gamma^* \rightarrow \ell\ell$	ALPGEN+PYTHIA	1122 pb
W^+W^-	SHERPA	54.71 pb
WZ	SHERPA	33.31 pb
ZZ	SHERPA	11.17 pb
$t\bar{t}$	POWHEG+PYTHIA	252.9 pb
single top (Wt -chan)	POWHEG+PYTHIA	22.37 pb
single top (s -chan)	POWHEG+PYTHIA	5.61 pb
single top (t -chan)	POWHEG+PYTHIA	87.76 pb
$t\bar{t}H$	POWHEG+PYTHIA	0.1293 pb
$gg \rightarrow H$	PYTHIA	19.27 pb
WH	PYTHIA	0.7046 pb
ZH	PYTHIA	0.4153 pb
tZ	MADGRAPH+PYTHIA	0.236 pb
$W^\pm W^\pm$	SHERPA	0.3784 pb
WWW	MADGRAPH+PYTHIA	0.1498 pb
WWZ	MADGRAPH+PYTHIA	0.1467 pb
ZZZ	MADGRAPH+PYTHIA	0.1630 pb
$t\bar{t}t\bar{t}$	MADGRAPH+PYTHIA	0.0007 pb

5

Object Reconstruction

This chapter discusses the reconstruction of the physics objects used in this study, in particular, tracks, electrons, muons, jets, and missing transverse momentum.

5.1 Tracks

As mentioned in Chapter 3, the ATLAS inner detector measures the tracks of the charged particles traversing it. The tracks are important for the electron, muon and jet reconstruction, as well as the primary vertex reconstruction (which is useful for further event selection). This section briefly discusses the reconstruction of the inner detector tracks and primary vertices.

The ATLAS inner detector tracking algorithm [50] consists of two consecutive sequences: the main inside-out tracking and the outside-in tracking. The inside-out tracking is further realized in several stages. Firstly, it creates SpacePoint objects, which are 3-dimensional coordinate positions of the pixel and SCT measurements. Secondly, the inside-out tracking looks for seeds for the track search, which consist of 3 SpacePoint objects. Using the seeds, track candidates are created, with roads of detector elements which are likely to contain track hits. A Kalman filter is utilized

to progressively add hits to the roads. Thirdly, track candidates may share hits, so a track scoring strategy is utilized, which describes the overall track quality. The shared hits are then assigned to the track with higher score. Finally, the tracks are extended into the TRT, by adding the TRT hits without modifying the original silicon tracks. After this, track parameters are refit using all the associated hits. The tracks reconstructed by the inside-out tracking are required to have $p_T > 0.4$ GeV.

After the above stages, the outside-in tracking is implemented. The outside-in tracking is mainly for the tracks that are not reconstructed by the inside-out tracking, including tracks sharing many silicon hits with other tracks, tracks from secondary hadron decays or photon conversions, as well as tracks with substantial energy loss. The outside-in tracking is realized in two stages. Firstly, it starts with a dedicated TRT segment finder, including a global pattern search and then a local pattern recognition. Secondly, the found TRT segments are extended inwards, by adding silicon hits along the roads. In particular, tracks with a TRT segment but no silicon detector extension are referred to as TRT-standalone tracks.

In addition, primary vertices are reconstructed with an iterative vertex finding approach [51]. The reconstructed tracks passing certain preselection criteria are considered as from the interaction region and used in the vertex finding. The first vertex seed is determined using the global maximum of the z coordinates (along the z axis) of the tracks. Then a χ^2 -based vertex fitting algorithm is utilized to determine the vertex position, taking the vertex seed position and the tracks as inputs. After the fit, the tracks that are deviated from the vertex by more than 7σ are used to seed another vertex. This procedure is repeated until all the tracks are associated with vertices and no new vertex is found. In the vertex finding, beam spot parameters are used in both the track preselection criteria, and the vertex fitting algorithm.

5.2 Electrons

At ATLAS, electron candidates are defined as energy deposits in the electromagnetic calorimeter matched to tracks in the inner detector [52]. This section describes the reconstruction and selection of the electron candidates.

5.2.1 *Electron Reconstruction*

The first step of electron reconstruction is electron seed-cluster reconstruction. The η - ϕ space of the EM calorimeter is divided into 200 (N_η) \times 256 (N_ϕ) towers. The energies of the EM calorimeter cells are summed up to get the energies of the corresponding towers. Then a sliding-window algorithm is utilized to search for seed clusters of towers with a total transverse energy above 2.5 GeV. The window size used is 3 (N_η) \times 5 (N_ϕ) towers.

The second step of electron reconstruction is electron-track candidate reconstruction. Tracks are considered loosely matched to a cluster, if they are within 0.2 (on the side of track bending) or 0.05 (on the opposite side) in ϕ of the cluster. Furthermore, tracks with at least four silicon hits are extrapolated from the point of the closest approach to the primary vertex, and are required to be within 0.05 in η of the cluster. Tracks with less than four silicon hits are extrapolated from the last measurement point, and do not have the requirement on $\Delta\eta$ to the cluster. After forming electron-track candidates, track parameters of the candidates with at least four silicon hits are recalculated using a Gaussian Sum Filter (GSF) algorithm, which works better by accounting for the bremsstrahlung effects. The candidates with less than four silicon hits still use the original track parameters.

The third step of electron reconstruction is so-called electron-candidate reconstruction. An electron candidate is considered to be reconstructed if at least one track is matched to a seed cluster. Tighter matching requirements are used: $\Delta\phi$

between the cluster and track needs to be within 0.1. For tracks with less than four silicon hits, $\Delta\eta$ needs to be within 0.35 (0.2) in the barrel (endcap) region, and $\Delta\phi$ needs to be within 0.03 (0.02) on the same (opposite) side of track bending. All the tracks matched to a cluster will be kept, but the best matched track will be chosen as the primary track, used for electron kinematics and identification. For the primary track choice, tracks with at least one pixel hit are preferred, and, if several tracks contain pixel hits, the one with the smallest ΔR to the cluster is chosen.

After electron candidates are defined, the energies are recomputed. Energy calibration is applied to the calorimeter cells, clusters are rebuilt, and a number of pre-corrections are applied. Then the cluster energies are corrected by scale factors from a multivariate algorithm, taking the total energy in the accordion EM calorimeter, the ratio between the presampler energy and the accordion energy, the shower depth, and the η and ϕ positions of the clusters as inputs. Finally, additional correction factors are applied to electrons in data events and an energy smearing is applied to electrons in simulated events, in order to achieve good data-simulation agreement. The correction and smearing are derived using $Z \rightarrow ee$ events. In terms of the four-momenta of reconstructed electrons, the corrected cluster energies are used. The η and ϕ directions are given by the track parameters (cluster information), for electrons with at least four silicon hits (less than four silicon hits).

5.2.2 Electron Selection

The objects from electron reconstruction contain not only signal electrons, but also fake electrons, which are hadronic jets, as well as electrons from photon conversions, Dalitz decays, and heavy flavor hadron decays. To reject these fake electrons, further electron identification based on various discriminating variables is utilized. The discriminating variables include those describing the shapes of the EM showers, the properties of the tracks, as well as the matching between the tracks and the clusters.

Both cut-based and likelihood electron identification are available.

The cut-based electron identification applies sequential cuts on the discriminating variables. These cuts are optimized in 10 bins in $|\eta|$ and 11 bins in p_T , due to the dependence of the discriminating variables on η and p_T . Several selections are available, including `loose`, `medium`, and `tight`. Tighter selections have stricter requirements on the variables used.

The Likelihood electron identification utilized a multivariate analysis technique. It is able to calculate and cut on the probability for an electron object to be a signal electron, based on the values of certain discriminating variables. The likelihood electron identification is implemented in 9 bins in $|\eta|$ and 6 bins in p_T . Several likelihood selections are available, including `LOOSE`, `MEDIUM`, and `VERY TIGHT LH`. Different selections may use different sets of variables. This study chooses to use the `MEDIUM LH` selection, which has similar signal electron efficiency to the `medium` cut-based selection, but better rejection of the fake electrons.

Other requirements on electron objects are also used in this study. The cluster η are required to be within $|\eta_{\text{cluster}}| < 2.47$, but not within $1.37 < |\eta_{\text{cluster}}| < 1.52$, where the electron identification efficiency is low.

The electrons are required to be separated from other objects with isolation requirements, to further remove fake electrons. Isolation is calculated in two ways: summing up the p_T of tracks, or E_T of clusters, in a cone with respect to the direction of the electron, and are called `PtCone30` and `EtCone20`, respectively. The tracks (clusters) are selected in a cone of $\Delta R = 0.3$ (0.2), and exclude those associated with the electron of interest. The calorimeter-based isolation is corrected for pileup and leakage. In the 2SSL and 3L channels, electrons with $p_T < 50$ GeV are required to have $\text{EtCone20}/p_T < 0.12$ and $\text{PtCone30}/p_T < 0.12$. For electrons with $p_T > 50$ GeV, the isolation requirements are $\text{EtCone20} < 6$ GeV and $\text{PtCone30} < 6$ GeV instead. Fake electrons are less significant for the 2OSL and 4L channels, thus the isolation

requirements are loosened. The 2OSL channel requires only the track isolation cut of $\text{PtCone30}/p_T < 0.12$. The 4L channel further loosens this cut to $\text{PtCone30}/p_T < 0.18$.

The impact parameters of electrons are required to be small, to be consistent with prompt electrons originating from the primary vertex. The transverse (longitudinal) impact parameter, d_0 (z_0), is defined as the distance from the primary vertex to the point of the closest approach of the track in the x - y plane (the z direction). z_0 is required to be less than 2mm for all analysis channels. In the 2SSL channel, in order to suppress the (large) electron charge mis-identification and fake electron backgrounds, we apply a cut on the longitudinal impact parameter, $|z_0 \sin \theta| < 0.4$ mm, where θ is the polar angle of the electron object, as well as a cut on the transverse impact parameter, $|d_0/\sigma(d_0)| < 3$, where $\sigma(d_0)$ is the uncertainty on d_0 .

The reconstruction, isolation, and trigger selection efficiencies of simulated electrons are also corrected to account for the differences between simulation and data. These corrections are derived from the $Z \rightarrow ee$ events and applied as a function of p_T and η . All the correction factors are consistent with 1.0 within 1%.

5.3 Muons

This section describes the reconstruction and selection of muon candidates in this study.

5.3.1 Muon Reconstruction

To reconstruct and identify muons [53], the ATLAS experiment mainly uses information from the muon detectors and inner detector, and less frequently uses information from the calorimeters. Four different muon identification criteria (muon “types”) are available, according to which detectors are utilized:

- Stand-Alone (SA) muons: The tracks of Stand-Alone muons are reconstructed

only in the muon detectors, and extrapolated back to the point of closest approach to the beamline, in order to obtain information (direction of flight, impact parameters, etc.) in the interaction area. The SA muons are required to traverse at least two layers of the muon detectors. They are mainly used for muon reconstruction in the range of $2.5 < |\eta| < 2.7$, which is not covered by the inner detector.

- Combined (CB) muons: For Combined muons, track reconstruction is first performed independently for the inner detector and muon detectors. Then, if a combination of an inner detector track and a muon detector track is successful, a CB muon will be formed with the combined track. The CB muons have the highest muon purity, and are the most important type of reconstructed muons.
- Segment-tagged (ST) muons: Segment-tagged muons are reconstructed if an inner detector track is matched to at least one track segment in the MDT and CSC chambers. The ST muons are mainly used to detect muons that traverse only one layer of the muon detectors, because their energies are low, or they are in the muon detector regions with reduced acceptance.
- Calorimeter-tagged (CaloTag) muons: Calorimeter-tagged muons are reconstructed if an inner detector track is matched to an energy deposit in the calorimeters which is consistent with a minimum ionizing particle. The CaloTag muons have low purity, but can recover the acceptance of certain regions where the muon detectors have no coverage. They are optimized for $|\eta| < 0.1$.

The CB and SA muon reconstruction is affected by the acceptance losses of the muon detectors. In the region of $|\eta| < 0.1$, the muon detectors are only partially equipped, in order to provide space for services of the inner detector and calorimeters. In the region of $1.1 < |\eta| < 1.3$ (between the barrel and endcaps), only one layer of

muon chambers is installed for certain ϕ regions.

The reconstruction of the SA, CB, and ST muons is performed using two different implementing strategies (“Chains”), for both the reconstruction in the muon detectors, and the combination of the inner detector and muon detector tracks. The first chain (“Chain 1”) uses a statistical combination of the track parameters for the inner detector and muon detector tracks. The second chain (“Chain 2”) uses a global refit with hits in both the inner detector and muon detectors. These two independent chains were used during the ATLAS commissioning phase to check the robustness of muon reconstruction. They have shown similar performances and both have been used for ATLAS publications.

5.3.2 Muon Selection

This study uses only the Combined muons and the “Chain 2” strategy. Similarly to electron reconstruction, the objects from muon reconstruction include not only signal muons, but also fake muons. To reject fake muons, the muon objects are required to pass a set of “tight” quality cuts on the muon tracks, although “medium” and “loose” sets are also available. They are also required to be within $|\eta| < 2.5$, corresponding to the muon detector coverage. In addition, the inner detector track needs to have sufficient number of hits to be consistent with a muon track, which are detailed as follows:

- Number of pixel hits + number of crossed dead pixel sensors > 0 .
- Number of SCT hits + number of crossed dead SCT sensors ≥ 5 .
- Number of pixel holes + number of SCT holes < 3 . A hole is an expected but non-existing measurement point in the track trajectory.
- For muons within $0.1 < |\eta| < 1.9$, $n > 5$ and $n_{\text{TRTOutliers}}/n < 0.9$, where $n = n_{\text{TRTHits}} + n_{\text{TRTOutliers}}$, and n_{TRTHits} ($n_{\text{TRTOutliers}}$) denotes the number of

good TRT hits (TRT outliers) on a muon track. A TRT outlier is a TRT straw tube with a signal from other tracks, or a set of TRT measurements failing to form a smooth trajectory with the silicon detector measurements.

We require each muon to be separated from other objects by making isolation requirements, to further reduce fake muon backgrounds. The isolation variable uses tracks in a cone of $\Delta R = 10 \text{ GeV}/p_T(\mu)$ around the muon direction, where $p_T(\mu)$ is the muon transverse momentum. The track of the muon is excluded, and the sum of p_T of all the other tracks in the cone is then required to be less than $0.05 * p_T(\mu)$. This p_T -dependent track-based isolation requirement is found to have good performance under high pile-up conditions.

The impact parameters of muons are required to be small, to be consistent with prompt muons originating from the primary vertex. Similarly with the electron selection, z_0 is required to be less than 2mm for all analysis channels. In the 2SSL channel, in order to suppress the fake muon backgrounds, we apply a cut on the longitudinal impact parameter, $|z_0 \sin \theta| < 0.4 \text{ mm}$, as well as a cut on the transverse impact parameter, $|d_0/\sigma(d_0)| < 3$.

Momenta of muons in the simulation samples are corrected to match the muon momentum scale and resolution in data. Reconstruction, identification and isolation efficiencies are also corrected for the simulated muons for better data/simulation agreement. These corrections are derived using $Z \rightarrow \mu\mu$ events.

5.4 Jets

A jet is a large number of hadrons that result from the hadronization of a high energy quark or gluon. At ATLAS, a jet is identified with a group of energy deposits in both the EM calorimeter and hadronic calorimeter, often associated with several matched tracks in the inner detector [54]. This section describes the reconstruction

and selection of jets.

5.4.1 Jet Reconstruction

The first step of jet reconstruction is forming topological calorimeter clusters. First, seed cells are found, if the signal-to-noise ratio is above 4.0. The signal is defined as the absolute value of the energy deposited in the cell, and the noise is defined as the RMS of the energy distribution in random events, including both electronic noise and pileup noise components. Second, cells near the seed cell with signal-to-noise ratio above 2.0 are included in the cluster. Finally, all cells near the cluster are added.

After a topological cluster is formed, the clustering algorithm implements a splitting step to separate showers from different particles. Local maxima of the cells in a cluster are searched for, and then used as the seed cells for a new iteration of the clustering, which may split the original cluster into multiple clusters.

Using the topological clusters as inputs, jets are formed using the so-called Anti- k_t algorithm [55]. The distance parameter R (intuitively the radius of a jet in the ϕ - η plane) can be set at 0.4 or 0.6 in the jet finding algorithm. The jet four-momentum is then defined as the sum of the four-momenta of its constituents. In addition, for simulation samples, stable simulated particles are used as inputs of the jet finding algorithm, and the resulting objects are called truth jets.

Initially, the topological clusters are reconstructed in the electromagnetic (EM) scale, which correctly measures only the energy deposits of the EM showers. A different topological cluster reconstruction adds the calibration of the calorimeter cells to also correctly measure the energy deposits of the hadronic showers. This calibration uses the local cell weighting (LCW) method. This method first classifies a cluster to be either electromagnetic or hadronic, mostly based on the energy density and shower depth. Then it applies energy corrections, which are derived from MC simulation. The LCW method improves the energy resolutions and reduces the

effects of non-compensation, dead material and out-of-cluster leakage, compared to the EM scale. Jets formed from initial clusters are referred to as EM scale jets, and jets formed from clusters with the LCW calibration are referred to as LCW scale jets.

After the jet finding procedure, a jet calibration procedure is implemented, to restore jet energies to best approximate the truth jet level. The jet calibration procedure consists of four steps.

- Pile-up correction: This is applied to fix the energy offset from in-time pile-up and out-of-time pile-up. The correction is derived from MC simulation.
- Origin correction: This is applied to make the calorimeter jet point back to the primary vertex, instead of the geometrical center of the ATLAS detector.
- MC-based jet calibration: This is derived by comparing the jet energy and pseudorapidity of the calorimeter jets, to those of the corresponding truth jets in MC simulation. Based on the topological cluster reconstruction (EM or LCW), the resulting jets are referred to as EM+JES jets or LCW+JES jets, respectively.
- Residual in situ correction: This is derived in situ, and applied to jets in data to account for any residual difference between data and simulation.

This study uses the LCW+JES jets. In the Anti- k_t jet finding procedure, $R = 0.4$ is set.

5.4.2 Jet Selection

Besides signal jets from the hard scattering processes, the outputs from jet reconstruction also include various background objects. The main sources of the background objects are:

- beam-gas events: protons collide with residual gas in the beampipe
- beam-halo events: interactions in the beampipe far away from the ATLAS detector
- cosmic muons
- calorimeter noise

To reduce background objects, four sets of jet quality criteria are introduced, which are called **looser**, **loose**, **medium**, and **tight**. These jet quality criteria sets utilize event information, including cell energy reconstruction quality, energy deposits in the direction of the shower development, and tracks matched to the jets. In this study, jet quality criteria is used in the event selection stage.

Other requirements on jets are also used in this study: jets are required to have $p_T > 25$ GeV and $|\eta| < 2.5$.

To reject jets from pile-up interactions, jets are required to originate from the primary vertex, using the jet vertex fraction (JVF) requirement. JVF is defined as the ratio of the scalar sum of p_T of tracks associated with a jet and originating from the primary vertex, to the scalar sum of p_T of all tracks associated with the jet. The tracks used in the JVF definition are required to have $p_T > 1$ GeV. The JVF requirement is applied to jets with $p_T < 50$ GeV and $|\eta| < 2.4$. The absolute JVF value for these jets has to be greater than 0.5: $|JVF| > 0.5$.

An overlap removal procedure applied to the selected objects is outlined below. The aim of the overlap removal is to avoid ambiguity in the object selection and keep only prompt leptons.

- If any jet is within $\Delta R < 0.2$ of an electron having $p_T > 15$ GeV, the closest jet is discarded to avoid double counting of electrons as jets. This is because we do not explicitly reject electrons in the jet reconstruction procedure.

- We also remove all electrons and muons having $p_T > 15$ GeV and within $\Delta R < 0.4$ of any jet.

5.5 B-tagging

B-jets, jets containing b -hadrons, can be identified (called b -tagging) from their kinematic features [56, 57]. The lifetime of b -hadrons is of the order of 1.5 ps, thus b -hadrons with $p_T = 50$ GeV will typically have a flight length around 4mm before decaying, which results in a secondary vertex, and large impact parameters of tracks. Tagging other jet types (from other quarks or gluons) is usually much harder. This section discusses the b -tagging algorithms.

There are several basic b -tagging algorithms available at ATLAS. These algorithms share several steps: decays of hyperons (baryons containing a strange quark) are rejected; track impact parameter cuts are applied to reject long-lived particles and secondary interactions; pairs of remaining tracks are then used to form vertices; the masses of the vertices are used to reject tracks from K_s , Λ decays, and photon conversions; and the radii of the vertices are compared with the beampipe and pixel layers to reject secondary interactions in the detector material. After these steps, the basic b -tagging algorithms are implemented differently.

- Impact parameter based algorithm

This b -tagging algorithm combines the impact parameter significances of all tracks associated with the jet. Then it uses a likelihood technique to compare the jet with b -jets and light-jets from MC simulation. The inputs to the likelihood are the transverse impact parameter significance, $d_0/\sigma(d_0)$, as well as the longitudinal impact parameter significance, $z_0/\sigma(z_0)$. The likelihood takes the correlations of the two variables into account using 2-dimensional histograms. This algorithm is also referred to as the IP3D algorithm.

- Secondary vertex based algorithms

These algorithms utilize the inclusive vertex of the decay products of a b -hadron. A vertex search first looks for all two-track pairs compatible with a good vertex, using tracks associated to the jet and far from the primary vertex. Then all tracks of the found two-track vertices are combined into an inclusive vertex, using an iterative procedure.

SV0 and SV1 are both secondary vertex based algorithms. The SV0 algorithm uses the decay length significance $L_3 D / \sigma(L_3 D)$, as a discriminating variable between b -jets and light jets. For better discriminating power, the SV1 algorithm uses three variables, which are the invariant mass of all tracks associated to the inclusive vertex, the ratio of the energy sum of the tracks associated with the inclusive vertex to the energy sum of all tracks within the jet, as well as the number of the two-track vertices. These three variables are combined in a likelihood technique. In addition, ΔR between the jet direction and the line from the primary vertex to the secondary vertex is utilized.

- The JetFitter algorithm

The JetFitter algorithm looks into the topology of the b -hadron decays inside a jet. A Kalman filter is utilized to find a line with the primary vertex and the b -vertices, as well as their positions on the line. The discrimination between b -jets and light-jets is then provided by a likelihood technique using the SV1 algorithm variables, and some additional variables such as the flight length significances of the vertices.

The results of the above b -tagging algorithms can be combined using multivariate analysis techniques. The MV1 algorithm, utilizes an artificial neural network, taking the IP3D, SV1, and JetFitter results as inputs. The outputs of the MV1 algorithm

are weights for each jet: the larger weight indicates the higher probability to be a b -jet. The neural network is trained with b -jets as the signal and light-jets as the background.

Fixed cuts on the MV1 weights, referred to as working points, are applied in physics analyses. The working points being widely used are those with b -tagging efficiencies of 60%, 70% or 80%, for b -jets with $p_T > 20$ GeV and $|\eta| < 2.5$ in simulated $t\bar{t}$ events. For the 70% MV1 working point, the rejecting factors for light-jets and c -jets are approximately 130 and 5, respectively.

This study uses the MV1 algorithm and the working point with the 70% b -tagging efficiency. Any selected jets passing the MV1 working point requirement are identified as b -jet candidates. The b -tagging efficiencies in simulation samples are corrected using the measurements [58] in $t\bar{t}$ events, for better agreement between data and simulation. These efficiencies are binned in jet p_T and η .

5.6 Missing Transverse Momentum

In hadron collider events, the momentum sum in the plane transverse to the beamaxis is conserved and before the collision assumed to be zero. The missing transverse momentum, $\mathbf{E}_T^{\text{miss}}$, is defined as the momentum imbalance in the transverse plane, which is the negative vector sum of the momenta in the transverse plane of all particles from a collision event. E_T^{miss} , is defined as the magnitude of the vector $\mathbf{E}_T^{\text{miss}}$. A significant amount of missing transverse momentum provides an indirect measurement for the existence of neutrinos, or other possibly new particles that might have escaped detection. This section discusses the $\mathbf{E}_T^{\text{miss}}$ reconstruction.

$\mathbf{E}_T^{\text{miss}}$ reconstruction [59] mainly uses energy deposits in the calorimeters and reconstructed muons in the muon detectors. Inner detector tracks are also used to recover low- p_T particles which are not reconstructed in the calorimeters. In addition, segment-tagged muons are used to recover muons which do not traverse enough muon

detector layers.

In the $\mathbf{E}_T^{\text{miss}}$ calculation, calorimeter energy deposits are first associated with the reconstructed high- p_T objects in the following specific order: electrons, photons, hadronically decaying τ leptons, jets, and muons. Energy deposits not associated with the above objects are also considered in the so-called soft term. Then, the $\mathbf{E}_T^{\text{miss}}$ is calculated as

$$E_{x(y)}^{\text{miss}} = E_{x(y)}^{\text{miss,e}} + E_{x(y)}^{\text{miss,}\gamma} + E_{x(y)}^{\text{miss,}\tau} + E_{x(y)}^{\text{miss,jet}} + E_{x(y)}^{\text{miss,SoftTerm}} + E_{x(y)}^{\text{miss,}\mu} \quad (5.1)$$

where each term is the negative sum of the momenta of the corresponding objects in the x or y direction.

The terms in the $\mathbf{E}_T^{\text{miss}}$ formula are described below:

- $E_{x(y)}^{\text{miss,e}}$ is calculated for the reconstructed electrons passing the **tight** electron identification requirements and having $p_T > 10$ GeV. The standard ATLAS electron calibration is used.
- $E_{x(y)}^{\text{miss,}\gamma}$ is calculated for the reconstructed photons passing the **tight** photon identification requirements [60] and having $p_T > 10$ GeV. The photons are calibrated at the EM scale.
- $E_{x(y)}^{\text{miss,}\tau}$ is calculated for the reconstructed τ jets passing the **tight** τ identification requirements [61] and having $p_T > 10$ GeV. The LCW calibration and the tau energy scale (TES) correction are used.
- $E_{x(y)}^{\text{miss,jets}}$ is calculated for the reconstructed jets having $p_T > 20$ GeV. The LCW calibration and the jet energy scale (JES) correction are used.
- $E_{x(y)}^{\text{miss,SoftTerm}}$ is calculated for the topological clusters and tracks not associated to the high- p_T objects. The topological clusters, rather than the cells, are used

to suppress noise contributions. They are calibrated using the LCW techniques, and the overlap with the tracks are removed.

- $E_{x(y)}^{\text{miss},\mu}$ is calculated for the reconstructed muons having $p_T > 10$ GeV. To correctly treat calorimeter energy deposits produced by the muons, this term is calculated differently for isolated and non-isolated muons, where non-isolated muons are defined as muons within $\Delta R < 0.3$ of any reconstructed jet.

6

Event Selection and Background Estimation

The event-level analysis for the $t\bar{t}V$ measurement is discussed in this chapter. Section 6.1 describes the event selections and background estimations that are common to all analysis channels. Sections following this describe the event-level analysis specific for each analysis channel.

6.1 Common Event Selection and Background Estimation

Event pre-selection requirements, which are applied before other event-level selection requirements, are as follows. Unless otherwise stated, the pre-selection requirements are applied to both data and simulation events.

- Good runs list

As mentioned in Chapter 4, data events are required to be from runs in the good runs list (GRL). The GRL requirement is not applied to simulation events.

- Trigger

Events are required to be collected using high- p_T single lepton trigger paths, whereby at least one high- p_T electron or muon is identified by the trigger sys-

tem. Two single electron triggers are used, with p_T thresholds of 24 GeV and 60 GeV. Similarly, two single muon triggers are used, with p_T thresholds of 24 GeV and 36 GeV. In both cases, the triggers with the lower p_T thresholds have isolation requirements on the lepton being triggered. This results in some inefficiencies for high- p_T leptons, but is recovered by the triggers with the higher p_T thresholds. Both data and simulation events need to satisfy the trigger requirements (the triggers are also part of the ATLAS simulation).

- LArError and TileError

To reduce the effects of noise bursts and data corruptions in the Liquid Argon and Tile calorimeters, events are required not to have any error from the corresponding quality checks. The errors from these checks are named as LArError and TileError, respectively.

- Incomplete Events

During data taking runs, TTC restart procedures are sometimes implemented to fix technical problems of certain sub-systems of the ATLAS detector. Incomplete events due to the TTC restart procedures are removed.

- Primary Vertex

The reconstruction of primary vertices was introduced in Chapter 5. Events are required to have a reconstructed primary vertex with at least four associated tracks of $p_T > 400$ MeV and satisfying certain quality requirements. This is designed to reject non-collision background events.

- Cosmic Muon Veto

An event is discarded if two muons (before the object selections) have opposite-sign transverse impact parameters of $|d_0| > 0.5$ mm, as well as an azimuthal

angle difference of $|\Delta\phi| > 3.10$. This is designed to reduce events from cosmic-ray muons traversing the detector.

- Jet Cleaning

In Chapter 5, four sets of jet quality criteria were introduced. The **looser** jet quality criteria is used in this study: if an event contains any jet failing the **looser** criteria, the event is discarded. This requirement is intended to remove events with instrumental effects, such as beam-gas, beam-halo, cosmic muons, and calorimeter noise.

- Electron-Muon Overlap Removal

If an event contains an electron and a muon that have $|\Delta\theta| < 0.005$ and $|\Delta\phi| < 0.005$ between them, the event is discarded. This requirement is intended to reduce background events where a muon radiates a hard photon by bremsstrahlung, and the photon is reconstructed as an electron (which shares an inner detector track with the muon).

- Trigger Matching

If no selected lepton is matched to the corresponding trigger object(s), an event is discarded. A selected electron (muon) is considered to be trigger-matched, if it is within a cone of $\Delta R < 0.15$ of an electron (muon) reconstructed by the trigger. Only leptons with $p_T > 25$ GeV are considered in trigger matching. The trigger matching requirement removes events where the triggers are not caused by the selected leptons.

- Truth Matching

For a simulated event, if any reconstructed lepton is not matched to the corresponding leptons in the truth record, the event is discarded. A reconstructed

electron (muon) is considered to be truth-matched, if it is within a cone of $\Delta R < 0.15$ of a prompt electron (muon) in the truth record, from a W , Z , or tau lepton decay. The truth matching requirement ensures the simulated events are from physics processes with real prompt leptons.

After the pre-selection requirements, the selected leptons are used to determine four distinct analysis channels. The leptons are sorted according to the transverse momenta (p_T), in decreasing order. The two opposite-sign lepton channel (2OSL) requires events to have two leptons with $p_T > 15$ GeV and opposite electric charge, while the two same-sign lepton channel (2SSL) requires events to have two leptons with $p_T > 25$ GeV and the same electric charge. To avoid overlap with the three lepton channel, both the 2OSL and 2SSL channels veto events having an additional lepton with $p_T > 15$ GeV.

For the three lepton channel (3L), events are required to have three leptons with $p_T > 15$ GeV, and for the four lepton channel (4L), events are required to have at least four leptons with $p_T > 7$ GeV. To avoid overlap between the 3L and 4L channels, events passing both the 3L and 4L selections are assigned to the 3L channel and removed from the 4L channel. In addition, the overlap between the 4L channel and the dilepton channels is found to be negligible. Due to the trigger matching requirement, the leading lepton has $p_T > 25$ GeV in all analysis channels.

The backgrounds in this study are of two categories:

- Physics backgrounds:

The physics backgrounds constitute events with only well-identified prompt leptons, originating from Standard Model processes. These backgrounds are estimated with Monte Carlo simulation. By default, the physics backgrounds are normalized using the integrated luminosity and the corresponding theoretical cross sections. For the WZ and ZZ processes, the normalizations are

floated in the final likelihood fit, and constrained by certain control regions. This approach does not need to include the theoretical uncertainties on the WZ and ZZ cross sections, and is found to eventually reduce the uncertainties on the $t\bar{t}V$ cross section measurements.

- Instrumental backgrounds:

The instrumental backgrounds constitute events with one or more mis-identified or non-prompt lepton (fake lepton background), and dilepton events where the charge of one lepton is mis-identified (charge mis-ID background). These backgrounds are estimated with various data-driven methods. One exception is the fake lepton background in the 2OSL channel, where this background is very small compared with the physics backgrounds. For this channel, only MC simulation is used for the fake lepton background estimation.

6.2 Two Same-sign Lepton Analysis

The 2SSL analysis channel mostly targets the $t\bar{t}W$ process. The $t\bar{t}W$ process can produce events with two same-sign leptons when the associated W boson and one W boson from the decay of the top quarks decay leptonically. The other W boson from the top quarks can decay leptonically or hadronically.

The $t\bar{t}Z$ process also contributes to the 2SSL final state, when the associated Z boson decays to two leptons, where one lepton is not reconstructed or identified, and one W boson from the decay of the top quarks decays leptonically. The other W boson from the top quarks can decay leptonically or hadronically. In the 2SSL channel, the $t\bar{t}Z$ contribution is much smaller than the $t\bar{t}W$ contribution due to the smaller $t\bar{t}Z$ cross section, the smaller branch ratio for the Z to decay leptonically and the additional probability to miss one of the Z leptons.

We select events with two same-sign leptons and other kinematic requirements

(described in section 6.2.1). With the selected events, we define a 3-dimensional phase space and a likelihood function to extract the signal cross sections (described in section 6.2.6).

The main backgrounds in the 2SSL signal regions vary according to the lepton flavor. The charge mis-ID background (described in section 6.2.2) is prevalent in the ee and $e\mu$ same-sign channels. The fake lepton background (described in section 6.2.3) is significant in all the ee , $e\mu$ and $\mu\mu$ same-sign channels. These two instrumental backgrounds are estimated using data-driven methods. Backgrounds from physics processes with real prompt leptons include diboson, $W^\pm W^\pm$, tZ , and $t\bar{t}H$ production, among which the WZ process is the largest. These physics backgrounds are significantly smaller compared with the instrumental backgrounds, and estimated using MC simulation.

6.2.1 Event Selection

In the 2SSL analysis channel, different layers of kinematic regions are defined: pre-selection region, grand signal region (within the pre-selection region), and signal region (within the grand signal region).

Below are the event selection requirements that are used to define the 2SSL pre-selection region:

- Two same-sign identified leptons (ee , $e\mu$, $\mu\mu$), both with $p_T > 25$ GeV.

The p_T threshold of 25 GeV is found to reject more background without a significant loss of signal, and thus provide better sensitivity, compared to using the p_T threshold of 15 GeV.

- Veto events having more than two leptons with $p_T > 15$ GeV.

This veto is to avoid overlap with the 3L analysis channel. In addition, it reduces the contributions from diboson production (WZ , ZZ).

- The 2SSL events are then separated into three channels: ee , $e\mu$, or $\mu\mu$, depending on the flavor of the lepton pair.

Background compositions are different for the ee , $e\mu$, and $\mu\mu$ channels. Thus, separating events into these three channels increases the overall sensitivity.

- For the ee and $\mu\mu$ channels, events with $m_{ll} < 15$ GeV are removed.

This requirement is intended to reject events that contain the leptonic decay of heavy flavor mesons, such as J/Ψ and Υ mesons.

- Events are required to have at least one b -jet ($N_{b\text{-jets}} \geq 1$).

For the $t\bar{t}W$ and $t\bar{t}Z$ processes, two b -quarks are produced from the top quark decays. Therefore, this requirement rejects events from diboson production, while keeping events from the $t\bar{t}V$ processes. (As described in Chapter 5, the p_T requirement on the jets (including the b -jets) is $p_T > 15$ GeV.)

In addition to the above pre-selection requirements, the so-called grand signal region is defined with the H_T requirement.

- Events are required to have $H_T > 240$ GeV.

H_T is calculated as the scalar sum of the p_T of all selected jets and charged leptons in an event. The signal contribution is found to be negligible for events with $H_T < 240$ GeV. Thus, these low H_T events are designated a control regions and used for a fake lepton measurement.

In addition to the grand signal region requirements, the 2SSL signal region is further defined with the following requirements.

- For the ee channel, events with $75 \text{ GeV} < m_{ee} < 105 \text{ GeV}$ are removed.

This requirement is intended to reject the $Z \rightarrow ee$ events where the charge of one electron is mis-identified. It is not imposed on the $\mu\mu$ channel, because the probability of mis-identifying muon charges of the $Z \rightarrow \mu\mu$ events is found to be negligible.

- The transverse missing momentum is required to be $E_T^{\text{miss}} > 40 \text{ GeV}$.
- The total number of jets in an event is required to be $N_{\text{jets}} \geq 2$.

The cuts of $E_T^{\text{miss}} > 40 \text{ GeV}$ and $N_{\text{jets}} \geq 2$ are used to reduce backgrounds, especially the fake lepton background. However, they are relatively loose, in order to keep enough events and conduct a binned fit in the next step.

- $N_{\text{b-jets}} \geq 2$.

This requirement can further reject events from diboson production. Events with $N_{\text{b-jets}} = 1$ do contain some contributions from the $t\bar{t}V$ processes, where one b -jet is not identified. One reason that these events are removed is the 3L analysis channel uses a portion of them for its fake rate measurement.

6.2.2 Backgrounds from Charge Mis-identification

This background consists of events with two opposite-sign leptons where one lepton has its charge mis-identified. The charge mis-ID of muons is negligible as seen by examining the Z peak in data with two same-sign muons, but the charge mis-ID of electrons is an important instrumental background in the same-sign ee and $e\mu$ channels. The dominant mechanism of electron charge mis-ID is photon conversion: an electron radiates a photon and the photon converts to two opposite-sign electrons, where the wrongly signed electron is identified.

This background is estimated in a fully data-driven approach. Charge mis-ID rates, defined as the probability of mis-identifying the charge of an identified lepton,

are measured in a control region of data (see below). Then these rates are applied to data events with two opposite-sign leptons.

Given the charge mis-ID rates for each individual lepton, designated as $\varepsilon_{lep1}^{mis-ID}$ and $\varepsilon_{lep2}^{mis-ID}$, an event weight is computed and applied to each event in the opposite-sign ee and $e\mu$ samples to obtain the total charge mis-ID background. The event weight applied is given by

$$w = \frac{\varepsilon_{lep1}^{mis-ID} + \varepsilon_{lep2}^{mis-ID} - 2\varepsilon_{lep1}^{mis-ID}\varepsilon_{lep2}^{mis-ID}}{1 - (\varepsilon_{lep1}^{mis-ID} + \varepsilon_{lep2}^{mis-ID} - 2\varepsilon_{lep1}^{mis-ID}\varepsilon_{lep2}^{mis-ID})} \quad (6.1)$$

where the charge mis-ID rate is set to zero in the case of muons.

Charge Mis-ID Rates

We follow a well-understood method to measure the charge mis-ID rates. A sample of events is selected for the charge mis-ID measurement (called charge mis-ID control region) as follows:

- Two same-sign identified electrons with $p_T > 25$ GeV.
- Veto events having more than two leptons with $p_T > 15$ GeV.
- Require $75 < M_{ee} < 105$ GeV (a 30 GeV mass window around the Z mass).

Note that the control region has no overlap with the previously defined grand signal region. Both the opposite-sign and same-sign events are utilized. The opposite-sign events are mostly from the $Z \rightarrow e^+e^-$ processes, while the same-sign events are mostly $Z \rightarrow e^+e^-$ events with one electron's charge mis-identified.

Charge mis-ID rates are parameterized with $|\eta|$ and p_T because they are highly depending on the detector regions (the ATLAS detector material is $|\eta|$ -dependent), and the electron energies. The $|\eta|$ and p_T binning is shown below, and both the leading and sub-leading leptons are separated in $7 * 6 = 42$ bins.

- $|\eta|$ binning: 0-0.8, 0.8-1.2, 1.2-1.5, 1.5-1.8, 1.8-2, 2-2.25, 2.25-2.47
- p_T binning (GeV) : 25-35, 35-45, 45-55, 55-65, 65-100, > 100

We use a likelihood-based method to measure the charge mis-ID rates. For the kinematic region having a bin i leading lepton (with a charge mis-ID rate of ϵ_i) and a bin j sub-leading lepton (with a charge mis-ID rate of ϵ_j), we have the number of events $N^{ij} = N_{SS}^{ij} + N_{OS}^{ij}$, where N_{SS}^{ij} (N_{OS}^{ij}) is the number of same-sign (opposite-sign) events. Thus, the probability of observing N_{SS}^{ij} same-sign events can be expressed as a Poisson probability:

$$f(N_{SS}^{ij}; \lambda) = \frac{\lambda^{N_{SS}^{ij}} e^{-\lambda}}{N_{SS}^{ij}!} \quad (6.2)$$

where $\lambda = (\epsilon_i + \epsilon_j)N^{ij}$.

Summing the probabilities of all the kinematic regions in the dilepton phase space, taking the negative log likelihood ($-\ln(L)$), and simplifying algebraically, one can obtain:

$$-\ln L(\epsilon_i, \epsilon_j | N_{SS}, N) \approx - \sum_{i,j} \ln(N^{ij}(\epsilon_i + \epsilon_j)) N_{SS}^{ij} - N^{ij}(\epsilon_i + \epsilon_j) \quad (6.3)$$

This log likelihood function can then be maximized to obtain the charge mis-ID rates and statistical errors of all bins.

The contamination of non- Z events in the Z mass window is estimated using mass sidebands. As shown in Fig. 6.2, the $60 < M_{ee} < 75$ GeV and $105 < M_{ee} < 120$ GeV mass windows are used as sidebands. The events in the sidebands are taken to be the non- Z contamination in the Z mass window (noting the sum of the sideband widths is also 30 GeV), which is then subtracted from the events in the Z mass window.

The advantage of using the likelihood method over a traditional tag-and-probe method is that all the events in the same-sign/opposite-sign Z peaks are utilized.

Thus, the method allows us to better describe the charge mis-ID background with finer binning of the charge mis-ID rates. The corresponding statistical uncertainties are also reduced. The measured charge mis-ID rates with their statistical uncertainties are shown in Fig. 6.1.

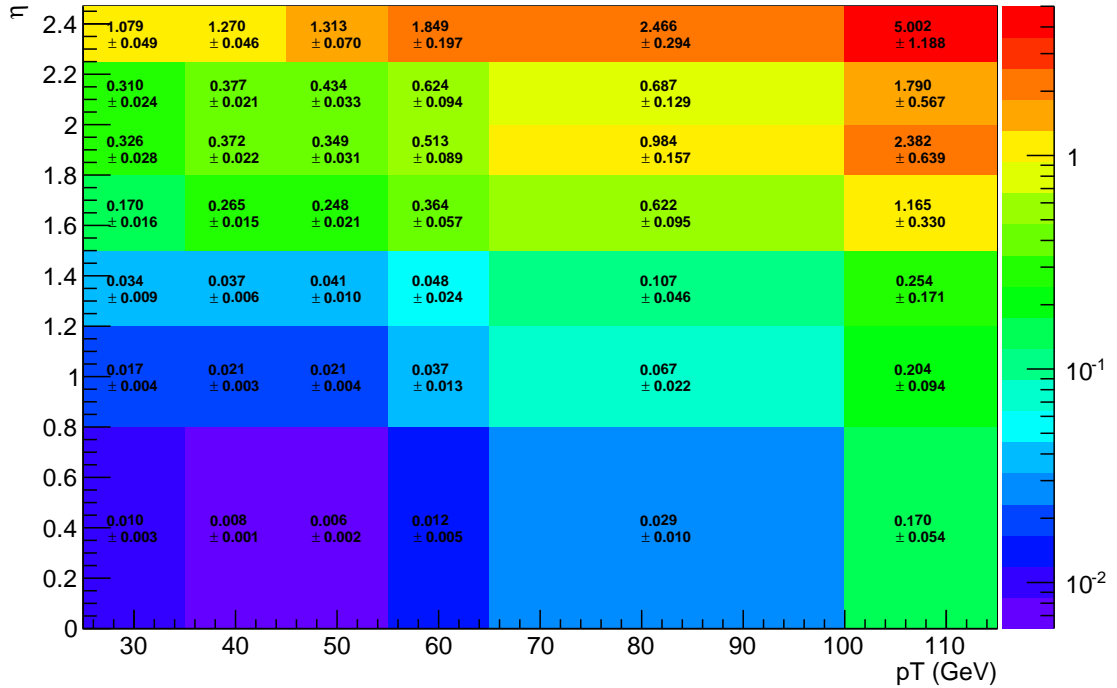


FIGURE 6.1: The electron charge mis-ID rates with their statistical uncertainties (in %) measured in data. The largest $|\eta|$ and p_T bins contain the overflow for higher values.

Loose electrons are used for the fake lepton background estimation, and defined as electrons having the same definition as the analysis electrons (tight electrons), but failing the impact parameter or isolation requirements. Charge mis-ID rates of loose electrons are used in the overlap removal of the charge mis-ID and fake lepton background estimates (see Section 6.2.3). To measure these, the above method is used again, by including both tight and loose electrons in the likelihood fit, and bin the electrons by ID (tight, loose), $|\eta|$ and p_T .

Finally, a closure test is conducted by comparing the same-sign Z peak observed in data with the same-sign Z peak estimated using the data-driven method. The number of events is 15023 ± 123 from the observation, and 14728 ± 12 from the estimation (the errors are statistical uncertainties only). The difference is 2.0%, which indicates the method works well at describing charge mis-ID in $Z \rightarrow ee$ events (within the systematic uncertainties which are of the order of 25%). Because of this good agreement, we do not apply additional correction or systematic uncertainties. The closure test is shown in Fig. 6.2. The figure also indicates that the $75 < M_{ee} < 105$ GeV mass window includes both the same-sign and opposite-sign Z peaks.

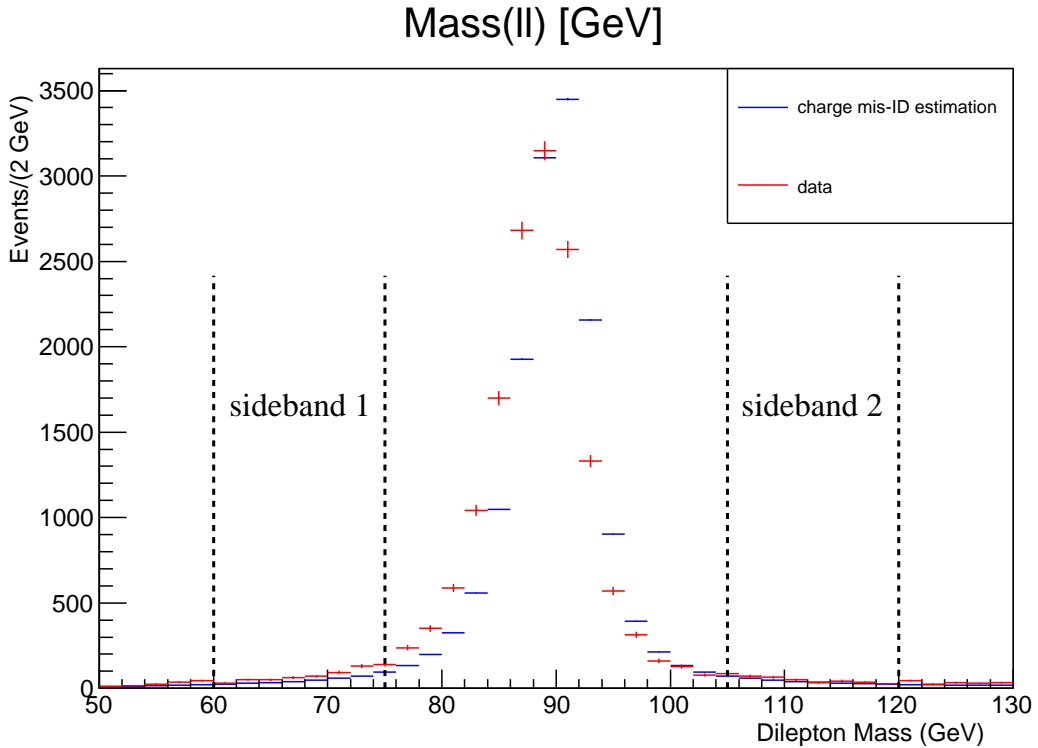


FIGURE 6.2: Results of the closure test performed by comparing the same-sign Z peak observed in data with the same-sign Z peak estimated using the data-driven method. The total yields differ by 2.0%. Also shown are the sideband regions used to subtract backgrounds in the nominal rate measurement.

6.2.3 Background from Fake Leptons

This background occurs in events where one lepton is either non-prompt (produced in a heavy-flavor hadron decay or from photon conversion in a hadronic jet) or mis-identified (from a jet with a large electromagnetic fraction). These two categories together are referred to as fake leptons in this documentation. The 2SSL channel uses a technique known as the fake factor method to estimate the background.

The fake factor method utilizes loose leptons. Loose leptons have the same definitions as analysis (tight) leptons, except that the impact parameter and isolation cuts are removed. However, the $|d_0/\sigma(d_0)| < 3$ cut is kept for loose electrons. This cut reduces the overlap between the charge mis-ID and fake lepton backgrounds because it significantly decreases the charge mis-ID rates of loose electrons.

With loose leptons, the fake factor can be defined as $f = N_{\text{tight}}/N_{\text{loose}}$, where N_{tight} is the number of fake leptons passing tight selection, and N_{loose} is the number of fake leptons passing loose selection, but failing tight selection.

The expression for the total number of fake lepton events (with two tight leptons) from the fake factor method is given by:

$$N_{\text{fakes}} = \left[\sum_{N_{LT}} f_1 + \sum_{N_{TL}} f_2 - \sum_{N_{LL}} f_1 f_2 \right]_{\text{data}} - \left[\sum_{N_{LT}} f_1 + \sum_{N_{TL}} f_2 - \sum_{N_{LL}} f_1 f_2 \right]_{\text{MC,prompt}} \quad (6.4)$$

N_{TL} (N_{LT}) represents the number of events where the first lepton is a tight (loose) lepton and the second is loose (tight), while N_{LL} represents the number of events with two loose leptons. For ee and $\mu\mu$ events, the leptons are ranked according to p_T . For $e\mu$ events, we take the electron to be the first lepton, and the muon to be the second lepton. The f_i is then the fake factor for the i th lepton of the event. In Equation 6.4, the contribution of real prompt leptons is estimated using MC simulation and subtracted from data.

A brief derivation of the above fake factor method formula is given below. First of all, the total number of fake lepton events is

$$N_{\text{fakes}} = [N_{FR} + N_{RF} + N_{FF}] \quad (6.5)$$

N_{FR} (N_{RF}) represents the number of events where the first lepton is a fake (real) lepton and the second is real (fake), while N_{FF} represents events with two fake leptons. This expression is true for the tight-tight (TT), tight-loose (TL), loose-tight (LT), and loose-loose (LL) samples.

From the number of events in the loose-tight sample, we have

$$\begin{aligned} \left[\sum_{LT} (N_{\text{data}} - N_{\text{MC,prompt}}) f_1 \right] &= (N_{LT,FR} + N_{LT,RF} + N_{LT,FF}) f_1 \\ &= N_{TT,FR} + N_{LT,RF} f_1 + N_{TT,FF} \end{aligned} \quad (6.6)$$

In the loose-tight sample, the contribution from real prompt leptons are completely subtracted using MC simulation. The remainder can be regarded as the fake lepton events in the loose-tight samples, which consists of FR events, RF events and FF events. Therefore, by multiplying with the corresponding fake factor, we obtain the FR and FF events in the analysis region (the tight-tight sample), as well as one additional term for the RF events in the loose-tight region.

Similarly, we have

$$\begin{aligned} \left[\sum_{TL} (N_{\text{data}} - N_{\text{MC,prompt}}) f_2 \right] &= (N_{TL,FR} + N_{TL,RF} + N_{TL,FF}) f_2 \\ &= N_{TL,FR} f_2 + N_{TT,RF} + N_{TT,FF} \end{aligned} \quad (6.7)$$

Additionally, from the number of events in the loose-loose sample, we have

$$\begin{aligned} \left[\sum_{LL} (N_{\text{data}} - N_{\text{MC,prompt}}) f_1 f_2 \right] &= (N_{LL,FR} + N_{LL,RF} + N_{LL,FF}) f_1 f_2 \\ &= N_{TL,FR} f_2 + N_{LT,RF} f_1 + N_{TT,FF} \end{aligned} \quad (6.8)$$

In the loose-loose sample, after subtracting the contribution from real prompt leptons, the remainder consists of FR events, RF events and FF events in the loose-loose sample. By multiplying with the fake factors, we obtain the FF events in the analysis region (the tight-tight sample), as well as two additional terms for the RF (FR) events in the loose-tight (tight-loose) region.

Finally, combining the above three equations and simplifying algebraically, we obtain Equation 6.4. Note the N_{fakes} in Equation 6.4 is the number of fake lepton events in the tight-tight sample, $N_{TT,FR} + N_{TT,RF} + N_{TT,FF}$.

Fake Factor Measurement

The fake factors are measured in a fake lepton control region defined as follows:

- Require two same-sign identified leptons ($p_T > 25$ GeV).
- Veto events having more than two leptons with $p_T > 15$ GeV.
- The events are then separated into three channels: ee , $e\mu$, or $\mu\mu$.
- For ee or $\mu\mu$ channels, events with $m_{ll} < 15$ GeV are vetoed.
- Separate $N_{\text{b-jets}} = 0$ and $N_{\text{b-jets}} \geq 1$ events, to separate fake leptons coming from different sources. The physics processes contributing to fake lepton events are different between the $N_{\text{b-jets}} = 0$ and $N_{\text{b-jets}} \geq 1$ final states.
- Veto events with $H_T > 240$ GeV to remove overlap with the signal region and ensure no $t\bar{t}V$ contribution. No N_{jets} or E_T^{miss} cut is applied.
- Events with $75 \text{ GeV} < M_{ee} < 105 \text{ GeV}$ are removed for the ee channel to reject charge mis-ID events.

The leptons are here binned in lepton flavor (e and μ) and p_T (25-36 GeV and > 36 GeV). The binning is limited because fake lepton statistics are suppressed by

the isolation and impact parameter requirements. The threshold of 36 GeV is chosen to ensure the high- p_{T} muon bin has enough statistics. It is also motivated by the p_{T} threshold of the high- p_{T} muon trigger. Limited statistics however do not permit an additional bin above the high- p_{T} electron trigger threshold of 60 GeV.

A likelihood function is constructed based on the agreement between data and expectation in the ee , $e\mu$, and $\mu\mu$ channels. The expectation includes the MC-based prompt lepton contribution, the charge mis-ID background, and finally the data-driven fake lepton background. The fake lepton background has an explicit dependence on the fake factors f_{ℓ}^n , where $\ell = e$ or μ , and n represents the binning of the fake factors in lepton p_{T} . This likelihood is written as:

$$-\ln L(f_{\ell}^n) \approx -\sum_{i,j} \ln(N_{\text{exp}}^{ij}(f_{\ell}^n)) N_{\text{data}}^{ij} - N_{\text{exp}}^{ij}(f_{\ell}^n) \quad (6.9)$$

$$N_{\text{exp}}^{ij}(f_{\ell}^n) = N_{\text{fakes}}^{ij}(f_{\ell}^n) + N_{\text{prompt,MC}}^{ij} + N_{\text{qmis-ID}}^{ij} \quad (6.10)$$

where $N_{\text{data(exp)}}^{ij}$ is the total number of the observed (expected) events in the kinematic region with a bin i leading lepton and a bin j sub-leading lepton, and N_{fakes} is defined in Equation 6.4. $N_{\text{prompt,MC}}$ is the number of the prompt lepton events estimated from MC, and $N_{\text{qmis-ID}}$ is the number of the charge mis-ID events from the estimation described in Section 6.2.2. The likelihood function can then be minimized to obtain the fake factors (f_e and f_{μ}) and statistical errors of all bins. The measured fake factors with their statistical uncertainties are shown in the top half of Table 6.1.

We also measure the fake factors using MC samples for comparison. The $W+\text{jets}$, $Z+\text{jets}$, $t\bar{t}$, single top, and WW samples are used (normalized with their theoretical cross sections). Then we select leptons not matched to any lepton in the truth record, but passing the loose lepton ID. From the selected leptons, we calculate the ratio of leptons passing the tight lepton ID, to leptons failing the tight lepton ID. Only events with $H_{\text{T}} < 240$ GeV are used, to be the same as the measurement in data.

Table 6.1: The fake factors with their statistical uncertainties for electrons and muons measured in data, followed by a cross-check conducted with MC (including combined samples and individual $t\bar{t}$ and W +jets samples). Only events with $H_T < 240$ GeV are used to calculate these values.

Data	$N_{b\text{-jets}} = 0$	$N_{b\text{-jets}} \geq 1$
electrons, $p_T = 25 - 36$ GeV	0.59 ± 0.11	0.20 ± 0.08
electrons, $p_T > 36$ GeV	1.28 ± 0.21	0.21 ± 0.19
muons, $p_T = 25 - 36$ GeV	0.10 ± 0.06	0.04 ± 0.03
muons, $p_T > 36$ GeV	0.93 ± 0.41	0.09 ± 0.10
Combined MC	$N_{b\text{-jets}} = 0$	$N_{b\text{-jets}} \geq 1$
electrons, $p_T = 25 - 36$ GeV	0.74 ± 0.10	0.09 ± 0.02
electrons, $p_T > 36$ GeV	0.95 ± 0.15	0.24 ± 0.05
muons, $p_T = 25 - 36$ GeV	0.07 ± 0.03	0.02 ± 0.01
muons, $p_T > 36$ GeV	0.09 ± 0.03	0.07 ± 0.02
$t\bar{t}$ MC	$N_{b\text{-jets}} = 0$	$N_{b\text{-jets}} \geq 1$
electrons, $p_T = 25 - 36$ GeV	0.03 ± 0.01	0.07 ± 0.01
electrons, $p_T > 36$ GeV	0.10 ± 0.03	0.18 ± 0.04
muons, $p_T = 25 - 36$ GeV	0.02 ± 0.01	0.02 ± 0.01
muons, $p_T > 36$ GeV	0.05 ± 0.02	0.07 ± 0.02
W +jets MC	$N_{b\text{-jets}} = 0$	$N_{b\text{-jets}} \geq 1$
electrons, $p_T = 25 - 36$ GeV	0.80 ± 0.17	0.33 ± 0.29
electrons, $p_T > 36$ GeV	0.74 ± 0.16	0.18 ± 0.15
muons, $p_T = 25 - 36$ GeV	0.14 ± 0.07	-
muons, $p_T > 36$ GeV	0.08 ± 0.05	-

The results are shown in the bottom half of Table 6.1, which can be compared with the fake factor dependence on b -jet multiplicity and p_T observed in data. We find a very different composition of processes contributing in the 0-tag region than the 1-tag region, so it is difficult to directly compare the fake factors in both regions. The lower fake factors in the 1-tag region indicate that the processes that populate the 1-tag region are much more likely to give loose lepton objects than the processes that populate the 0-tag region.

One thing to note is, we measure the fake factors in the $H_T < 240$ GeV region, while the signal region is within the $H_T > 240$ GeV region. To estimate any potential bias, we use MC samples to measure the fake factors in low- H_T and high- H_T regions.

Only $N_{b\text{-jets}} \geq 1$ events are studied because both the fake factor measurement and signal region have this requirement. The results are shown in Table 6.2 and the fake factors in low H_T and high H_T regions are found to be in good agreement.

Table 6.2: The fake factors with their statistical uncertainties for electrons and muons measured in low- H_T and high- H_T regions using MC samples.

	$H_T < 240$ GeV	$H_T > 240$ GeV
electrons, $p_T = 25 - 36$ GeV	0.09 ± 0.02	0.09 ± 0.02
electrons, $p_T > 36$ GeV	0.24 ± 0.05	0.22 ± 0.03
muons, $p_T = 25 - 36$ GeV	0.020 ± 0.005	0.036 ± 0.007
muons, $p_T > 36$ GeV	0.07 ± 0.02	0.08 ± 0.02

Overlap Between the Fake Lepton and Charge Mis-ID Backgrounds

The potential overlap between the data-driven estimates of the charge mis-ID and fake lepton backgrounds is estimated as follows. First, a template for fake lepton background is produced for the opposite-sign events, using the same selection and method as the same-sign events, except the total charge requirement. The charge mis-ID rates are then applied to the opposite-sign fakes estimate to obtain a sample of events which belong to both the fake lepton and charge mis-ID backgrounds. Note here the charge mis-ID rates for both tight and loose leptons are utilized. This template is then subtracted from the total fake lepton background estimate, along with the “MC, prompt” term in Equation 6.4.

Looking at the signal regions, the charge mis-ID contribution being subtracted accounts for 2-5% of the fake lepton estimation before the subtraction (the “data” term in Equation 6.4). However, without the d_0 significance cut on loose electrons, the overlap between the charge mis-ID and fake lepton backgrounds is around 40% (ee channel), or 30% ($e\mu$ channel). The prompt lepton contribution being subtracted only accounts for 2-3% of the fake lepton estimation before the subtraction.

6.2.4 Control region

To evaluate the accuracy of background predictions, a control region is defined as follows, in which various kinematic distributions will be compared:

- Require two same-sign identified leptons ($p_T > 25$ GeV).
- Veto events having more than two leptons with $p_T > 15$ GeV.
- The events are then separated into three channels: ee , $e\mu$, or $\mu\mu$.
- For ee or $\mu\mu$ channels, events with $m_{ll} < 15$ GeV are vetoed.
- Require $N_{b\text{-jets}} \geq 1$.
- Veto events with $H_T > 240$ GeV, which significantly suppresses the contribution of the $t\bar{t}V$ processes to the control region. No N_{jets} or E_T^{miss} cuts are applied.

This control region is the same as the fake factor measurement region, except that the requirement of $75 \text{ GeV} < M_{ee} < 105 \text{ GeV}$ is removed. This is intended to also evaluate the charge mis-ID background modeling.

The background compositions in the ee , $e\mu$ and $\mu\mu$ channels are drastically different. The ee channel has a considerable fraction of events where the charge of one electron is mis-identified, while the $e\mu$ and $\mu\mu$ channels primarily contain fake lepton background and prompt lepton background from WZ production.

Overall, our background modeling gives an adequate description of the experimental data. The level of agreement can be evaluated from the distributions in:

- jet multiplicity (see Fig. 6.3),
- b -jet multiplicity (see Fig. 6.4),
- E_T^{miss} (see Fig. 6.5),

- H_T (see Fig. 6.6), and
- p_T of leptons (see Figs. 6.7, 6.8, and 6.9).

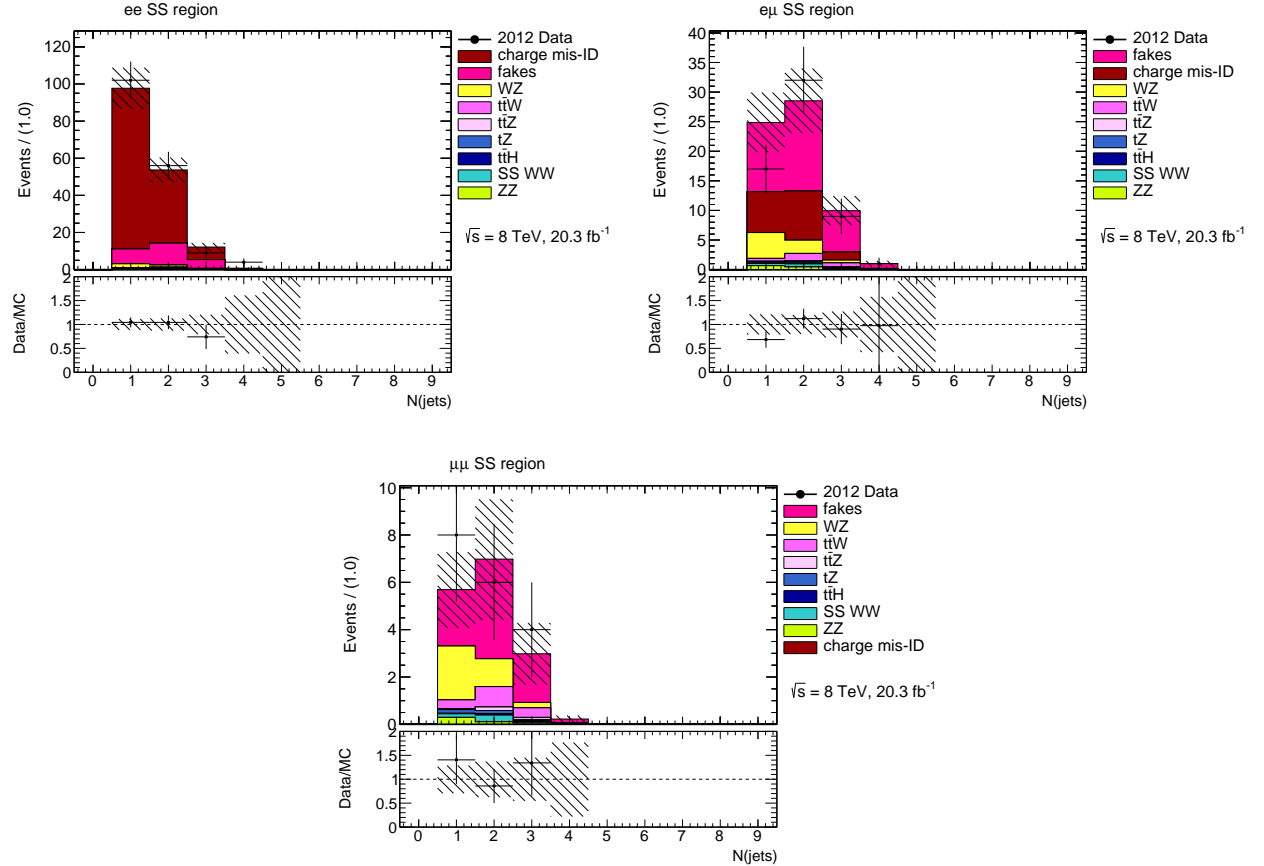


FIGURE 6.3: The distributions in jet multiplicity for two same-sign lepton final states: ee (top left), $e\mu$ (top right), and $\mu\mu$ (lower middle). The events are required to contain at least one b -tagged jet and $H_T < 240$ GeV. The rate of events from $t\bar{t}V$ is negligible in comparison to the other processes. The instrumental backgrounds are predicted using data-driven methods. The hatched areas include both statistical and systematic uncertainties.

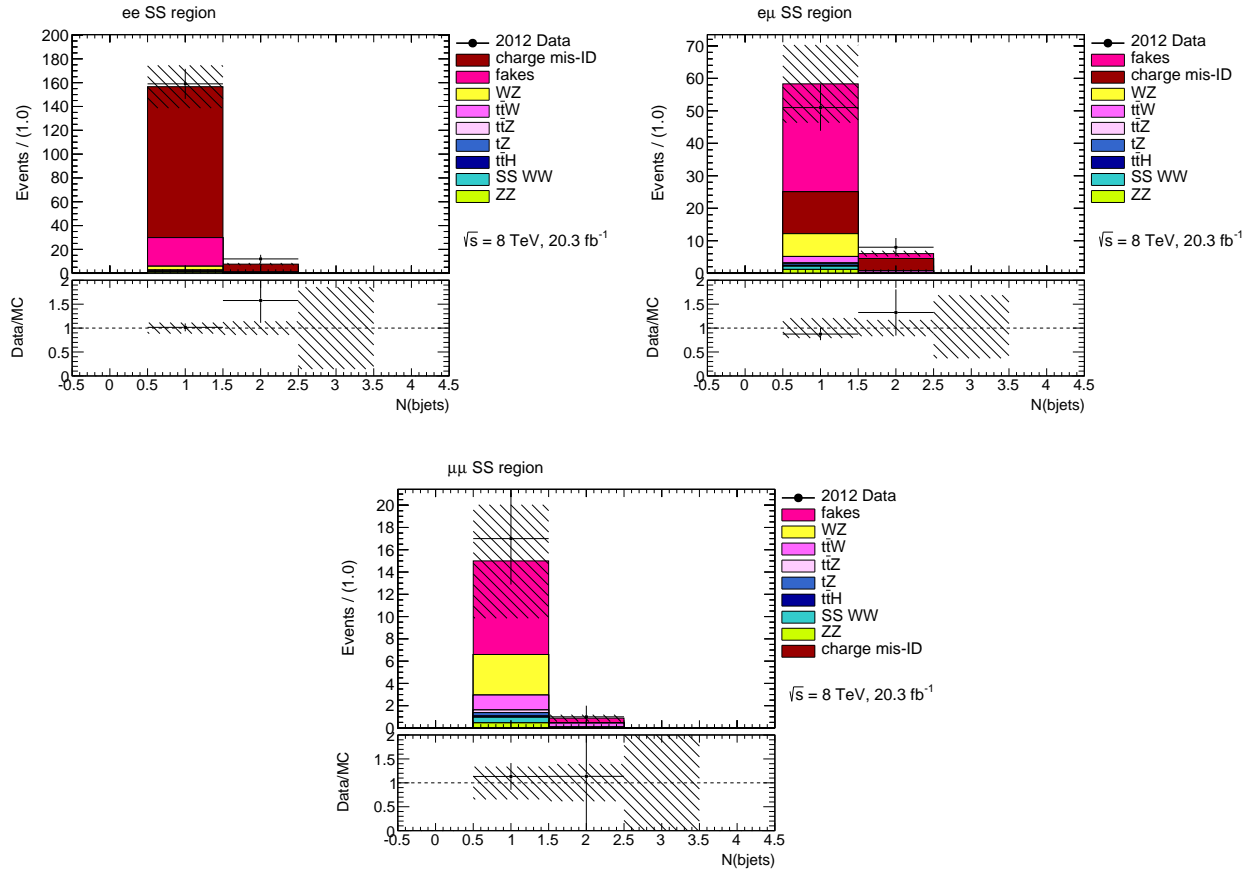


FIGURE 6.4: The distributions in b -tagged jet multiplicity for two same-sign lepton final states: ee (top left), $e\mu$ (top right), and $\mu\mu$ (lower middle). The events are required to contain at least one b -tagged jet and $H_T < 240$ GeV. The rate of events from $t\bar{t}V$ is negligible in comparison to the other processes. The instrumental backgrounds are predicted using data-driven methods. The hatched areas include both statistical and systematic uncertainties.

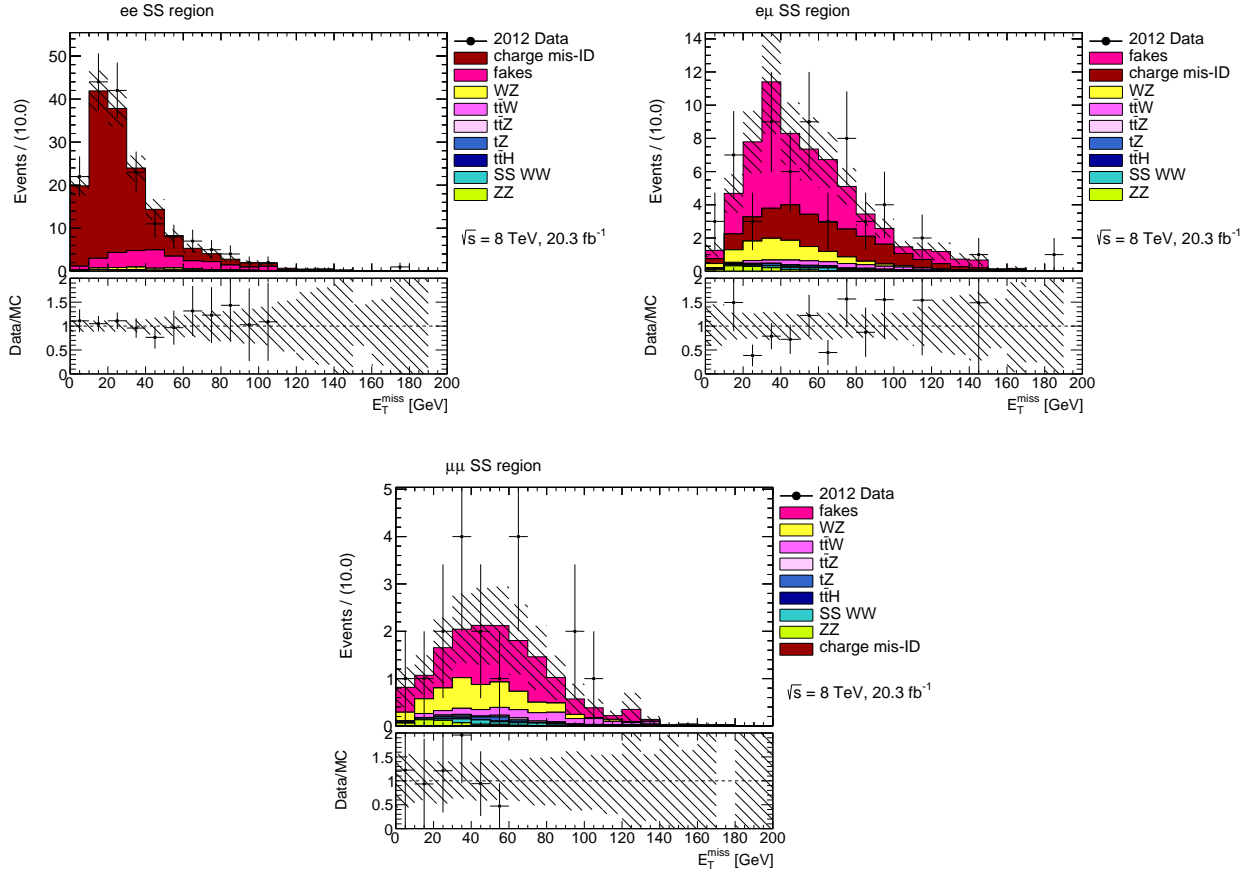


FIGURE 6.5: The distributions in missing transverse momentum for two same-sign lepton final states: ee (top left), $e\mu$ (top right), and $\mu\mu$ (lower middle). The events are required to contain at least one b -tagged jet and $H_T < 240$ GeV. The rate of events from $t\bar{t}V$ is negligible in comparison to the other processes. The instrumental backgrounds are predicted using data-driven methods. The hatched areas include both statistical and systematic uncertainties.

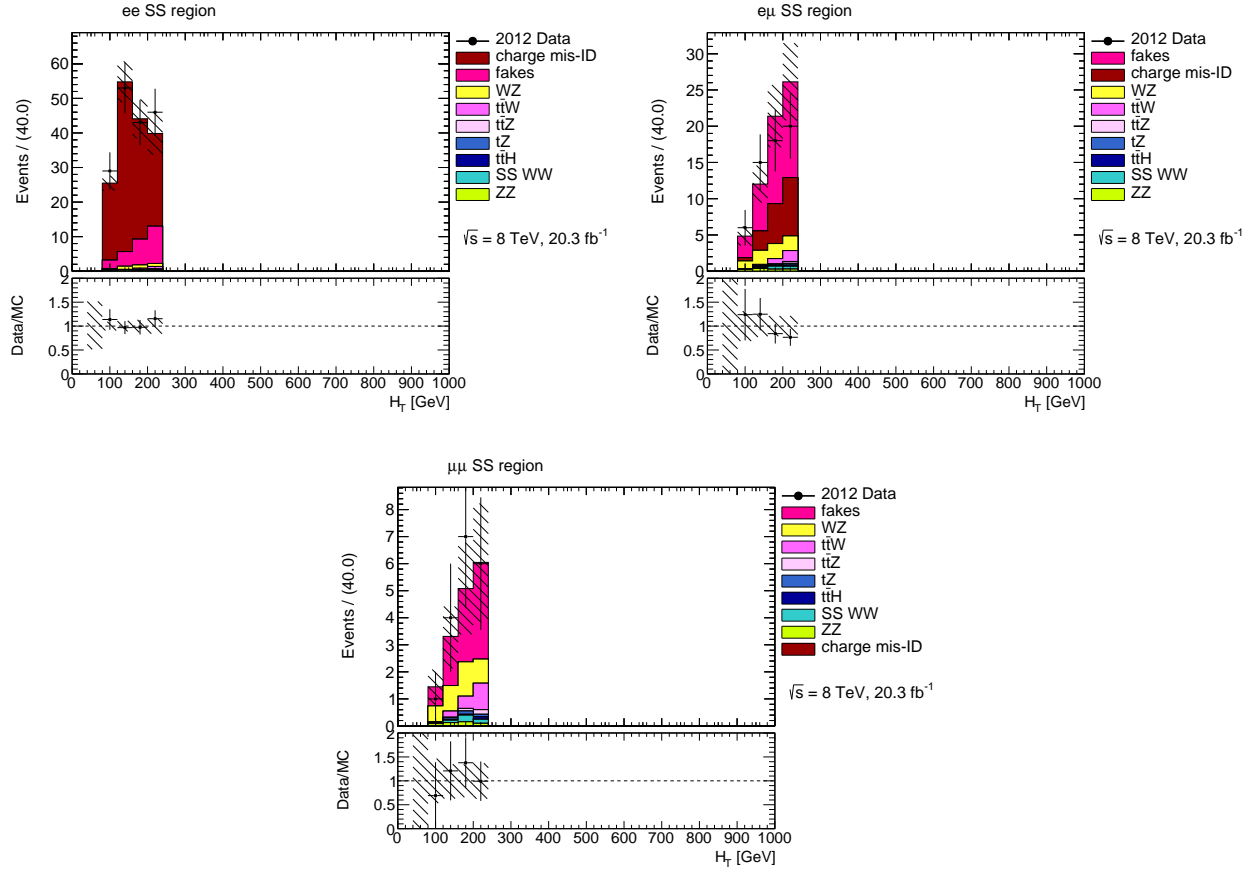


FIGURE 6.6: The distributions in H_T for two same-sign lepton final states: ee (top left), $e\mu$ (top right), and $\mu\mu$ (lower middle). The events are required to contain at least one b -tagged jet and $H_T < 240$ GeV. The rate of events from $t\bar{t}V$ is negligible in comparison to the other processes. The instrumental backgrounds are predicted using data-driven methods. The hatched areas include both statistical and systematic uncertainties.

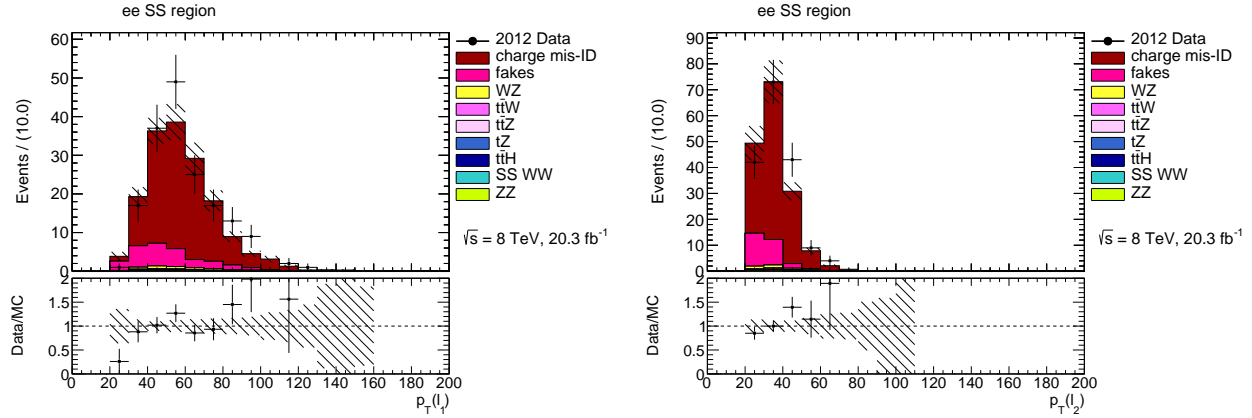


FIGURE 6.7: The distributions in p_T of the first and second leptons for two same-sign electron final states. The events are required to contain at least one b -tagged jet and $H_T < 240$ GeV. The rate of events from $t\bar{t}V$ is negligible in comparison to the other processes. The instrumental backgrounds are predicted using data-driven methods. The hatched areas include both statistical and systematic uncertainties.

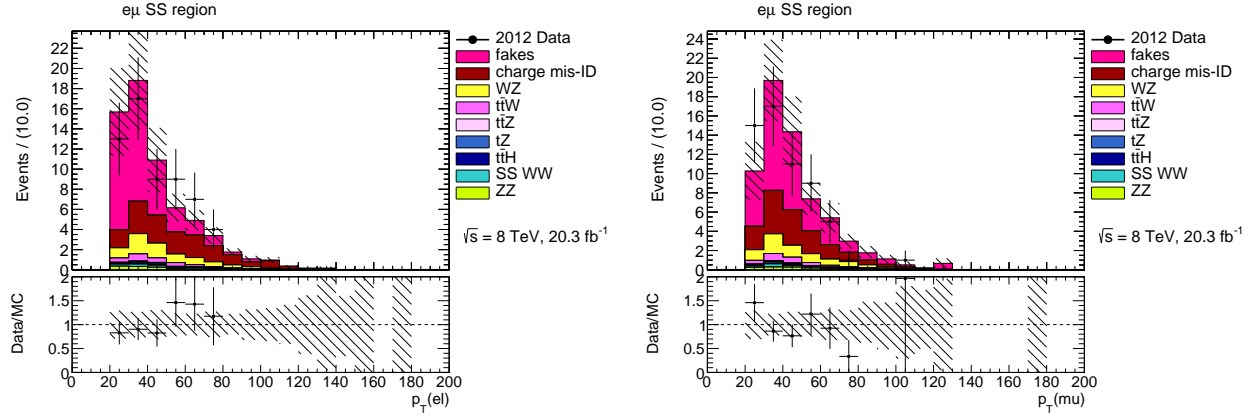


FIGURE 6.8: The distributions in p_T of the electrons and muons for same-sign $e\mu$ final states. The events are required to contain at least one b -tagged jet and $H_T < 240$ GeV. The rate of events from $t\bar{t}V$ is negligible in comparison to the other processes. The instrumental backgrounds are predicted using data-driven methods. The hatched areas include both statistical and systematic uncertainties.

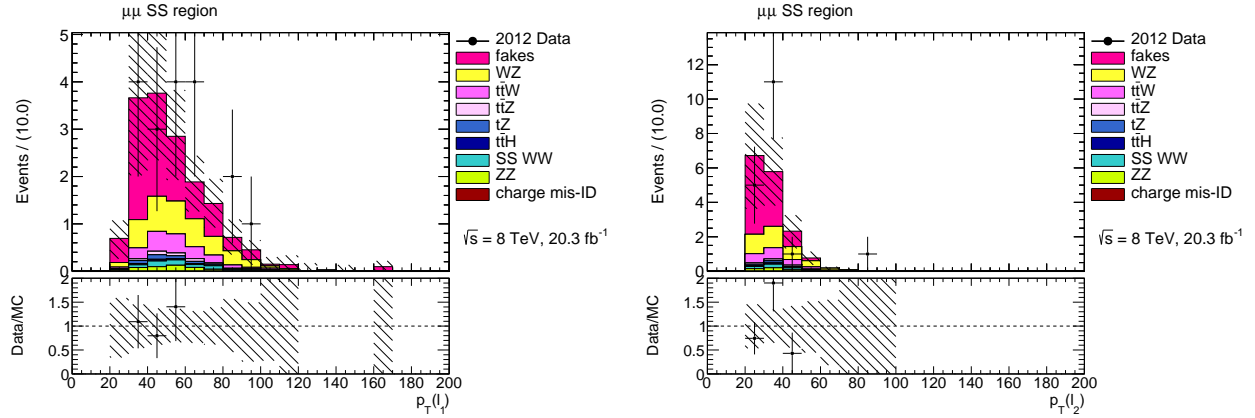


FIGURE 6.9: The distributions in p_T of the first and second leptons for two same-sign muon final states. The events are required to contain at least one b -tagged jet and $H_T < 240$ GeV. The rate of events from $t\bar{t}V$ is negligible in comparison to the other processes. The instrumental backgrounds are predicted using data-driven methods. The hatched areas include both statistical and systematic uncertainties.

6.2.5 Grand signal region

As described in section 6.2.1, the grand signal region is defined as follows:

- Require two same-sign identified leptons ($p_T > 25$ GeV).
- Veto events having more than two leptons with $p_T > 15$ GeV.
- The events are then separated into three channels: ee , $e\mu$, or $\mu\mu$.
- For ee or $\mu\mu$ channels, events with $m_{ll} < 15$ GeV are vetoed.
- Require $N_{b\text{-jets}} \geq 1$.
- $H_T > 240$ GeV.

Note this region covers the final signal region, but has no cuts on N_{jets} or E_T^{miss} .

The grand signal region allows us to understand the kinematic behavior of the signal and background processes, by looking at the following kinematic distributions:

- jet multiplicity (see Fig. 6.10),
- b -jet multiplicity (see Fig. 6.11),
- E_T^{miss} (see Fig. 6.12),
- H_T (see Fig. 6.13), and
- p_T of leptons (see Figs. 6.14, 6.15, and 6.16).

As shown in these figures, the signal $t\bar{t}V$ processes tend to have larger H_T , E_T^{miss} , and jet multiplicity than the background processes. In addition, fake leptons tend to have lower p_T than prompt leptons. Understanding these kinematic features of the signal and background processes are helpful for further extracting the signals from the backgrounds.

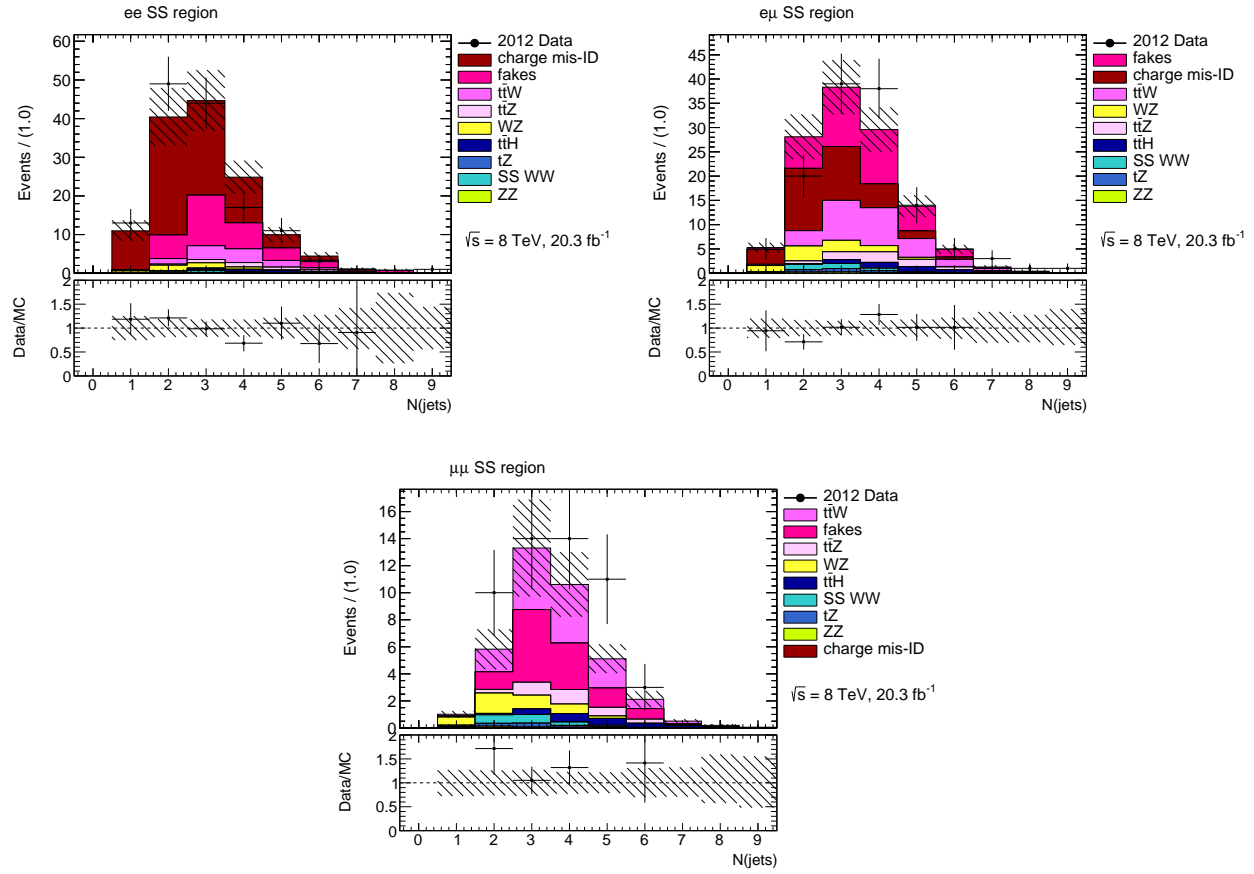


FIGURE 6.10: The distributions in jet multiplicity for two same-sign lepton final states: ee (top left), $e\mu$ (top right), and $\mu\mu$ (lower middle). The events are required to contain at least one b -tagged jet and $H_T > 240 \text{ GeV}$. The instrumental backgrounds are predicted using data-driven methods. The hatched areas include both statistical and systematic uncertainties.

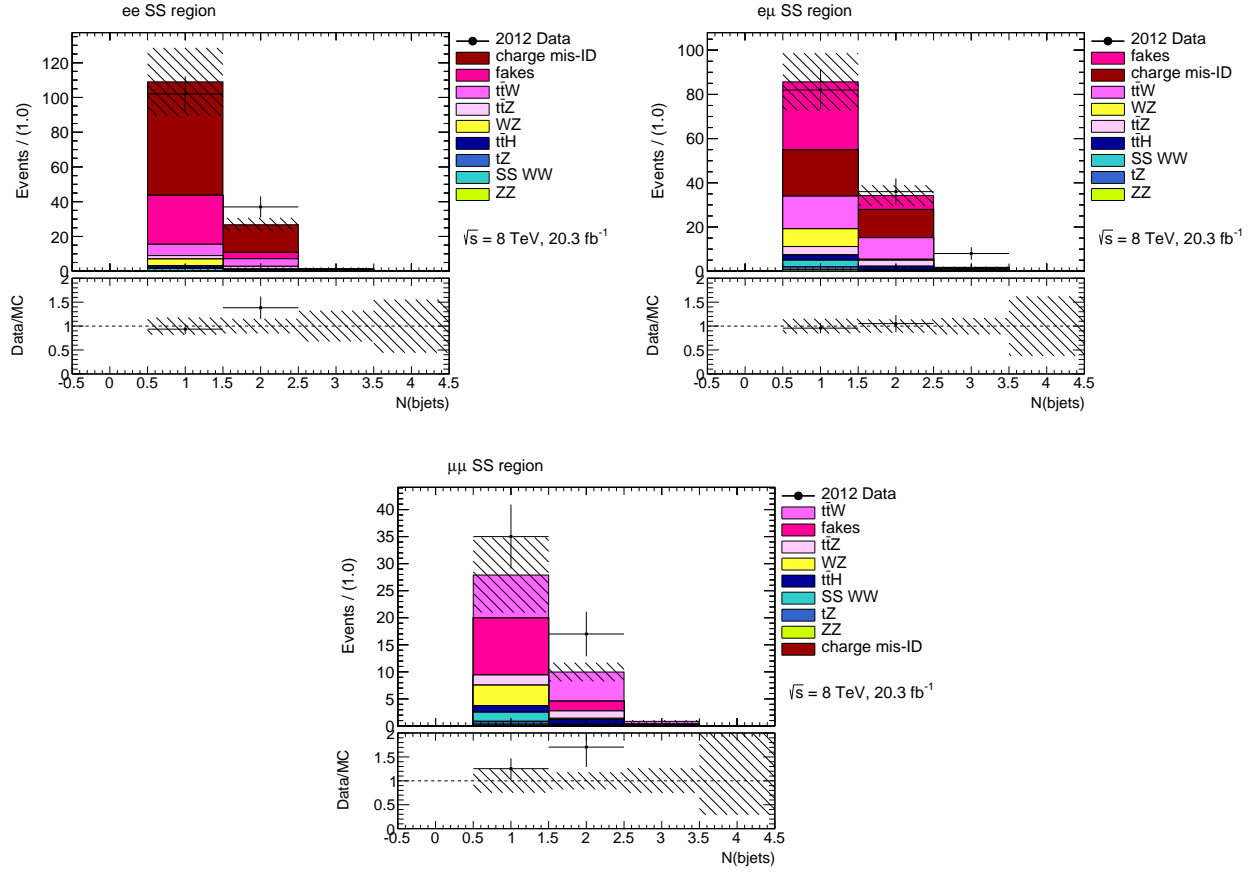


FIGURE 6.11: The distributions in b -tagged jet multiplicity for two same-sign lepton final states: ee (top left), $e\mu$ (top right), and $\mu\mu$ (lower middle). The events are required to contain at least one b -tagged jet and $H_T > 240 \text{ GeV}$. The instrumental backgrounds are predicted using data-driven methods. The hatched areas include both statistical and systematic uncertainties.

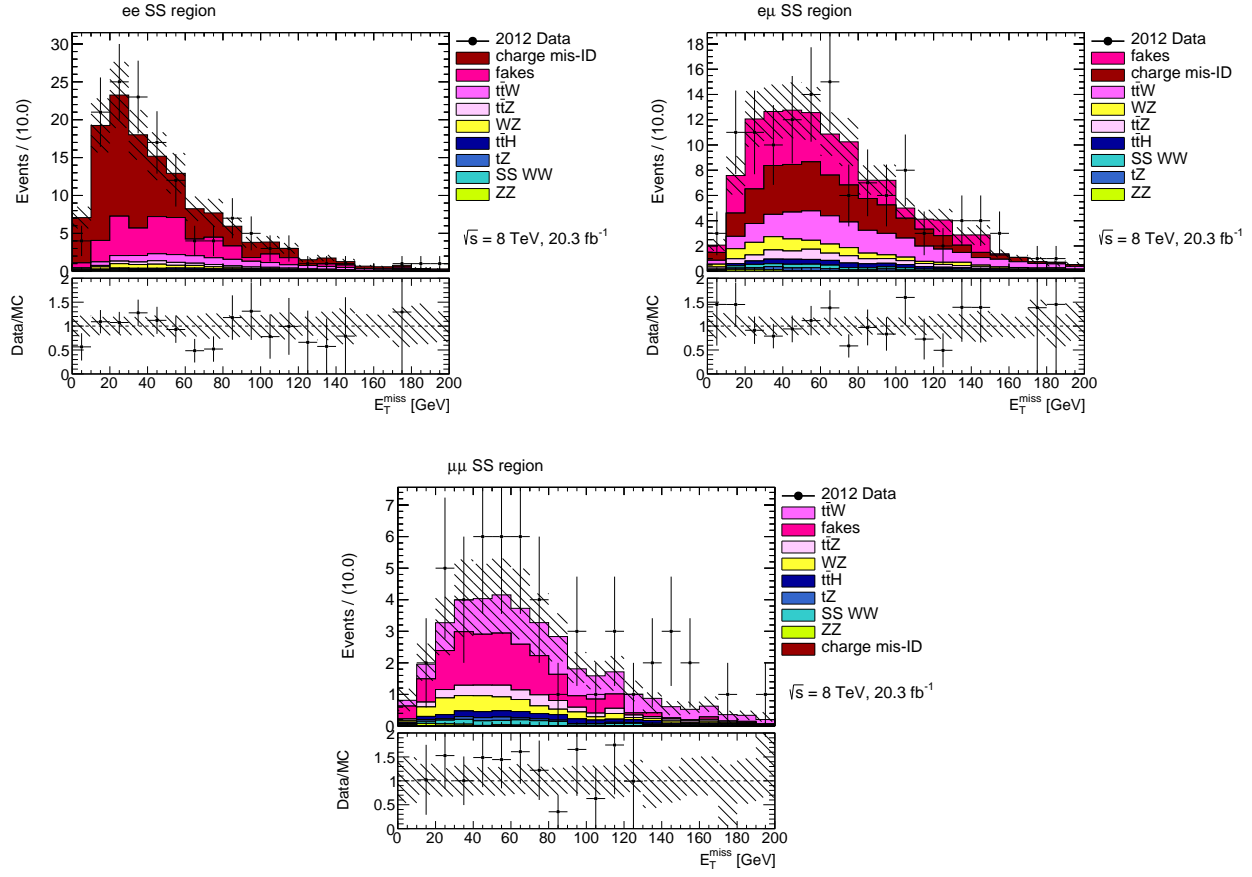


FIGURE 6.12: The distributions in missing transverse momentum for two same-sign lepton final states: ee (top left), $e\mu$ (top right), and $\mu\mu$ (lower middle). The events are required to contain at least one b -tagged jet and $H_T > 240$ GeV. The instrumental backgrounds are predicted using data-driven methods. The hatched areas include both statistical and systematic uncertainties.

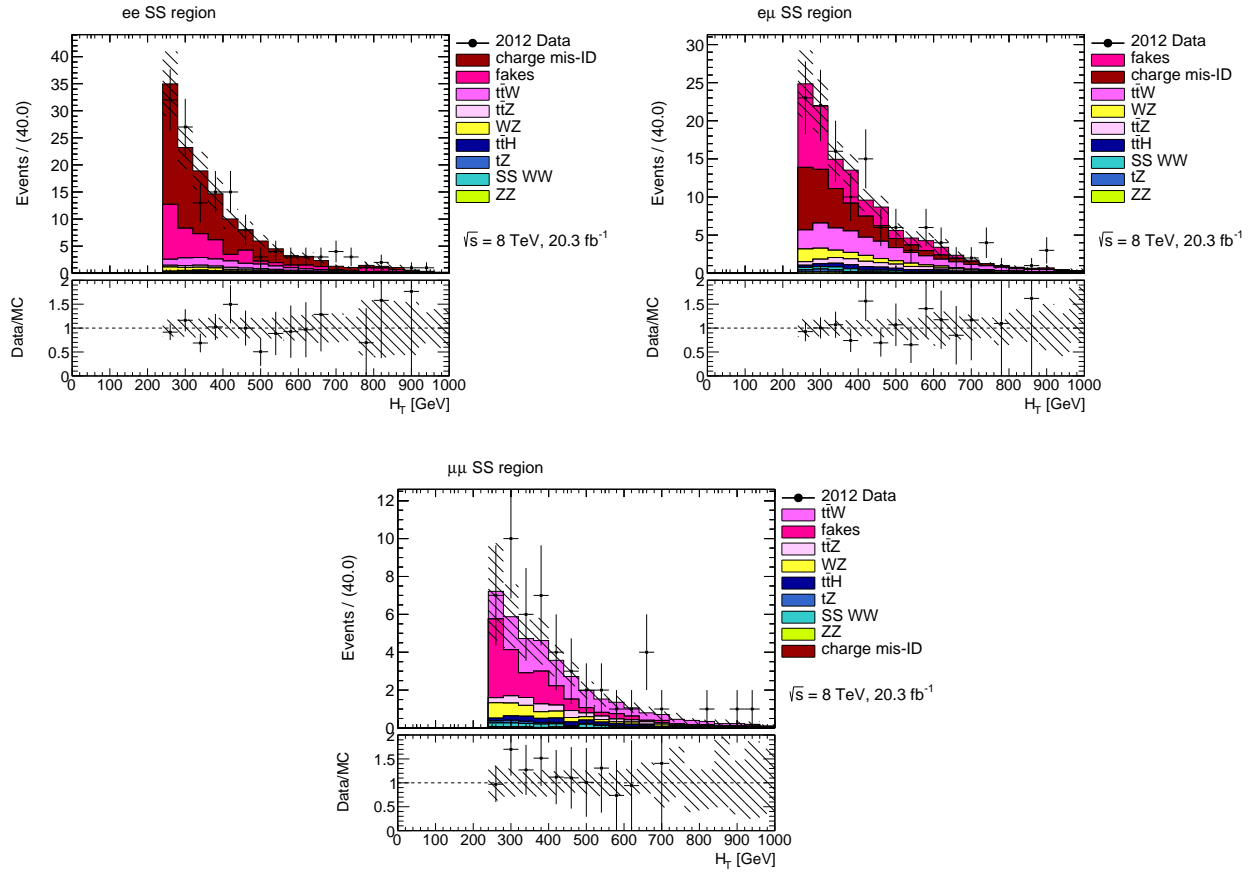


FIGURE 6.13: The distributions in H_T for two same-sign lepton final states: ee (top left), $e\mu$ (top right), and $\mu\mu$ (lower middle). The events are required to contain at least one b -tagged jet and $H_T > 240$ GeV. The instrumental backgrounds are predicted using data-driven methods. The hatched areas include both statistical and systematic uncertainties.

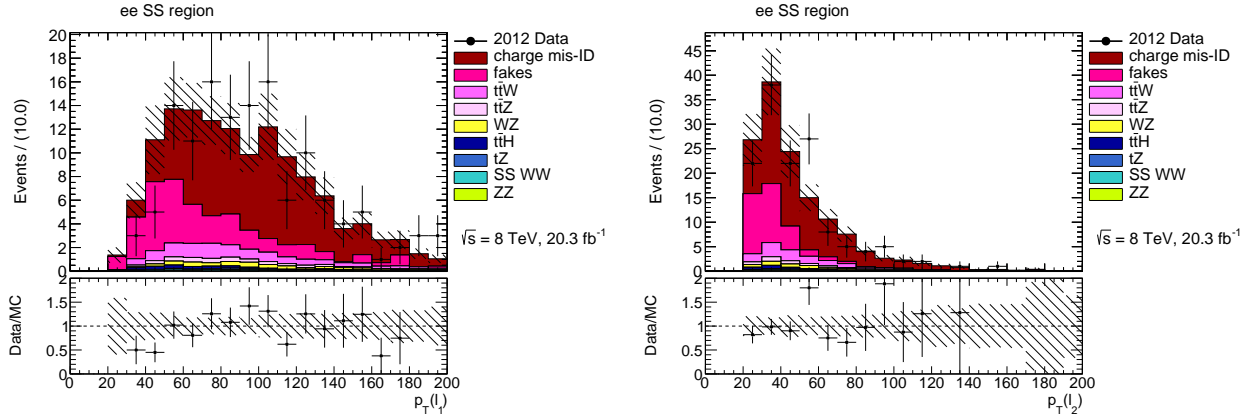


FIGURE 6.14: The distributions in p_T of the first and second leptons for two same-sign electron final states. The events are required to contain at least one b -tagged jet and $H_T > 240$ GeV. The instrumental backgrounds are predicted using data-driven methods. The hatched areas include both statistical and systematic uncertainties.

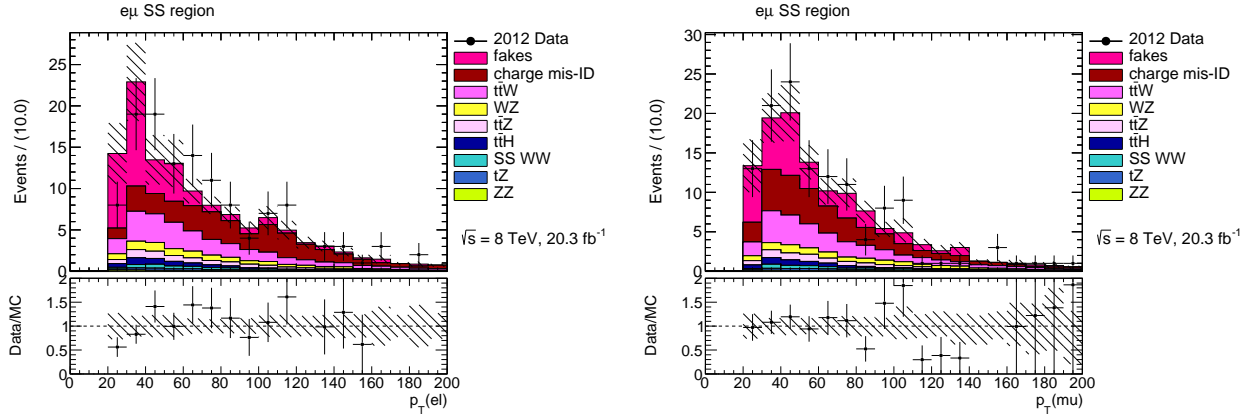


FIGURE 6.15: The distributions in p_T of the electrons and muons for same-sign $e\mu$ final states. The events are required to contain at least one b -tagged jet and $H_T > 240$ GeV. The instrumental backgrounds are predicted using data-driven methods. The hatched areas include both statistical and systematic uncertainties.

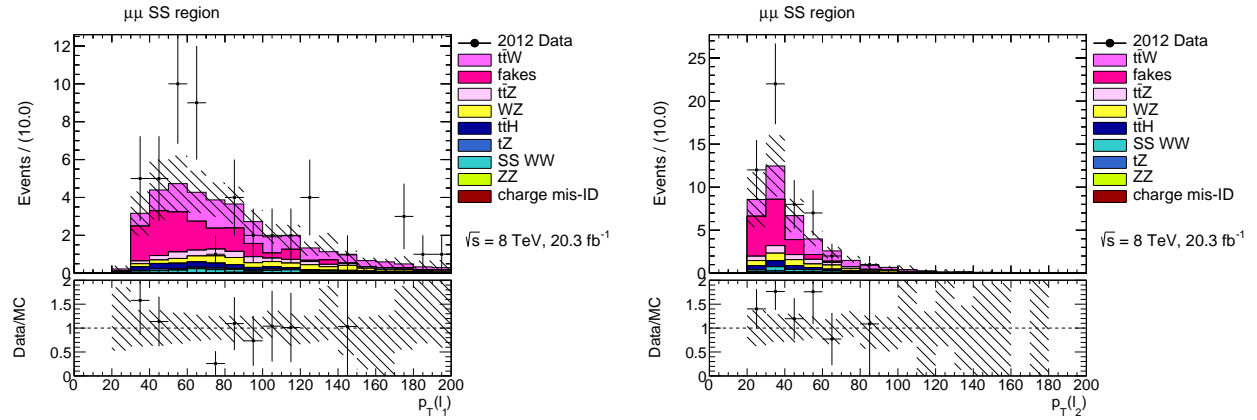


FIGURE 6.16: The distributions in p_T of the first and second leptons for two same-sign muon final states. The events are required to contain at least one b -tagged jet and $H_T > 240$ GeV. The instrumental backgrounds are predicted using data-driven methods. The hatched areas include both statistical and systematic uncertainties.

6.2.6 Further Analysis strategy

With the event selection and background estimation, the further analysis strategy of the 2SSL channel is to extract $t\bar{t}V$ events in a phase space of dilepton flavor (ee , $e\mu$, $\mu\mu$), jet (b -jet) multiplicity, and E_T^{miss} , because the signal processes ($t\bar{t}V$) and the background processes are naturally separated in this phase space. A likelihood function is constructed to fit the data to the expected distributions (templates) of the signal and background processes and simultaneously extract the signal cross sections. The Monte Carlo and data-driven templates that describe the signal and background processes are employed in the likelihood fit.

The following binning configurations are considered for constructing the phase space in the analysis:

- dilepton flavor axis: ee , $e\mu$, $\mu\mu$
- b -jet multiplicity ($N_{b\text{-jets}}$) axis: 2 $N_{b\text{-jets}}$ bins ($1, \geq 2$), or 1 $N_{b\text{-jets}}$ bin (≥ 2)
- jet multiplicity (N_{jets}) axis: 2 N_{jets} bins ($2\text{-}3, \geq 4$), or 4 N_{jets} bins ($2, 3, 4, \geq 5$)
- E_T^{miss} axis: 1 E_T^{miss} bin, or 2 E_T^{miss} bins ($40 < E_T^{\text{miss}} < 80 \text{ GeV}, \geq 80 \text{ GeV}$)

The ee , $e\mu$, and $\mu\mu$ channels have different physics compositions and signal-to-background ratios. Therefore, separating them results in greater signal sensitivity. The two options given for the shown $N_{b\text{-jets}}$ binning is for investigating the effect of using the $N_{b\text{-jets}} \geq 1$ events (split into two bins) versus that of using only the $N_{b\text{-jets}} \geq 2$ events. The N_{jets} and E_T^{miss} variables are used because the signal $t\bar{t}V$ processes tend to have larger N_{jets} and E_T^{miss} than the background processes, thus separating the signals from the backgrounds.

An optimization is performed by scanning the binning scenarios and analyzing the expected significance of the $t\bar{t}W$ signal while considering most of the statistical

and systematic uncertainties. Each binning scenario is a combination of the binning options for the b -jet multiplicity, jet multiplicity and E_T^{miss} axes. We do not optimize for $t\bar{t}Z$ here, as the 2SSL analysis is mainly sensitive to $t\bar{t}W$.

The results of the optimization using the $N_{b\text{-jets}} \geq 1$ events is shown in Table 6.3. The best expected significance is 3.1σ for $t\bar{t}W$, from the 2 E_T^{miss} bins, 4 N_{jets} bins, and 2 $N_{b\text{-jets}}$ bins scenario.

For the combination with the other analysis channels (2OSL, 3L, 4L), the $N_{b\text{-jets}} = 1$ events, which are used for the results in Table 6.3, cannot be used due to the overlap with a control region used by the 3L channel. Therefore, in considering the full combination of all channels, the best available scenario (using only the $N_{b\text{-jets}} \geq 2$ events) is achieved by using 2 E_T^{miss} bins and 4 N_{jets} bins, which gives an expected significance of 2.7σ . The results of the optimization using only the $N_{b\text{-jets}} \geq 2$ events is shown in Table 6.4.

An alternative approach is to use only one bin for each dilepton flavor, and apply tighter cuts on N_{jets} (requiring at least 2, 3, or 4 jets), $N_{b\text{-jets}}$ (requiring at least 2 b -tagged jets), and E_T^{miss} (requiring $E_T^{\text{miss}} > 40$ GeV or $E_T^{\text{miss}} > 80$ GeV). This approach is close to the strategy of a previous CMS $t\bar{t}V$ measurement [62].

The alternative approach is also studied and shown in Table 6.5. The expected significance of the best available scenario is 2.3σ , using the 2 b -tagged jet events and requiring $N_{\text{jets}} \geq 2$ and $E_T^{\text{miss}} > 80$ GeV. The performance of this approach is shown to be not as good as the baseline approach.

Overall, the best scenario is using 2 E_T^{miss} bins, 4 N_{jets} bins, and 2 $N_{b\text{-jets}}$ bins. However, we find using 2 N_{jets} bins instead of 4 N_{jets} bins gives almost identical expected significance and saves a large amount of computing time. In addition, the relatively small number of signal events in the ee channel does not allow us to have E_T^{miss} bins, noting we apply an additional requirement on dilepton mass in this channel. We also find the N_{jets} binning in the ee channel does not improve the

Table 6.3: Selected results of the optimization using the $N_{b\text{-jets}} \geq 1$ events. The significances are achieved using only the 2SSL events. The last row shows the final binning case where a single bin is used for the ee channel.

Bin configuration	ee	$e\mu$	$\mu\mu$	SS combined
1 E_T^{miss} bin, 2 N_{jets} bins	0.8σ	1.8σ	1.9σ	2.6σ
1 E_T^{miss} bin, 4 N_{jets} bins	0.7σ	1.8σ	2.0σ	2.7σ
2 E_T^{miss} bins, 2 N_{jets} bins	1.0σ	2.0σ	2.2σ	3.0σ
2 E_T^{miss} bins, 4 N_{jets} bins	0.9σ	2.2σ	2.2σ	3.1σ
2(1) E_T^{miss} bins, 2(1) N_{jets} bins for $e\mu, \mu\mu$ (for ee)	0.9σ	2.2σ	2.2σ	3.1σ

Table 6.4: Selected results of the optimization using the $N_{b\text{-jets}} \geq 2$ events (without the $N_{b\text{-jets}} = 1$ events). The significances are achieved using only the 2SSL events. The last row shows the final binning case where a single bin is used for the ee channel.

Bin configuration	ee	$e\mu$	$\mu\mu$	SS combined
1 E_T^{miss} bin, 2 N_{jets} bins	0.7σ	1.5σ	1.9σ	2.4σ
1 E_T^{miss} bin, 4 N_{jets} bins	0.5σ	1.5σ	1.9σ	2.4σ
2 E_T^{miss} bins, 2 N_{jets} bins	0.8σ	1.7σ	2.1σ	2.7σ
2 E_T^{miss} bins, 4 N_{jets} bins	0.7σ	1.9σ	2.0σ	2.7σ
2(1) E_T^{miss} bins, 2(1) N_{jets} bins for $e\mu, \mu\mu$ (for ee)	0.7σ	1.7σ	2.1σ	2.6σ

expected significance. The reason for this is the large backgrounds from charge mis-ID in this channel causes the signal-to-background ratio to be quite similar across the entire phase space. Thus, the final fit configuration is 2 E_T^{miss} bins, 2 N_{jets} bins, and 2 $N_{b\text{-jets}}$ bins for the $e\mu$ and $\mu\mu$ channels, and 2 $N_{b\text{-jets}}$ bins for the ee channel.

Table 6.5: Selected results of the optimization using the $N_{b\text{-jets}} \geq 2$ events and the alternative (tighter cuts) approach. The significances are achieved using only the 2SSL events.

Single bin definition	ee	$e\mu$	$\mu\mu$	SS combined
$E_T^{\text{miss}} > 40 \text{ GeV}, N_{\text{jets}} \geq 2$	0.7σ	1.2σ	1.8σ	2.0σ
$E_T^{\text{miss}} > 40 \text{ GeV}, N_{\text{jets}} \geq 3$	0.8σ	1.2σ	1.8σ	2.0σ
$E_T^{\text{miss}} > 40 \text{ GeV}, N_{\text{jets}} \geq 4$	0.7σ	1.4σ	1.5σ	2.1σ
$E_T^{\text{miss}} > 80 \text{ GeV}, N_{\text{jets}} \geq 2$	0.1σ	1.4σ	1.9σ	2.3σ
$E_T^{\text{miss}} > 80 \text{ GeV}, N_{\text{jets}} \geq 3$	0.1σ	1.4σ	1.8σ	2.2σ
$E_T^{\text{miss}} > 80 \text{ GeV}, N_{\text{jets}} \geq 4$	0.2σ	1.3σ	1.4σ	2.0σ

As previously mentioned, in the combination procedure, the $N_{b\text{-jets}} = 1$ events are unavailable. So for the combination, the final fit configuration for the 2SSL channel is 2 E_T^{miss} bins and 2 N_{jets} bins for the $e\mu$ and $\mu\mu$ channels, and one bin for the ee channel (which amounts to a simple event count for ee with E_T^{miss} and N_{jets} cuts). For this configuration, the expected and observed contributions in each of the three dilepton flavour channels are shown in Figure 6.17.

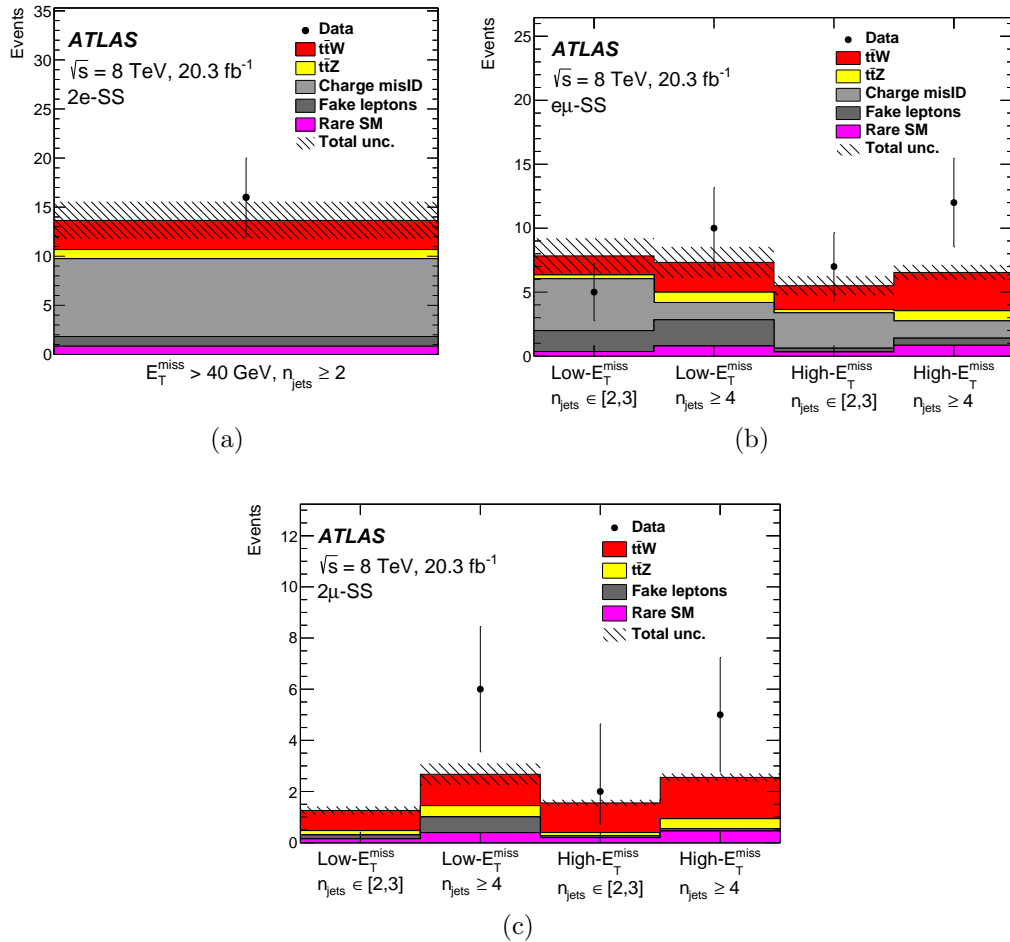


FIGURE 6.17: Expected and observed contributions in the (a) ee , (b) $e\mu$ and (c) $\mu\mu$ channels of the 2SSL signal regions with the binning used in the final likelihood fit. The distributions are shown before the fit. “Rare SM” contains small background contributions mainly consisting of the $t\bar{t}H$ and WZ processes. The instrumental backgrounds are predicted using data-driven methods. The hatched areas include both statistical and systematic uncertainties.

6.3 Two Opposite-sign Lepton Analysis

We now briefly discuss the other three channels used for the combined $t\bar{t}V$ result for completeness, noting that the author did not contribute significantly to these individual channels.

The 2OSL analysis channel requires events to have two leptons with opposite electric charge and $p_T > 15$ GeV. Additionally, events are required to have at least three jets. The average ΔR between two jets, among all possible jet pairs in an event, is required to be above 0.75, in order to remove a phase space where the $Z+jets$ simulation does not provide a good description.

Furthermore, two orthogonal preselection requirements are used, referred to as the 2ℓ - Z region and the 2ℓ -no Z region. The 2ℓ - Z region contains events with a Z candidate, which is a pair of same-flavor leptons, with $|m_{\ell\ell} - m_Z| < 10$ GeV (a 20 GeV mass window around the Z mass of 91 GeV). The 2ℓ - Z region targets the $t\bar{t}Z$ process, where the associated Z boson decays into two same-flavor opposite-sign leptons, and both the W bosons from $t\bar{t}$ decay hadronically. The contribution from the $t\bar{t}W$ process is negligible. In this region, the main background is $Z+jets$ production. On the other hand, the 2ℓ -no Z region contains events with a same-flavor or different-flavor lepton pair. For the same-flavor events, $|m_{\ell\ell} - m_Z| > 10$ GeV, $m_{\ell\ell} > 15$ GeV, and $E_T^{\text{miss}} > 15$ GeV are required, in order to reject events from Z boson or low-mass resonance production. For the different-flavor events, H_T , the scalar sum of the p_T of all leptons and jets in the event, is required to be above 130 GeV, which increases the signal-to-background ratio. The 2ℓ -no Z region targets both the $t\bar{t}Z$ and $t\bar{t}W$ processes, where the associated Z or W bosons decay hadronically, and both the W bosons from $t\bar{t}$ decay leptonically. Additionally, the $t\bar{t}W$ process can contribute to the 2ℓ -no Z region, when the associated W boson and one W boson from the top quark pairs decay leptonically. In this region, the main background is

$t\bar{t}$ production.

The 2OSL background estimates are important for extracting the signals, and are determined from Monte Carlo simulation. The simulated $t\bar{t}$ events are reweighted to account for differences between data and simulation in the top quark p_{T} distribution and the p_{T} distribution of the $t\bar{t}$ system, as documented in a previous $t\bar{t}$ differential cross section measurement [63]. In addition, the simulated $Z+\text{jets}$ events are reweighted to account for differences between the observed and simulated Z boson p_{T} distributions, as documented in a previous $Z+\text{jets}$ cross section measurement [64], and the $Z+\text{heavy flavor jets}$ component is adjusted to achieve better data to simulation agreement in a control region dominated by $Z+\text{heavy flavor jets}$ production. These adjustments to the simulated $t\bar{t}$ and $Z+\text{jets}$ events improve the modeling of these backgrounds.

$W+\text{jets}$, $t\bar{t}$ production (with a single lepton in the final state), and certain other processes can contribute to the 2OSL regions, when the event additionally contains a mis-identified or non-prompt lepton. However, these fake lepton backgrounds are found to be small, compared with the total backgrounds in the 2OSL regions. The fake lepton backgrounds are estimated directly from Monte Carlo simulation, and cross-checked with a data-driven method based on a two same-sign lepton selection.

For both the $2\ell-Z$ region and the $2\ell-\text{no}Z$ region, we further define signal regions and control regions by jet and b -tagged jet multiplicity. The definitions of these regions are as follows.

- $2\ell-Z-3\text{j}$ control region: $2\ell-Z$ events with exactly three jets, exactly two of which are b -tagged.
- $2\ell-Z-4\text{j}$ control region: $2\ell-Z$ events with exactly four jets, exactly two of which are b -tagged.
- $2\ell-Z-5\text{j}$ signal region: $2\ell-Z$ events with at least five jets, exactly two of which

are b -tagged.

- 2ℓ -no Z -3j control region: 2ℓ -no Z events with exactly three jets, one or two of which are b -tagged.
- 2ℓ -no Z -4j signal region: 2ℓ -no Z events with exactly four jets, one or two of which are b -tagged.
- 2ℓ -no Z -5j signal region: 2ℓ -no Z events with at least five jets, one or two of which are b -tagged.

For the signal regions, 2ℓ - Z -5j, 2ℓ -no Z -4j, and 2ℓ -no Z -5j, a neural network (NN) discriminant is separately produced by the NeuroBayes package [65], and used for the final likelihood fit. The NN algorithm takes several variables as the input, and produces a single discriminant as the output, which is able to separate the $t\bar{t}V$ signals from the backgrounds. For each signal region, seven variables are separately chosen as the neural network inputs, based on the rankings provided by the NeuroBayes package, which considers the statistical separation power and the correlation of the variables. All variables used for the NN algorithm are required to show good data to simulation agreement in the given control regions. The NN discriminant distributions in the 2ℓ -no Z -4j, 2ℓ -no Z -5j, and 2ℓ - Z -5j signal regions are shown in Figure 6.18.

For the control regions, a simple event count discriminant is used in the 2ℓ -no Z -3j region, while the scalar sum of the p_T of hadronic jets (H_T^{had}) is used for the 2ℓ - Z -3j and 2ℓ - Z -4j regions. The control regions are dominated by the $t\bar{t}$ and $Z+jets$ backgrounds, with limited sensitivities for the $t\bar{t}V$ signals. These regions are also included in the final likelihood fit, and strongly constrain the normalization uncertainties of the $t\bar{t}$ and $Z+jets$ backgrounds. This increases the signal significance in the final result. The discriminant distributions in the 2ℓ -no Z -3j, 2ℓ - Z -3j, and 2ℓ - Z -4j control regions are shown in Figure 6.19.

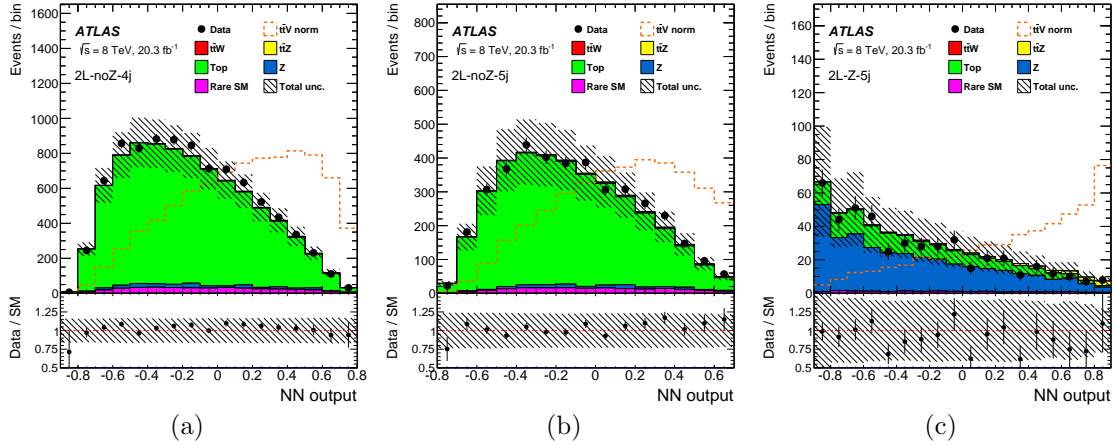


FIGURE 6.18: The NN discriminant distributions in the 2ℓ -no Z -4j (a), 2ℓ -no Z -5j (b), 2ℓ - Z -5j (c) signal regions. The dashed lines are the $t\bar{t}V$ distributions normalized to the background yields. The distributions are shown before the final likelihood fit. “Rare SM” contains the diboson, single top, tZ , $t\bar{t}H$ processes and the fake lepton background. The hatched areas include both statistical and systematic uncertainties.

6.4 Three Lepton Analysis

The 3L analysis channel requires events to have three leptons (electrons and muons in any combination) with $p_T > 15$ GeV. Furthermore, two orthogonal preselection requirements are used, referred to as the 3ℓ - Z region and the 3ℓ -no Z region. The 3ℓ - Z region requires a Z boson candidate, which is a pair of same-flavor opposite-sign leptons, with $m_{\ell\ell} - m_Z < 10$ GeV (a 20 GeV mass window around the Z mass). The 3ℓ - Z region targets the $t\bar{t}Z$ process, where the Z boson decays into two same-flavor opposite-sign leptons. In this region, the main background is WZ production. On the other hand, the 3ℓ -no Z region contains the remaining 3L events, except those in which the three leptons have the same charge. The 3ℓ -no Z region targets the $t\bar{t}W$ process, where the total lepton charge cannot be $+3e$ or $-3e$. In this region, the main background is the fake lepton background. In both the 3ℓ - Z region and the 3ℓ -no Z region, we further define multiple signal regions and control regions.

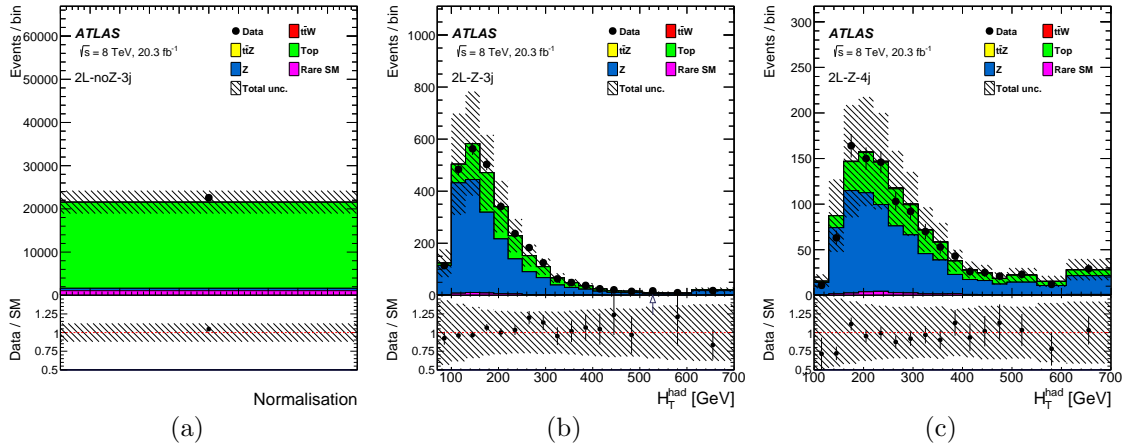


FIGURE 6.19: The discriminant distributions in the 2ℓ -no Z -3j (a), 2ℓ - Z -3j (b), 2ℓ - Z -4j (c) control regions. Event count is used in the 2ℓ -no Z -3j region, while the scalar sum of the p_T of hadronic jets (H_T^{had}) is used for the 2ℓ - Z -3j and 2ℓ - Z -4j regions. The distributions are shown before the final likelihood fit. “Rare SM” contains the diboson, single top, tZ , $t\bar{t}H$ processes and the fake lepton background. The hatched areas include both statistical and systematic uncertainties.

Four signal regions are defined in the 3L analysis channel as follows. These four signal regions are found to have quite different signal-to-background ratios and systematic uncertainties.

- 3ℓ - Z -1b4j: 3ℓ - Z events with at least four jets, exactly one of which is b -tagged.
- 3ℓ - Z -2b3j: 3ℓ - Z events with exactly three jets, at least two of which are b -tagged.
- 3ℓ - Z -2b4j: 3ℓ - Z events with at least four jets, at least two of which are b -tagged.
- 3ℓ -no Z -2b: 3ℓ -no Z events with at least two b -tagged jets.

In addition, if the third lepton (recalling the leptons are ranked by p_T) is an electron, the p_T requirement on this lepton is raised to 20 GeV for the 3ℓ - Z -1b4j, 3ℓ - Z -2b3j, and 3ℓ - Z -2b4j regions, or 25 GeV for the 3ℓ -no Z -2b region. This requirement

is designed to reduce the fake electron background, where the mis-identified or non-prompt electron tends to have relatively low energy. The lepton p_T requirements are optimized for each signal region, by maximizing expected significances.

The kinematics of the WZ background is estimated using Monte Carlo simulation. To further constrain its normalization, a control region, labelled 3ℓ - Z - $0b3j$, is defined. This region requires 3ℓ - Z events with exactly three jets and exactly zero b -tagged jet, where WZ production contributes most of the events. In the final likelihood fit, the 3ℓ - Z - $0b3j$ control region is included, and the normalization of the WZ background is treated as a floating parameter. The correction on the WZ background normalization with respect to the SM prediction is obtained from the fit, and found to be 0.98 ± 0.20 . In addition, another control region, 3ℓ - Z - $1b$, is defined to validate the modeling of the WZ background with heavy flavor jets. This region requires 3ℓ - Z events with one to three jets, exactly one of which is b -tagged. The distribution of the third lepton p_T in the 3ℓ - Z - $1b$ region is shown in Figure 6.20. The observed and expected distributions are found to agree well.

The fake lepton background is estimated using the so-call matrix method, a well-established data-driven method [66]. Similarly to the fake factor method, the matrix method utilizes loose leptons, for which the lepton isolation and identification criteria are relaxed. The real (fake) lepton efficiencies are defined as the probabilities of passing tight lepton criteria, for real (fake) leptons passing loose lepton criteria. These efficiencies are measured in a control region with two same-sign leptons and exactly one b -tagged jet. Finally, matrices are constructed using the numbers of events with loose leptons, as well as the corresponding efficiencies for real and fake leptons. It can be shown that the number of fake lepton events in the analysis region (with only tight leptons) can be determined from these matrices. To validate the fake lepton background estimation, another control region, labelled 3ℓ - noZ - $1b$, is defined. This region requires 3ℓ - noZ events with exactly one b -tagged jet. The distribution of

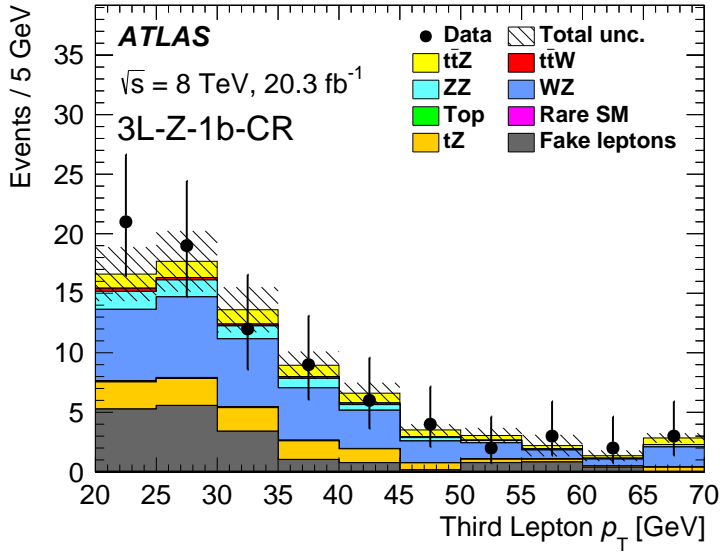


FIGURE 6.20: The distribution of the third lepton p_T in the 3ℓ - Z - $1b$ region. The distribution is shown before the final likelihood fit. The last bin includes the overflow. “Rare SM” contains small background contributions mainly consisting of the $H \rightarrow ZZ$ and triboson processes. The hatched areas include both statistical and systematic uncertainties.

missing transverse momentum in the 3ℓ -no Z - $1b$ region is shown in Figure 6.21. The agreement between data and expectation is also found to be good.

For the final likelihood fit, the discriminant provided by the 3L analysis channel is the event counts of the four signal regions (3ℓ - Z - $1b4j$, 3ℓ - Z - $2b3j$, 3ℓ - Z - $2b4j$ and 3ℓ -no Z - $2b$), as well as the 3ℓ - Z - $0b3j$ control region. The event yields of different lepton flavor combinations in the 3ℓ - Z signal regions are shown in Figure 6.22. (Note these lepton flavor combinations are not used in the final likelihood fit.)

6.5 Four Lepton Analysis

The 4L analysis channel requires events to have four leptons with $p_T > 7$ GeV. This channel targets the $t\bar{t}Z$ process, where the associated Z boson and the two W bosons (from the top quark pair decays) all decay leptonically. The main background for

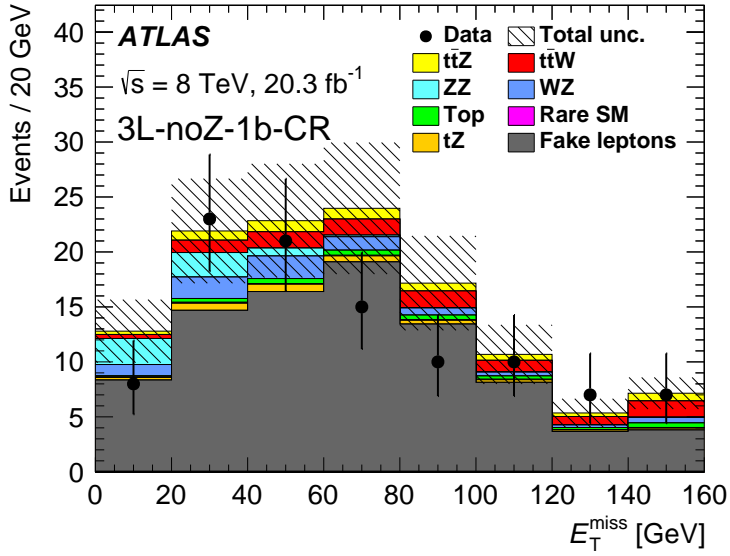


FIGURE 6.21: The distribution of missing transverse momentum in the 3ℓ -no Z -1 b region. The distribution is shown before the final likelihood fit. The last bin includes the overflow. “Rare SM” contains small background contributions mainly consisting of the $H \rightarrow ZZ$ and triboson processes. The hatched areas include both statistical and systematic uncertainties.

the 4L channel is ZZ production.

With the four leptons, this analysis first forms a best Z candidate, by looking for an opposite-sign same-flavor lepton pair. In the case no such lepton pair is found, the event is removed. If more than one opposite-sign same-flavor lepton pair are found, the one with the invariant mass closest to the Z boson mass is chosen. This lepton pair is referred to as $Z1$ ($\ell 1, \ell 2$). The remaining two leptons are referred to as $Z2$ ($\ell 3, \ell 4$). $Z2$ is required to have opposite electric charge, because the total electric charge of the top quark pair in $t\bar{t}Z$ events is zero.

Signal regions are defined according to the relative flavor of $\ell 3$ and $\ell 4$, which can be different flavor (DF) or same flavor (SF), as well as the b -tagged jet multiplicity, which can be zero (0 b), one (1 b), or at least two (2 b). There are five signal regions defined: 4 ℓ -DF-0 b , 4 ℓ -DF-1 b , 4 ℓ -DF-2 b , 4 ℓ -SF-1 b , 4 ℓ -SF-2 b . The 4 ℓ -SF-0 b events

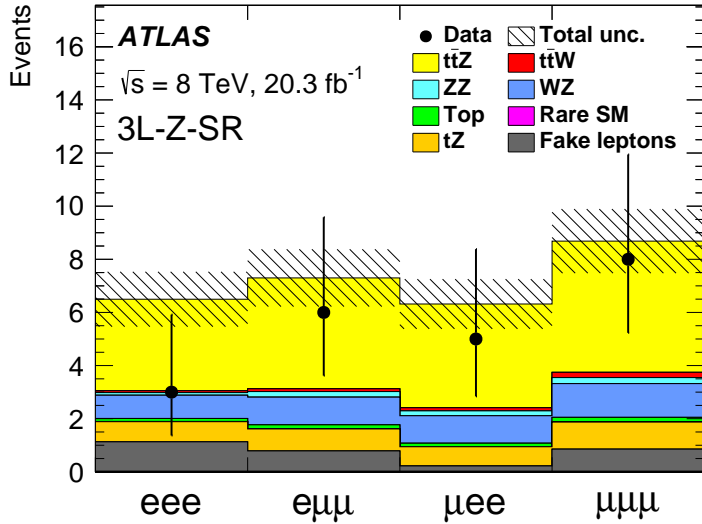


FIGURE 6.22: The event yields of different lepton flavor combinations in the 3ℓ - Z signal regions. The distribution is shown before the final likelihood fit. “Rare SM” contains small background contributions mainly consisting of the $H \rightarrow ZZ$ and triboson processes. The hatched areas include both statistical and systematic uncertainties.

are not used to define a signal region, because these events are dominated by ZZ production (most of the ZZ events are produced without heavy flavor jets).

Furthermore, additional requirements are applied to each signal region. These requirements are optimized by minimizing the expected statistical uncertainties on the $t\bar{t}Z$ cross section measurements. The signal region definitions are listed below:

- 4ℓ -DF-0b:

$Z2$ is opposite-sign and different-flavor ($e^\pm\mu^\mp$), exactly zero b -tagged jet, at least two jets, p_{T4} (the transverse momentum of $\ell4$) > 10 GeV, p_{T34} (the scalar sum of the transverse momenta of $\ell3$ and $\ell4$) > 45 GeV.

- 4ℓ -DF-1b:

$Z2$ is opposite-sign and different-flavor ($e^\pm\mu^\mp$), exactly one b -tagged jet, $p_{T4} >$

7 GeV, $p_{T34} > 35$ GeV.

- 4 ℓ -DF-2b:

$Z2$ is opposite-sign and different-flavor ($e^\pm\mu^\mp$), at least two b -tagged jets, $p_{T4} > 7$ GeV.

- 4 ℓ -SF-1b:

$Z2$ is opposite-sign and same-flavor ($e^\pm e^\mp$ or $\mu^\pm\mu^\mp$), exactly one b -tagged jet, $p_{T4} > 7$ GeV, $p_{T34} > 25$ GeV. In addition, if $|m_{l3l4} - m_Z| > 10$ GeV, it is required that $E_T^{\text{miss}} > 40$ GeV. Conversely if $|m_{l3l4} - m_Z| < 10$ GeV, it is required that $E_T^{\text{miss}} > 80$ GeV.

- 4 ℓ -SF-2b:

$Z2$ is opposite-sign and same-flavor ($e^\pm e^\mp$ or $\mu^\pm\mu^\mp$), at least two b -tagged jets, $p_{T4} > 7$ GeV. In addition, if $|m_{l3l4} - m_Z| < 10$ GeV, it is required that $E_T^{\text{miss}} > 40$ GeV.

The requirements on $|m_{l3l4} - m_Z|$ and E_T^{miss} are made to reduce ZZ production, because the ZZ events tend to have m_{l3l4} close to the Z boson mass and have low E_T^{miss} . The requirements on p_{T4} and p_{T34} are intended to reject the fake lepton background, because the fake leptons tend to have low energy. In addition, for all signal regions, if the invariant mass of any opposite-sign lepton pair is less than 10 GeV, the event is removed.

Similarly to the WZ background estimation in the 3L channel, the kinematics of the ZZ background is estimated using Monte Carlo simulation, and a control region, labelled 4 ℓ - ZZ , is defined to constrain the ZZ background normalization. This region requires events to have two opposite-sign same-flavor lepton pairs with $|m_{ll} - m_Z| < 10$ GeV, as well as $E_T^{\text{miss}} < 50$ GeV, where the events are mostly from ZZ

production. The $4\ell-ZZ$ control region is also included in the final likelihood fit, with the ZZ background normalization floated. The correction on the ZZ background normalization with respect to the SM prediction is found to be 1.16 ± 0.12 from the fit. In addition, the distributions of the jet multiplicity and b -tagged jet multiplicity in the $4\ell-ZZ$ region are shown in Figure 6.23. The observed and expected distributions agree well.

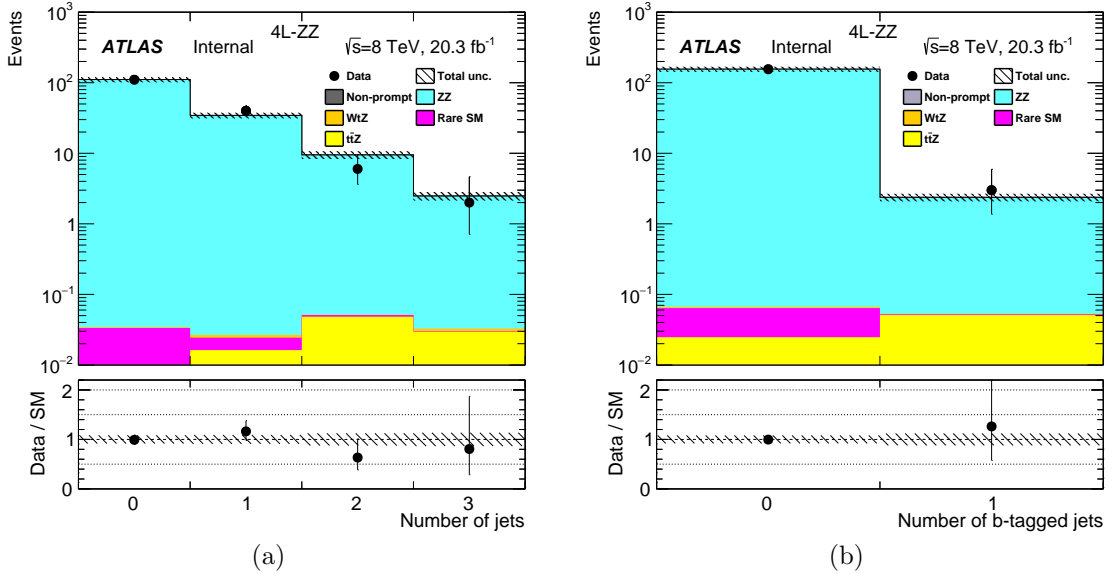


FIGURE 6.23: The distributions of the jet multiplicity (a) and b -tagged jet multiplicity (b) in the $4\ell-ZZ$ region. The distributions are shown before the final likelihood fit. “Rare SM” contains small background contributions mainly consisting of the $t\bar{t}H$ and tZ processes. The hatched areas include both statistical and systematic uncertainties.

The backgrounds with at least one mis-identified or non-prompt lepton are estimated with Monte Carlo simulation. However, the normalization of the fake lepton estimates need to be multiplied by an appropriate constant factor, depending on the fake lepton flavor and physics process. There are four such correction factors defined:

- $c_e^{t\bar{t}}$: applied to $t\bar{t}$ -like events with a fake electron
- $c_\mu^{t\bar{t}}$: applied to $t\bar{t}$ -like events with a fake muon

- c_e^Z : applied to Z -like events with a fake electron
- c_μ^Z : applied to Z -like events with a fake muon

The correction factors are derived from a Z +fake lepton control region and a $t\bar{t}$ +fake lepton control region, where the fake lepton contributions are enhanced. Both the control regions require events with three leptons. For the Z +fake lepton control region, $E_T^{\text{miss}} < 30$ GeV and an opposite-sign same-flavor lepton pair are required. In addition, the third lepton (the fake lepton candidate) together with the E_T^{miss} is required to satisfy $m_T < 35$ GeV, where $m_T = \sqrt{2p_T^\ell E_T^{\text{miss}} - 2\mathbf{p}_T^\ell \cdot \mathbf{p}_T^{\text{miss}}}$ is the transverse mass. This requirement reduces the contamination of real leptons from W decays. For the $t\bar{t}$ +fake lepton control region, at least one jet with $p_T > 30$ GeV and an opposite-sign lepton pair are required. In addition, events with an opposite-sign same-flavor lepton pair are removed. The events in the $t\bar{t}$ +fake lepton control region must have two same-sign leptons and the one with lower p_T is used as the fake lepton candidate. By optimizing the agreement between observed data and expected backgrounds in the control regions, the four correction factors are determined:

- $c_e^{t\bar{t}}$: 1.23 ± 0.13
- $c_\mu^{t\bar{t}}$: 1.25 ± 0.09
- c_e^Z : 1.35 ± 0.05
- c_μ^Z : 1.61 ± 0.05

Furthermore, the backgrounds with at least two mis-identified or non-prompt leptons are first evaluated from simulation with relaxed requirements and then extrapolated into the signal regions. They are found to be very small, compared with the backgrounds with only one fake lepton.

Similarly to the 3L analysis, for the final likelihood fit, the discriminant in the 4L analysis is the event counts in the five signal regions ($4\ell\text{-DF-0}b$, $4\ell\text{-DF-1}b$, $4\ell\text{-DF-2}b$, $4\ell\text{-SF-1}b$, $4\ell\text{-SF-2}b$), as well as the $4\ell\text{-}ZZ$ control region. The distributions of the jet multiplicity, b -tagged jet multiplicity, $Z1$ invariant mass, and $Z2$ invariant mass in the 4L signal regions are shown in Figure 6.24. (Note these distributions are not used in the final likelihood fit.)

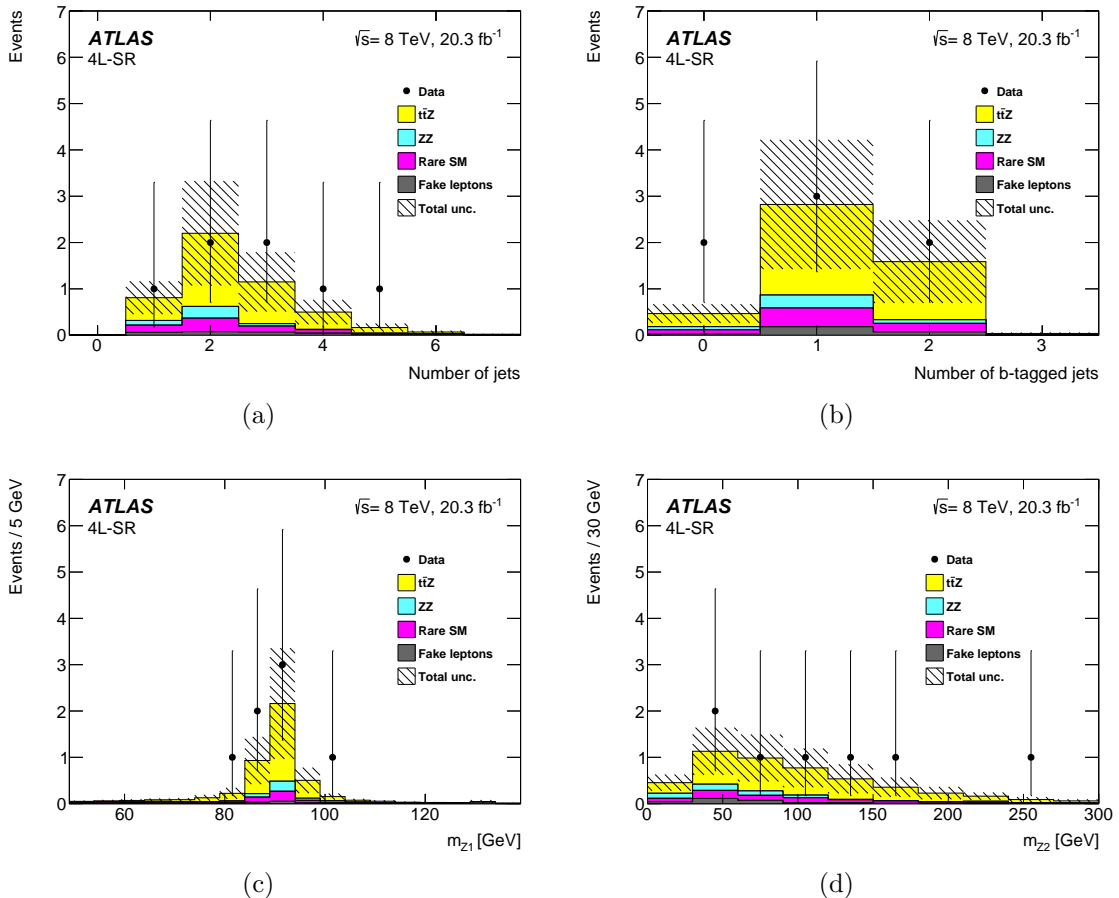


FIGURE 6.24: The distributions of the jet multiplicity (a), b -tagged jet multiplicity (b), $Z1$ invariant mass (c), and $Z2$ invariant mass (d) in the 4L signal regions. The distributions are shown before the final likelihood fit. “Rare SM” contains small background contributions mainly consisting of the $t\bar{t}H$ and tZ processes. The hatched areas include both statistical and systematic uncertainties.

Systematic Uncertainties

The expected distributions for signal and background processes contain a number of sources of systematic uncertainties. For each systematic uncertainty, there are generally two types of effects: those related to event rates, and those associated with kinematic shapes. (The expected signal and background rates in this study are summarized in Table 8.1.)

In HEP data analyses, the systematic uncertainties are generally evaluated by varying parameters or approaches, and quantifying the effects on the expected distributions. Systematic uncertainties from different sources are assumed to be uncorrelated. The sources of systematic uncertainties considered in this study, are documented in this chapter.

7.1 Luminosity Uncertainties

The luminosity measurement is calibrated by beam-separation scans [67], which was performed in November 2012 (after the regular data-taking periods). The beam-separation scans also determine the uncertainty on the luminosity measurement, which is 2.8% for the 2012 data-taking. The luminosity uncertainty is evaluated by

varying the normalization of all physics processes that are estimated using Monte Carlo simulation. The data-driven backgrounds are not normalized with the luminosity.

7.2 Uncertainties on Reconstructed Objects

The uncertainties on reconstructed objects are treated similarly for all four analysis channels, and they are considered correlated for all kinematic regions. Below is a list of all such uncertainties considered in this study.

7.2.1 *Lepton Trigger, Reconstruction, and Identification Efficiencies*

For electrons and muons, the efficiencies of triggers, reconstruction, and identification (including isolation requirements), differ slightly between data and simulation. Thus, correction factors are derived using tag-and-probe methods on $Z \rightarrow \ell\ell$ events, and applied to simulation samples to account for efficiency differences. This study considers the uncertainties on these correction factors [52, 53], which can come from finite statistics and various assumptions in the tag-and-probe efficiency measurements. These uncertainties are evaluated as a function of the p_T , η , and ϕ of the reconstructed leptons. The electron identification uncertainties are one of the most important systematic uncertainties for the 3L and 4L analysis channels.

7.2.2 *Lepton Momentum Scale and Resolution*

Simulation of the lepton momentum scale and resolution is examined using the position and width of the $Z \rightarrow \ell\ell$ and $J/\Psi \rightarrow \ell\ell$ mass spectra, as well as the $W \rightarrow \ell\nu$ events. Small discrepancies between data and simulation are observed, and corrected using rescaling and smearing procedures. The uncertainties associated with the rescaling and smearing procedures [68, 53] are (separately) considered in this study. These uncertainties are evaluated as a function of the p_T , η , and ϕ of the

reconstructed leptons. When evaluating these uncertainties, the variations in the momenta of electrons and muons are propagated into the E_T^{miss} calculation.

7.2.3 Jet Reconstruction Efficiencies

The efficiencies of jet reconstruction are studied in dijet events, using a tag-and-probe method [69]. The jet reconstruction efficiencies in simulation are found to be slightly higher ($\sim 0.2\%$) than those in data, for low p_T ($p_T < 20$ GeV) jets. Jet reconstruction is found to be almost fully efficient for high p_T jets. Uncertainties on the jet reconstruction efficiencies are considered in this study, by randomly removing jets in simulated events according to the above efficiency differences. The analysis of an event, including jet-related kinematic variable calculations and event selections, is then redone with the modified jet list.

7.2.4 Jet Vertex Fraction Efficiencies

As described in Chapter 5, the jet vertex fraction (JVF) requirement is applied to jets. The efficiencies for jets to satisfy the JVF requirement are studied in $Z \rightarrow \ell\ell + \text{jets}$ events in data and simulation samples, including events enriched in jets from hard scatterings, as well as events enriched in jets from pileup interactions. The uncertainties associated with the scale factors that match the JVF efficiencies in simulation to data have two components: the fit uncertainty and the selection uncertainty. These uncertainties are incorporated in this study by varying the JVF scale factors, up and down by 1σ .

7.2.5 Jet Energy Scale

The jet energy scale (JES) uncertainties are derived from the test beam data, LHC collision data, and simulation [54]. The JES uncertainties include those from in situ JES calibration (including the statistical, detector, and modeling uncertainties), relative calibration for forward jets ($|\eta| > 0.8$), jets with very high p_T (> 400 GeV),

pileup interactions, close-by jets, jet flavor composition and response, and b -jet energy scale. The JES uncertainties are split into 22 orthogonal systematic sources in total, which have different p_T and η dependencies. These systematics are (separately) varied to evaluate the total impact of the JES uncertainties. The altered jet energies are propagated into the calculation of E_T^{miss} . The JES uncertainties are among the dominant uncertainties in the 2OSL, 2SSL, and 3L analysis channels.

7.2.6 Jet Energy Resolution

The jet energy resolution (JER) is measured using two different in situ methods [70]. The results of the measurement agree well between data and simulation. An associated systematic uncertainty is defined using the difference in JER between data and simulation. This uncertainty is applied using a smearing procedure on the simulation samples, and symmetrized manually. The smearing will change the jet energies for every simulated event, and these altered jet energies are propagated into the calculation of E_T^{miss} . The JER uncertainty is calculated as a function of jet η and p_T , and is one of the major uncertainties for the 3L analysis channel.

7.2.7 Flavor Tagging

The number of b -tagged jets in each event is used in this measurement. Thus the uncertainties associated with the b -tagging efficiencies and mis-tagging rates need to be considered. The b -tagging efficiencies and mis-tagging rates are measured using control samples for each jet flavor, from which correction factors are derived to match simulation with data [57, 58]. For b -jets (c -jets), the correction factors and associated uncertainties are derived using dilepton $t\bar{t}$ events (using jets associated with D^* mesons). In both cases, they are binned by jet p_T . For light flavor jets, the correction factors and associated uncertainties are derived using dijet events, and binned by both jet p_T and η . The uncertainties for b -jets, c -jet, and light flavor jets are

treated as uncorrelated, and each is further divided into a set of orthogonal systematic sources. Additional uncertainties are defined to account for the extrapolation of the corrections factors from jets with lower p_T to jets with higher p_T (where the statistics are limited), for b -jets, c -jets, and light flavor jets, respectively. These systematics are (separately) varied to evaluate the total impact of the flavor tagging uncertainties.

7.2.8 Soft Terms in Missing Transverse Momentum Calculation

As mentioned above, the systematic variations on lepton momentum scale, lepton momentum resolution, jet energy scale, and jet energy resolution are propagated to the E_T^{miss} calculation. In addition, the uncertainties on the soft terms in the E_T^{miss} calculation [59] are taken into account in this study. These terms are assembled using topological clusters that are not associated with high p_T physics objects, such as electrons and jets. The energy scale and resolution of the soft terms are (separately) varied within their uncertainties, in order to evaluate their impact on the E_T^{miss} calculation. These are treated as uncorrelated to other systematic uncertainties.

7.3 Uncertainties on Signal Modeling

Systematic uncertainties on the theoretical $t\bar{t}V$ cross section calculations are not included in this study, since we are measuring these cross sections. However, the systematic effects on the $t\bar{t}V$ kinematics need to be considered, which are documented in this section. These uncertainties are treated as correlated for all four analysis channels.

The $t\bar{t}W$ and $t\bar{t}Z$ processes are simulated using MADGRAPH for the matrix element calculation, and PYTHIA for the parton showering. The PDF set used is CTEQ6L1. There exist several uncertainties associated with the signal modeling:

- Renormalization and factorization scale

For the renormalization and factorization scales, the nominal values are taken to be $\mu_R = \mu_F = 2m_t + m_Z$. To evaluate the signal uncertainties due to these scales, the values are varied around the nominal ones, in the **MADGRAPH** generator. Both scales are (simultaneously) multiplied by a factor of 2 and a factor of 0.5 for up and down variations, respectively.

- Radiation

PYTHIA and **MADGRAPH** are used to model the initial and final state radiation. One uncertainty is determined by simultaneously varying the scale of the momentum transfer Q for the strong coupling constant $\alpha_s(Q)$ in both the **PYTHIA** and **MADGRAPH** generators, up and down by a factor of 2. In addition, another uncertainty is determined by varying the amount of radiation up and down by a factor of 2 in the **PYTHIA** generator.

- MLM matching

The MLM matching is used to combine the **MADGRAPH** matrix element calculation and **PYTHIA** parton showering. The uncertainty with doing this is evaluated by varying the jet p_T threshold up and down by 5 GeV (around 20 GeV) used in the MLM matching.

For the above signal modeling uncertainties, simulation samples are produced by **MADGRAPH** and **PYTHIA** with the same configuration as the nominal samples, except for the specific parameters being varied. To save processing time, these variation samples are not passed through the detector simulation. Thus, the signal modeling uncertainties are estimated by comparing the truth record of the nominal samples with that of the variation samples. The reconstructed events of the nominal samples are then reweighted according to the differences found at the truth level.

The dominant uncertainty among the $t\bar{t}V$ signal modeling uncertainties is the

uncertainty associated with the momentum transfer Q in $\alpha_s(Q)$, which has a significant effect on the kinematic distributions in $t\bar{t}V$ events. The effects of the other signal modeling uncertainties are relatively negligible.

In addition to the above modeling uncertainties, the uncertainties due to the choice of the parton distribution functions (PDF) in $t\bar{t}V$ modeling are also included. These uncertainties are evaluated by constructing an envelope of the variations in the CT10 NLO, MSTW2008 NLO, and NNPDF NLO [71] PDF sets, following the PDF4LHC recommendations [72]. Both the variations within each PDF set, and the differences among these PDF sets are considered. The PDF uncertainties of signal modeling are found to be small in this study.

7.4 Uncertainties on Background Modeling

This section documents the uncertainties on background modeling in this study. Some background modeling uncertainties are considered correlated among all four analysis channels, while the others are treated as uncorrelated among the analysis channels, depending on the background features and estimation methods.

7.4.1 $Z+jets$ Background

The $Z+jets$ background only affects the 2OSL analysis channel, but dominates the $2\ell-Z$ regions. For the modeling of this background, four (independent) systematic sources are considered, which are the uncertainties associated with the $Z+jets$ cross section (4%), the Z p_T correction (described in Chapter 6), the parton emission, and the choice of matrix element generator. The last two systematic sources are evaluated by comparing the nominal ALPGEN sample with the SHERPA sample, which calculates LO matrix elements with up to three additional partons.

7.4.2 $t\bar{t}$ Background

The $t\bar{t}$ background only affects the 2OSL analysis channel, but dominates the 2ℓ -no Z regions. Several (independent) systematic sources are considered for its modeling. They are the uncertainty on the $t\bar{t}$ cross section (+5%/-6%), the uncertainty on the parton showering and hadronization modeling (evaluated by comparing the default sample with the sample produced by POWHEG interfaced with HERWIG), the uncertainty on the choice of matrix element generator (evaluated by comparing the default sample with the sample produced by MADGRAPH interfaced with PYTHIA), as well as the uncertainty on the reweighting procedure to correct certain $t\bar{t}$ distributions (described in Chapter 6). The default $t\bar{t}$ sample is produced by POWHEG interfaced with PYTHIA. In addition, a 50% normalization uncertainty is applied to the events of $t\bar{t}$ + heavy flavor jets, because the understanding of this process is relatively limited.

7.4.3 Single Top Background

The single top background also only affects the 2OSL analysis channel, with small contributions from Wt production. For this background, a 6.8% normalization uncertainty is assigned, to account for the theoretical uncertainty on the Wt cross section. In addition, another uncertainty is evaluated by comparing predictions from different schemes for the interface between the Wt and $t\bar{t}$ processes.

7.4.4 Diboson Background

In the 2SSL and 3L analysis channels, the largest diboson background is due to WZ production, while in the 4L analysis channel, the largest diboson background is due to ZZ production. For the 2OSL analysis channel, the diboson backgrounds include WW , WZ , ZZ production, but the contributions are relatively small.

In the 3L and 2SSL analysis channels, the normalization of the WZ background is

treated as a free parameter in the final likelihood fit, and no uncertainty on the WZ production cross section is included. For the uncertainty on the kinematics of the WZ process, we compare the nominal SHERPA sample with the POWHEG sample, as well as utilize variations of generator parameters. This uncertainty is found to be at the level of 20%-35%.

Similarly, in the 4L, 3L and 2SSL analysis channels, the normalization of the ZZ background is treated as a free parameter in the final likelihood fit, and no uncertainty on the ZZ production cross section is included. The uncertainty on the kinematics of the ZZ process are treated differently among those channels. In the 3L and 2SSL analysis channels, we again compare the nominal SHERPA sample with the POWHEG sample, as well as utilize variations of generator parameters. In the 4L analysis channel, several uncertainties are considered. An uncertainty due to the extrapolation from the control region with on-shell ZZ production to the signal regions with off-shell ZZ production, and an uncertainty due to the extrapolation from the control region without jets to the signal regions with at least one jet, are found to be 30% and 20%, respectively, using data-driven methods. In addition, a normalization uncertainty of 10%-30% is applied to the events of $ZZ +$ heavy flavor jets, which is based on a data/simulation comparison in events with one Z boson and additional jets.

In the 2OSL analysis channel, a 20% normalization uncertainty is assigned to the sum of the WW , WZ , and ZZ processes. This uncertainty is based on the level of agreement between data and simulation in the 3ℓ - Z -0b3j control region.

7.4.5 $t\bar{t}H$ Background

A 12% normalization uncertainty is assigned to $t\bar{t}H$ production in all analysis channels, due to the $t\bar{t}H$ cross section calculation. Only in the 2OSL analysis channel, are additional uncertainties for the $t\bar{t}H$ kinematics assigned, which are those associated

with the renormalization and factorization scales, and the functional form of these scales. These uncertainties are negligible for the other analysis channels.

7.4.6 tZ and WtZ Backgrounds

In the 2OSL, 2SSL, and 3L analysis channels, tZ and WtZ backgrounds are summed together. A 20% normalization uncertainty is assigned in these three analysis channels, for the cross section calculations. Only in the 3L analysis channel, where these backgrounds are important, is an uncertainty on the kinematics included. This uncertainty is evaluated by varying the renormalization and factorization scales, as well as α_S (the strong coupling constant) in simulation. The α_S variation is found to have a larger effect, which is 10% to 20% depending on the jet and b -jet multiplicity.

In the 4L analysis channel, the tZ background makes no contribution, while the WtZ background is important. An uncertainty of 10% is assigned due to the WtZ cross section, derived from the variation of the renormalization and factorization scales. Another uncertainty for the modeling of the jets in WtZ events is evaluated by varying the relevant parameters in simulation.

7.4.7 Other Physics Backgrounds

For the triboson and same-sign WW processes, 100% normalization uncertainties are (separately) assigned. For the WH and ZH processes, 20% normalization uncertainties are assigned, based on the cross section calculations.

7.4.8 Charge Mis-identification Background

The electron charge mis-identification background affects the same-sign ee and $e\mu$ regions. To obtain the uncertainties on this background, several sources of systematic uncertainties are considered:

- Statistical uncertainties due to limited data in the charge mis-ID rate measure-

ment:

We vary up and down the charge mis-ID rates within the corresponding statistical uncertainties, simultaneously for all lepton p_T and η bins. This is found to be comparable to varying the charge mis-ID rates, separately for each lepton bin. This is the main source of uncertainties for the charge mis-ID background.

- Sideband subtraction:

When measuring the charge mis-ID rates, we subtract the sidebands from the Z peak to remove the non- Z component. Charge mis-ID rates measured with no sideband subtraction are used to generate another charge mis-ID background estimation. The difference in these estimates is used to evaluate the uncertainty of the non- Z component modeling.

- Difference of charge mis-ID rates between Z +jets and $t\bar{t}$:

We measure the charge mis-ID rates in a Z +jets dominant region of data, while in the signal region, the charge mis-ID events are mostly from $t\bar{t}$. To estimate the uncertainty associated with this, we first extract charge mis-ID rates from the ALPGEN Z +jets sample, using the described likelihood method. We then use the POWHEG $t\bar{t}$ sample to perform a closure test, requiring both top quarks to decay leptonically and two truth-matched reconstructed leptons. The charge mis-ID rates are applied to the opposite-sign $t\bar{t}$ events to estimate the charge mis-ID, which are then compared to the same-sign events. The difference is found to be small. Finally, a conservative 10% normalization uncertainty on the charge mis-ID background estimation is given to cover the difference.

The total effect of the systematic effects on the charge mis-ID estimation is of the order of 25%.

7.4.9 *Fake Lepton Background*

The fake lepton background is important in the 2SSL, 3L, and 4L analysis channels. In these channels, several systematic sources are considered to obtain the total uncertainties on the fake lepton backgrounds.

- Statistical uncertainties due to limited events in the fake rate measurement:

We vary up and down the fake rates within the corresponding statistical uncertainties, separately for each fake rate bin. The fake rates refer to fake factors for the 2SSL channel, real/fake efficiencies for the 3L channel, and fake rate correction factors for the 4L channel. This is the main uncertainty source for the fake lepton background.

- Modeling of the prompt lepton and charge mis-ID contributions:

The normalizations of the prompt lepton and charge mis-ID contributions, estimated from Monte Carlo samples and data-driven methods, is (separately) adjusted up and down (by 20-25%) in the fake rate measurements, to determine these additional systematic sources. The magnitude of the normalization change is depending on the analysis channels, and chosen to conservatively reflect the approximate upper bound on the total uncertainty of these backgrounds in this study.

In the 3L analysis channel, an additional uncertainty on the fake lepton background is evaluated by measuring the fake rates in two orthogonal regions: one with one or two jets, and the other with three or more jets. Fake lepton background estimates are produced with fake rates measured from these regions, and compared with the estimate produced with the nominal fake rates. All the uncertainties associated with the fake lepton background are treated as they are uncorrelated among the analysis channels.

In the 2OSL analysis channel, the fake lepton background is small and estimated using simulation. A 50% normalization uncertainty is applied to the fake lepton background in this channel, in order to cover the difference in rates between the simulation and another estimate using two same-sign lepton events in data. An additional uncertainty is applied to cover the difference in the shapes between the two estimates.

8

Results

A likelihood fit procedure is used to extract the $t\bar{t}W$ and $t\bar{t}Z$ cross sections from the four analysis channels. This chapter first describes the statistical tools, and then presents the event yields and cross section results.

8.1 Statistical Tools

In general, results of high energy physics data analyses are distributions (templates): one for data, and many for signal and background processes (which are used to compare with the data). Each template consists of one or more kinematic regions, and each region consists of one or more discriminant bins. The region and bin configurations are the same among all templates. The templates for signal and background processes are produced by Monte Carlo simulation or data-driven methods.

A likelihood function, L , is defined as the probability of observing the data distribution, given a certain physics hypothesis. It is the product of L_i , the likelihood for each bin i :

$$L = \prod_i L_i \quad (8.1)$$

L_i is the product of a Poisson probability \mathcal{P}_i and a Gaussian probability term. The Poisson probability \mathcal{P}_i is the probability of observing N_i^{obs} events when expecting N_i^{exp} events, for bin i . The Gaussian probability term incorporates all systematic uncertainties, and each systematic uncertainty is parameterized by a nuisance parameter α_j .

$$L_i(\mu, \alpha_j) = \mathcal{P}_i(N_i^{\text{obs}} | N_i^{\text{exp}}(\mu, \alpha_j)) \prod_{j \in \text{syst}} \mathcal{G}(\alpha_j) \quad (8.2)$$

The Gaussian probability \mathcal{G} for each nuisance parameter α_j is:

$$\mathcal{G}(\alpha_j) = \frac{1}{\sqrt{2\pi}} e^{-\alpha_j^2/2} \quad (8.3)$$

The Poisson probability \mathcal{P}_i is

$$\mathcal{P}_i(N_i^{\text{obs}} | N_i^{\text{exp}}(\mu, \alpha_j)) = \frac{(N_i^{\text{exp}})^{N_i^{\text{obs}}} \cdot e^{-N_i^{\text{exp}}}}{N_i^{\text{obs}}!} \quad (8.4)$$

The nuisance parameter α_j describes the level of variation for a systematic uncertainty. In particular, $\alpha_j = 0$ corresponds to no systematic variation from the nominal expectation, while $\alpha_j = \pm 1$ correspond to $\pm 1\sigma$ systematic variations. The effects of the $\pm 1\sigma$ variations on the expectation are quantified by dedicated studies, as described in Chapter 7. For the variations in between and beyond the three sampling points of $+1\sigma$, nominal, and -1σ , interpolation methods are utilized.

In addition, μ is the signal strength (the ratio of the measured cross section to the theoretical cross section) for signal processes. The expected number of events, N_i^{exp} , is a function of μ and α_j :

$$N_i^{\text{exp}} = \sum_{\text{sig}} N_i^{\text{sig}}(\mu, \alpha_j) + \sum_{\text{bg}} N_i^{\text{bg}}(\alpha_j) \quad (8.5)$$

where N_i^{sig} is the expected number of signal events, depending on μ and α_j ; N_i^{bg} is the expected number of background events, depending on α_j . Technically, they are calculated from the templates for signal and background processes. (These templates can be with or without systematic variations.)

With the constructed likelihood function, physics quantities can be obtained using statistical procedures. For example, by maximizing the likelihood function, we can extract the signal strength μ , and thus the signal cross section. The corresponding uncertainty of the estimation of μ can be obtained from the relation between the likelihood function and μ .

In the statistical procedures, the nuisance parameters are initially set to zero, and floated within Gaussian constraints as shown in Equation 8.3. The effects of the systematic variations on the normalization and shape of signal or background templates are then simultaneously taken into account in the likelihood function. This approach of dealing with systematic uncertainties is referred to as “profiling.”

Furthermore, we can calculate signal significance (for discovery) or upper limits (for exclusion) using the following procedure. First, a test statistic needs to be constructed, which converts the discrimination power into a single number. The LHC experiments commonly use the likelihood ratio as test statistic:

$$q_\mu = -2 \ln \frac{L(\mu, \hat{\alpha}_j)}{L(\hat{\mu}, \hat{\alpha}_j)} \quad (8.6)$$

In the denominator, $\hat{\mu}$ and $\hat{\alpha}_j$ are the best fit values for μ and α_j , respectively. Thus, the denominator is the likelihood of the best fit with μ floated. In the numerator, μ is fixed, and $\hat{\alpha}_j$ is the best fit value for α_j with the fixed μ . Thus, the numerator is

the likelihood of the best fit with a given μ . If data is in good agreement with the hypothesis of the given μ , q_μ will be close to zero.

With this test statistic definition, we can obtain an expected distribution of q_μ , using pseudo-experiments: with a given hypothesis, generate pseudo-data using signal and background templates, and calculate q_μ . We can repeat the above pseudo-experiment for a large number of times, and plot the distribution of q_μ . Often, we calculate the q_μ distributions for the $\mu = 0$ (background only hypothesis) and $\mu = 1$ (signal plus background hypothesis) cases.

However, conducting pseudo-experiments usually takes lots of computing resource. Sometimes the expected distribution of q_μ is approximated using an asymptotic formula [73]. This approach works only when the number of observed events $N_{obs} \geq 10$.

In addition, the observed template also results in a q_μ value, q_{obs} . From q_{obs} and the expected q_μ distribution, we can calculate the p value, which describes the probability to obtain the observed template, or more extreme templates:

$$p = \int_{q_{obs}}^{\infty} f(q_\mu | \mu) dq_\mu \quad (8.7)$$

where the $f(q_\mu | \mu)$ is the q_μ probability density function with a given hypothesis, derived from the expected distribution of q_μ . Often, we calculate p values for the background only hypothesis and signal plus background hypothesis, referred to as p_b and p_{s+b} , respectively.

From p_b , we can further calculate the z-value, or signal significance, using the following relation:

$$p = \int_z^{\infty} \frac{1}{\sqrt{2\pi}} e^{-x^2/2} dx \quad (8.8)$$

The significance can be used to quantify “discovery.” In high energy physics data analyses, we usually regard a 5σ result as a “discovery” of the signal, and a 3σ result

as “evidence” for the signal.

From p_b and p_{s+b} , we can further calculate the upper limit, using the so-called CL_s approach. CL_s is defined as

$$CL_s = \frac{p_{s+b}}{1 - p_b} \quad (8.9)$$

If the CL_s value is found to be smaller than certain threshold α , the signal plus background hypothesis is rejected at a confidence level of $1 - \alpha$. The commonly used α value is 0.05, which corresponds to a 95% confidence level.

In this measurement, the likelihood function is constructed using the HistFactory [74]+RooFit [75] framework. The further statistical procedures, including the maximization of the likelihood function, and the calculation of signal significance is performed in the RooStats [76] framework.

8.2 Expected and Observed Event Rates

The likelihood fit of this measurement uses 5 control regions and 15 signal regions defined by the four analysis channels. The expected event rates of signals and backgrounds, as well as the observed event rates, in all of these regions are shown in Table 8.1. The expected event rates are obtained after applying the event selection described in Chapter 6, and are inputs to the likelihood fit that is used to extract the $t\bar{t}W$ and $t\bar{t}Z$ cross sections. These expected events are normalized using the theoretical cross sections listed in Table 4.1.

8.3 Cross Section Results

In this study, the measured production cross sections $\sigma_{t\bar{t}W}$ and $\sigma_{t\bar{t}Z}$ are simultaneously extracted. Using the statistical techniques described in Section 8.1, we first construct a profiled likelihood function with all the discriminant bins in the control

Table 8.1: Expected event rates of signals and backgrounds, as well as observed event rates, in all 5 control regions and 15 signal regions used in the likelihood fit. The control regions are labeled with an “*”. The total background is split into 3 categories. $t + X$ includes the $t\bar{t}$, single top, tZ , $t\bar{t}H$ and $t\bar{t}t\bar{t}$ backgrounds. “Bosons” includes the $Z+jets$, WW , WZ , ZZ , $W^\pm W^\pm$, and triboson backgrounds. Instrumental background includes the fake lepton and charge mis-ID backgrounds. The quoted uncertainties are the total uncertainties on expected rates, including the MC statistical uncertainties.

Region	$t + X$	Bosons	Instrumental background	Total background	$t\bar{t}W$	$t\bar{t}Z$	Data
2 ℓ -no Z -3j*	20800 ± 2600	600 ± 200	160 ± 80	21600 ± 2700	42.0 ± 2.8	23.2 ± 1.5	22585
2 ℓ -no Z -4j	8200 ± 1400	240 ± 90	80 ± 40	8600 ± 1400	36.6 ± 1.8	22.4 ± 1.1	8909
2 ℓ -no Z -5j	3700 ± 850	100 ± 40	47 ± 23	3810 ± 870	24.9 ± 2.2	22.4 ± 2.0	3901
2 ℓ - Z -3j*	800 ± 140	1960 ± 880	4.1 ± 2.1	2760 ± 890	1.24 ± 0.13	3.71 ± 0.38	2806
2 ℓ - Z -4j*	330 ± 70	740 ± 390	2.2 ± 1.1	1100 ± 400	1.31 ± 0.11	7.21 ± 0.58	1031
2 ℓ - Z -5j	170 ± 40	340 ± 200	1.4 ± 0.7	510 ± 210	0.89 ± 0.07	17.7 ± 1.4	471
$2e$ -SS	0.66 ± 0.13	0.17 ± 0.10	8.9 ± 2.4	9.8 ± 2.6	2.97 ± 0.30	0.93 ± 0.23	16
$e\mu$ -SS	1.9 ± 0.35	0.39 ± 0.28	14.1 ± 4.5	16.4 ± 5.1	8.67 ± 0.76	2.16 ± 0.51	34
$\mu\mu$ -SS	0.94 ± 0.17	0.25 ± 0.14	0.93 ± 0.55	2.12 ± 0.86	4.79 ± 0.40	1.12 ± 0.27	13
3 ℓ - Z -0b3j*	1.11 ± 0.32	67 ± 16	15.2 ± 6.0	83 ± 15	0.05 ± 0.03	1.86 ± 0.47	86
3 ℓ - Z -1b4j	1.58 ± 0.42	3.8 ± 1.3	2.4 ± 1.1	7.8 ± 1.6	0.14 ± 0.05	7.1 ± 1.6	8
3 ℓ - Z -2b3j	1.29 ± 0.34	0.68 ± 0.33	0.19 ± 0.13	2.16 ± 0.42	0.21 ± 0.07	2.76 ± 0.69	3
3 ℓ - Z -2b4j	1.00 ± 0.29	0.48 ± 0.24	0.42 ± 0.37	1.93 ± 0.49	0.14 ± 0.07	6.6 ± 1.6	11
3 ℓ -no Z -2b	1.06 ± 0.25	0.27 ± 0.17	1.31 ± 0.90	2.7 ± 0.9	3.7 ± 0.9	1.23 ± 0.32	6
4 ℓ -DF-0b	0.06 ± 0.01	0.11 ± 0.04	0.03 ± 0.17	0.21 ± 0.22	-	0.28 ± 0.01	2
4 ℓ -DF-1b	0.22 ± 0.03	0.05 ± 0.03	0.13 ± 0.22	0.39 ± 0.27	-	1.05 ± 0.03	1
4 ℓ -DF-2b	0.11 ± 0.02	< 0.01	0.11 ± 0.19	0.22 ± 0.21	-	0.64 ± 0.02	1
4 ℓ - ZZ *	0.01 ± 0.00	134.2 ± 1.2	0.27 ± 0.18	134.5 ± 1.3	-	0.07 ± 0.01	158
4 ℓ -SF-1b	0.16 ± 0.02	0.29 ± 0.06	0.14 ± 0.19	0.61 ± 0.27	-	0.91 ± 0.02	2
4 ℓ -SF-2b	0.08 ± 0.01	0.09 ± 0.03	0.04 ± 0.18	0.21 ± 0.23	-	0.64 ± 0.02	1

regions and signal regions of the four analysis channels. We then fit the data to the signal and background processes by maximizing the likelihood function. The parameters of interest in the likelihood fit are the signal strengths of the $t\bar{t}W$ and $t\bar{t}Z$ processes, as well as the normalizations of the WZ and ZZ processes.

From the likelihood fit, the $t\bar{t}W$ and $t\bar{t}Z$ production cross sections are measured to be:

- $\sigma_{t\bar{t}W} = 369^{+86}_{-79}$ (stat.) ± 44 (syst.) fb $= 369^{+100}_{-91}$ fb

- $\sigma_{t\bar{t}Z} = 176^{+52}_{-48}$ (stat.) ± 24 (syst.) fb = 176^{+58}_{-52} fb

Table 8.2: Breakdown of the uncertainties on the measured $t\bar{t}W$ and $t\bar{t}Z$ cross sections.

Uncertainty	$\sigma_{t\bar{t}W}$	$\sigma_{t\bar{t}Z}$
Luminosity	3.2%	4.6%
Reconstructed objects	3.7%	7.4%
Background from simulation	5.8%	8.0%
Fake leptons and charge mis-ID	7.5%	3.0%
Signal modeling	1.8%	4.5%
Total systematics	12%	13%
Statistical	+24% / -21%	+30% / -27%
Total	+27% / -24%	+33% / -29%

Table 8.2 provides a breakdown of the uncertainties on the measured $t\bar{t}W$ and $t\bar{t}Z$ cross sections. The numbers are determined by allowing one signal cross section to float in the fit while fixing the other signal cross section to its theoretical value. As shown in Table 8.2, statistical uncertainties dominate for the measurement of both processes. For the $t\bar{t}W$ measurement, the largest systematic uncertainties are those associated with the modeling of the fake lepton and charge mis-identification backgrounds. For the $t\bar{t}Z$ measurement, the largest systematic uncertainties are those associated with the modeling of the physics backgrounds, such as the WZ and ZZ processes.

Figure 8.1 plots expected yields returned by the likelihood fit compared to observed yields in the control regions and signal regions. The x-axis corresponds to different regions: 5 control regions (used to constrain the $t\bar{t}$, $Z+jets$, ZZ , and WZ backgrounds), three 2OSL signal regions, three 2SSL signal regions, four 3L signal regions, and five 4L signal regions, from the left to the right. The y-axis corresponds to event yields of each region. These regions are used in the likelihood fit for the simultaneous extraction of the $t\bar{t}W$ and $t\bar{t}Z$ production cross sections. The 2OSL and 2SSL signal regions shown consist of multiple discriminant bins, as described

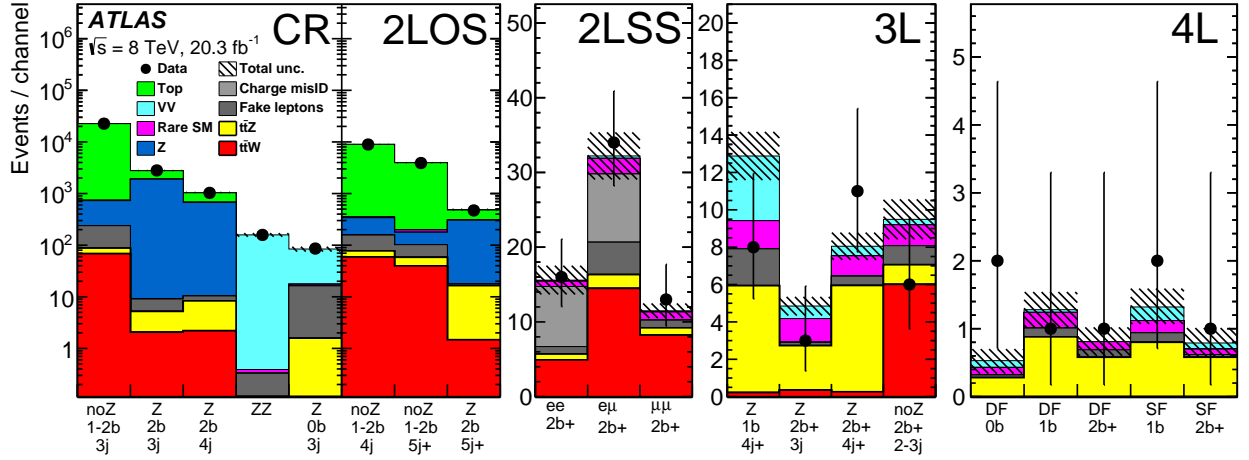


FIGURE 8.1: Expected yields after the likelihood fit compared to observed yields in the control regions and signal regions. The hatched areas include both statistical and systematic uncertainties on the expected yields.

in Chapter 6. The signal strengths of the $t\bar{t}W$ and $t\bar{t}Z$ processes, as well as the normalizations of the WZ and ZZ processes, are extracted from the likelihood fit, and applied to the expected yields. As shown in the figure, the post-fit agreement between expectation and observation is good.

Table 8.3: Expected and observed signal significance of the $t\bar{t}W$ and $t\bar{t}Z$ processes from each analysis channel and the combination of all analysis channels.

Channel	$t\bar{t}W$ significance		$t\bar{t}Z$ significance	
	Expected	Observed	Expected	Observed
2OSL	0.4σ	0.1σ	1.4σ	1.1σ
2SSL	2.8σ	5.0σ	-	-
3L	1.4σ	1.0σ	3.7σ	3.3σ
4L	-	-	2.0σ	2.4σ
Combined	3.2σ	5.0σ	4.5σ	4.2σ

Signal significance is also calculated from the constructed likelihood function, using the asymptotic formula approach. Table 8.3 provides the expected and observed signal significance of the $t\bar{t}W$ and $t\bar{t}Z$ processes from each analysis channel and the combination of all analysis channels. The significance of $t\bar{t}W$ ($t\bar{t}Z$) is calculated

using the null hypothesis without $t\bar{t}W$ ($t\bar{t}Z$), while floating the signal strength of $t\bar{t}Z$ ($t\bar{t}W$) in the likelihood fit. As shown in the table, the $t\bar{t}W$ signal significance is mainly from the 2SSL channel, while the $t\bar{t}Z$ signal significance is mainly from the 3L and 4L channels. Combining four analysis channels, the $t\bar{t}W$ ($t\bar{t}Z$) signal significance is expected to be 3.2σ (4.5σ), and measured to be 5.0σ (4.2σ). This represents the first observation of $t\bar{t}W$ production and evidence of $t\bar{t}Z$ production. In addition, the z -value with the null hypothesis with neither $t\bar{t}W$ process nor $t\bar{t}Z$ process is expected to be 5.9σ , and measured to be 7.1σ .

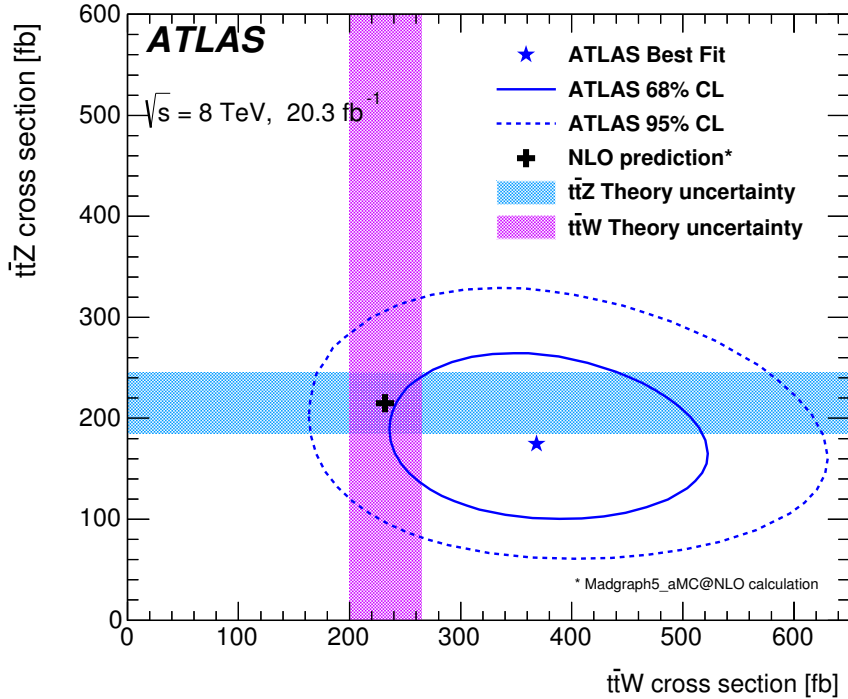


FIGURE 8.2: The measured results of the $t\bar{t}W$ and $t\bar{t}Z$ cross sections compared with the NLO theoretical calculations.

We also compare the measured results of the $t\bar{t}W$ and $t\bar{t}Z$ cross sections with the NLO theoretical calculations, in Figure 8.2. In the figure, the x-axis corresponds to the $t\bar{t}W$ cross section, while the y-axis corresponds to the $t\bar{t}Z$ cross section. The

blue pentagram is the measured results of the $t\bar{t}W$ and $t\bar{t}Z$ cross sections, and the two ellipses are the 68% and 95% CL (confidence level) experimental uncertainty contours. The black cross is the NLO theoretical calculations of the $t\bar{t}W$ and $t\bar{t}Z$ cross sections, and the shaded areas are the 14% theoretical uncertainties, including the renormalization and factorization scale uncertainties, as well as the PDF uncertainties. The figure shows consistency between the experimental measurements and the theoretical calculations for the $t\bar{t}V$ cross sections.

Conclusion

A measurement of the $t\bar{t}W$ and $t\bar{t}Z$ production cross sections is presented. This measurement uses $\int \mathcal{L} dt = 20.3 \text{ fb}^{-1}$ of data from proton-proton collisions at $\sqrt{s}=8 \text{ TeV}$ collected by the ATLAS detector at the LHC in 2012. Four final states are analyzed: two opposite-sign leptons (2OSL), two same-sign leptons (2SSL), three leptons (3L), and four leptons (4L). To simultaneously extract the $t\bar{t}W$ and $t\bar{t}Z$ processes, we fit the data by maximizing a likelihood function over 5 control regions and 15 signal regions from the 4 analysis channels. The $t\bar{t}W$ and $t\bar{t}Z$ production cross sections are measured to be: $\sigma_{t\bar{t}W} = 369^{+100}_{-91} \text{ fb}$ and $\sigma_{t\bar{t}Z} = 176^{+58}_{-52} \text{ fb}$. The $t\bar{t}W$ signal significance is found to be 5.0σ , while the $t\bar{t}Z$ signal significance is found to be 4.2σ .

This measurement is one of the first published measurements of the $t\bar{t}V$ cross sections. It represents the first 5σ observation of the $t\bar{t}W$ process, and a strong evidence of the $t\bar{t}Z$ process. The results are consistent with the NLO QCD theoretical calculations for the $t\bar{t}W$ and $t\bar{t}Z$ processes. This consistency provides an important validation for the Standard Model, in particular, for the top-EWK couplings. Furthermore, the results will become important inputs for $t\bar{t}H$ measurements and new physics searches. However, the measured $t\bar{t}W$ cross section is about 1σ larger

than the Standard Model prediction. This might be due to statistical fluctuation, an underestimation of the $t\bar{t}W$ cross section in the NLO QCD theoretical calculations, or a beyond-Standard-Model process contributing to the $t\bar{t}V$ signal regions. With the Run 1 dataset, we are not able to make any conclusion.

It will be important to measure the $t\bar{t}V$ processes using the LHC Run 2 data. With the LHC collision energy increasing from 8 TeV to 13 TeV, the production rates of these processes become significantly higher. The Run 2 $t\bar{t}V$ analysis can possibly be done using the same four final states of the Run 1 analysis. It might improve the sensitivity to extend the analysis strategy of the 2SSL analysis channel (global fit), to the 3L and 4L analysis channels. A feasibility study is presented in Appendix A. On the other hand, one difficulty of the analysis will be estimation of instrumental backgrounds, including both charge mis-identification and fake lepton backgrounds. An estimation with smaller systematic uncertainties is preferred, using Monte Carlo simulation and/or data-driven methods.

Appendix A

Feasibility Study of Extending the Global Fit Method to the Three Lepton Final States for the $t\bar{t}V$ Measurements

In the published $t\bar{t}V$ measurement of the ATLAS experiment, the two opposite-sign lepton (2OSL) and two same-sign lepton (2SSL) analysis channels utilize both the rate and shape information of each signal region, while the three lepton (3L) and four lepton (4L) analysis channels utilize only the rate information (event count) of each signal region. In this appendix, we extend the global fit analysis strategy of the 2SSL channel to 3L events, and study whether it improves the signal sensitivities. This study will benefit the future $t\bar{t}V$ analyses.

The event pre-selection of this feasibility study is similar with the 3L analysis documented in Chapter 6. Events are required to have three leptons with $p_T > 15$ GeV (including a trigger-matched lepton with $p_T > 25$ GeV), and not to have a total electric charge of $+3e$ or $-3e$. 3L events are then split into a 3ℓ - Z region and a 3ℓ -no Z region. The 3ℓ - Z region requires a Z boson candidate, which is a pair of same-flavor opposite-sign leptons, with $m_{\ell\ell} - m_Z < 10$ GeV. The 3ℓ -no Z region contains the

remaining 3L events. The 3ℓ - Z region targets the $t\bar{t}Z$ process, while the 3ℓ -no Z region targets the $t\bar{t}W$ process. The main background in the 3ℓ - Z region is WZ production, and in the 3ℓ -no Z region is the fake lepton background. Furthermore, we require events to have at least one b -tagged jet, for both the 3ℓ - Z region and the 3ℓ -no Z region.

For simplicity, all the backgrounds in this feasibility study are estimated using Monte Carlo simulation. The physics backgrounds, including the WZ , ZZ , triboson, tZ , and $t\bar{t}H$ processes, are estimated using events with real prompt leptons in the corresponding simulation samples. The fake lepton background, however, is estimated using events with at least one mis-identified or non-prompt lepton in the simulation samples of the above physics backgrounds, as well as the $W/Z+jets$, $t\bar{t}$, single top, and WW processes. The fake lepton events are split into four categories, depending on the fake lepton flavor and physics process: a fake electron from a heavy-flavor (HF) jet; a fake muon from a heavy-flavor (HF) jet; a fake electron from a light-flavor (LF) jet; a fake muon from a light-flavor (LF) jet. No correction on the fake lepton background estimation is applied in this study.

Also for simplicity, this feasibility study only considers statistical uncertainties and the major systematic uncertainties. We assign a 30% normalization uncertainty to the WZ modeling, a 30% normalization uncertainty to the ZZ modeling, a 100% normalization uncertainty to the triboson modeling, a 15% normalization uncertainty to the tZ modeling, and a 20% normalization uncertainty to the $t\bar{t}H$ modeling. The four categories of the fake lepton background are separately assigned a 50% normalization uncertainty. In addition, a 2.8% luminosity uncertainty is applied to all processes, including the fake lepton background. No systematic uncertainty on object reconstruction and signal modeling is considered in this study.

The distributions in jet multiplicity and missing transverse momentum for the 3ℓ - Z region and the 3ℓ -no Z region are shown in Figure A.1 and Figure A.2. The

agreement between data and Monte Carlo simulation is found to be reasonable. (The hatched areas include only statistical uncertainties.) As shown in the figures, the signal $t\bar{t}V$ processes tend to have larger missing transverse momentum and jet multiplicity than the background processes.

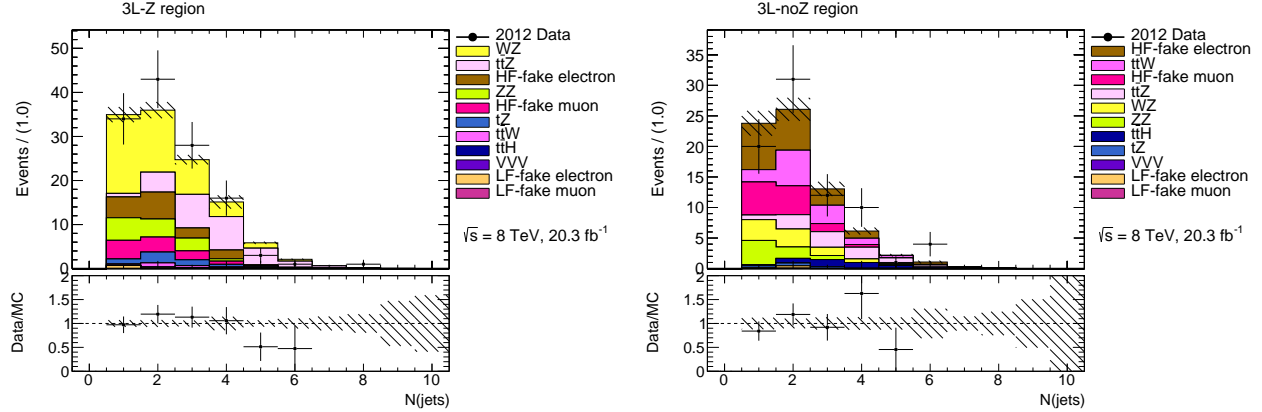


FIGURE A.1: The distributions in jet multiplicity for the 3ℓ - Z region (left) and the 3ℓ -no Z region (right). The events are required to contain three leptons and at least one b -tagged jet. The instrumental backgrounds are predicted using Monte Carlo simulation. The hatched areas include only statistical uncertainties.

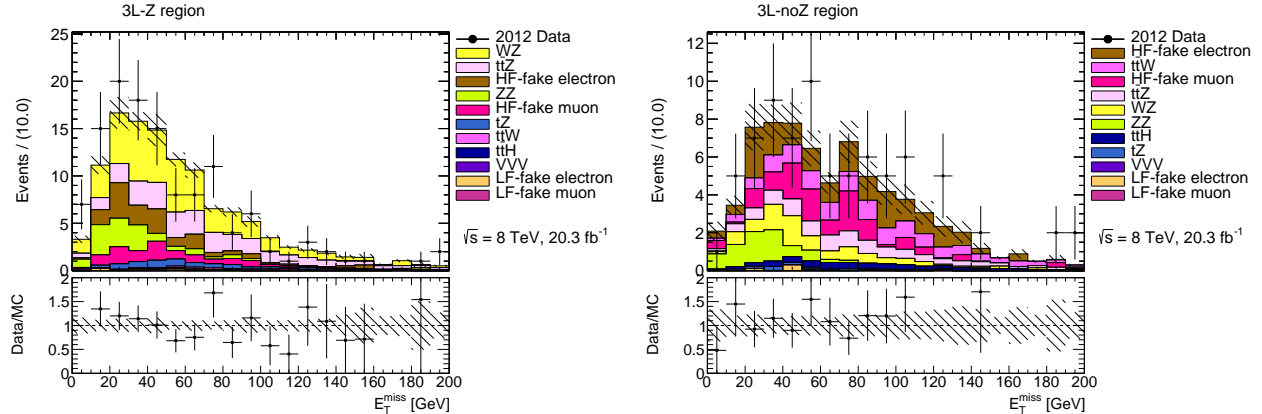


FIGURE A.2: The distributions in missing transverse momentum for the 3ℓ - Z region (left) and the 3ℓ -no Z region (right). The events are required to contain three leptons and at least one b -tagged jet. The instrumental backgrounds are predicted using Monte Carlo simulation. The hatched areas include only statistical uncertainties.

The global fit analysis strategy for the 3L final states is to extract $t\bar{t}W$ and $t\bar{t}Z$ events in a phase space of Z candidate existence, jet (b -jet) multiplicity, and E_T^{miss} , because the signal processes and the background processes are naturally separated in such a phase space. A likelihood function is then constructed to fit the data to the expected distributions of the signal and background processes, which are from Monte Carlo simulation.

The following binning configurations are considered for constructing the phase space:

- Z candidate axis: Z , no Z
- b -jet multiplicity axis: 2 $N_{b\text{-jets}}$ bins (1, ≥ 2), or 1 $N_{b\text{-jets}}$ bin (≥ 2 only)
- jet multiplicity axis: 2 N_{jets} bins (2-3, ≥ 4), or 4 N_{jets} bins (2, 3, 4, ≥ 5)
- E_T^{miss} axis: 1 E_T^{miss} bin, or 2 E_T^{miss} bins (< 80 GeV, ≥ 80 GeV)

An optimization is performed by scanning the binning scenarios and analyzing the expected significances of the $t\bar{t}W$ and $t\bar{t}Z$ signals, considering the statistical uncertainties and the major systematic uncertainties. Each binning scenario is a combination of the binning options for the b -jet multiplicity, jet multiplicity and E_T^{miss} axes.

The results of the optimization using the $N_{b\text{-jets}} \geq 1$ events and two $N_{b\text{-jets}}$ bins is shown in Table A.1. As can be seen, the 3 ℓ - Z region is mostly for the $t\bar{t}Z$ signal, and the 3 ℓ -no Z region is for both the $t\bar{t}W$ and $t\bar{t}Z$ signals. In addition, more N_{jets} and E_T^{miss} bins slightly improves the signal sensitivities. For the 3 ℓ - Z region, the best expected significance is 0.3σ for $t\bar{t}W$ and 3.8σ for $t\bar{t}Z$, from the scenario of 2 E_T^{miss} bins and 4 N_{jets} bins. For the 3 ℓ -no Z region, the best expected significance is 1.5σ for $t\bar{t}W$ and 1.4σ for $t\bar{t}Z$, from the scenario of 2 E_T^{miss} bins and 4 N_{jets} bins. Combining the above two scenarios, the $t\bar{t}W$ expected significance is found to be 1.6σ , and the

Table A.1: Selected results of the optimization using 3L events with $N_{b\text{-jets}} \geq 1$. The optimization considers the statistical uncertainties and the major systematic uncertainties.

Bin configuration	$t\bar{t}W$ expected significance	$t\bar{t}Z$ expected significance
3 ℓ -Z, 1 E_T^{miss} bin, 2 N_{jets} bins	0.2 σ	3.5 σ
3 ℓ -Z, 1 E_T^{miss} bin, 4 N_{jets} bins	0.2 σ	3.7 σ
3 ℓ -Z, 2 E_T^{miss} bins, 2 N_{jets} bins	0.2 σ	3.6 σ
3 ℓ -Z, 2 E_T^{miss} bins, 4 N_{jets} bins	0.3 σ	3.8 σ
3 ℓ -noZ, 1 E_T^{miss} bin, 2 N_{jets} bins	1.4 σ	1.2 σ
3 ℓ -noZ, 1 E_T^{miss} bin, 4 N_{jets} bins	1.5 σ	1.2 σ
3 ℓ -noZ, 2 E_T^{miss} bins, 2 N_{jets} bins	1.4 σ	1.3 σ
3 ℓ -noZ, 2 E_T^{miss} bins, 4 N_{jets} bins	1.5 σ	1.4 σ

Table A.2: Selected results of the optimization using 3L events with $N_{b\text{-jets}} \geq 2$. The optimization considers the statistical uncertainties and the major systematic uncertainties.

Bin configuration	$t\bar{t}W$ expected significance	$t\bar{t}Z$ expected significance
3 ℓ -Z, 1 E_T^{miss} bin, 2 N_{jets} bins	0.2 σ	3.4 σ
3 ℓ -Z, 1 E_T^{miss} bin, 4 N_{jets} bins	0.2 σ	3.5 σ
3 ℓ -Z, 2 E_T^{miss} bins, 2 N_{jets} bins	0.2 σ	3.5 σ
3 ℓ -Z, 2 E_T^{miss} bins, 4 N_{jets} bins	0.3 σ	3.5 σ
3 ℓ -noZ, 1 E_T^{miss} bin, 2 N_{jets} bins	1.3 σ	1.0 σ
3 ℓ -noZ, 1 E_T^{miss} bin, 4 N_{jets} bins	1.3 σ	1.1 σ
3 ℓ -noZ, 2 E_T^{miss} bins, 2 N_{jets} bins	1.4 σ	1.0 σ
3 ℓ -noZ, 2 E_T^{miss} bins, 4 N_{jets} bins	1.4 σ	1.1 σ

$t\bar{t}Z$ expected significance is found to be 4.0σ . If dropping the additional N_{jets} binning and E_T^{miss} binning in the combination, the $t\bar{t}W$ expected significance is found to be 1.4σ , and the $t\bar{t}Z$ expected significance is found to be 3.7σ .

The results of the optimization using only the $N_{b\text{-jets}} \geq 2$ events is shown in Table A.2. As can be seen, the signal sensitivities are significantly worse than using the $N_{b\text{-jets}} \geq 1$ events and two $N_{b\text{-jets}}$ bins.

In the published ATLAS $t\bar{t}V$ measurement, four signal regions are defined for the 3L analysis channel, which are listed below. In the likelihood fit to extract the $t\bar{t}V$ cross sections, the discriminant of these signal regions is the event count.

- 3 ℓ -Z-1b4j: 3 ℓ -Z events with at least four jets, exactly one of which is b -tagged.

- 3ℓ - Z - $2b3j$: 3ℓ - Z events with exactly three jets, at least two of which are b -tagged.
- 3ℓ - Z - $2b4j$: 3ℓ - Z events with at least four jets, at least two of which are b -tagged.
- 3ℓ - $\text{no}Z$ - $2b$: 3ℓ - $\text{no}Z$ events with at least two b -tagged jets.

For comparison, this approach is also studied using the simplified treatments. The expected significance is found to be 1.4σ for $t\bar{t}W$, and 3.7σ for $t\bar{t}Z$. The performance of this approach is not as good as the global fit approach, but still comparable (the four signal region definitions carry some shape information of the inclusive 3L events).

In addition, we need to notice that the background estimation and systematic uncertainties are simplified in this feasibility study. Thus, we should not directly compare the results here with the published results. However, we can compare different scenarios within this study and obtain insights. As shown above, the global fit method improves the signal sensitivities, by about 0.2σ for both $t\bar{t}W$ and $t\bar{t}Z$.

Appendix B

ATLAS Phase II Inner Tracker Upgrade

As my service task for the ATLAS experiment, I have contributed to the ATLAS inner tracker upgrade in three aspects, which are documented as follows.

B.1 Introduction

The high-luminosity upgrades of the LHC and its experiments will be installed during the phase II upgrade (around the year of 2025). The goal is to achieve an instantaneous luminosity of around $\sim 10^{35} \text{ cm}^{-2}\text{s}^{-1}$, and record collision data of an integrated luminosity of $\sim 3000 \text{ fb}^{-1}$ by the year of 2035. During the phase II upgrade, ATLAS will replace the current inner detectors (Pixel+SCT+TRT) with a silicon-based inner tracker (ITk) [77], due to the radiation damage of operation and the requirements for higher pile-up. (If not being replaced, after the phase II upgrade, the current inner detectors will reach the maximum radiation fluence, and their readout electronics and granularity are not able to cope with the ~ 100 pile-up interactions in each collision.) Building the ITk detector will be the largest upgrade activity for the ATLAS experiment. It will significantly affect the physics prospects of the ATLAS

experiment with higher luminosity. Furthermore, the techniques developed for the ITk will be useful for future particle detectors.

The ITk detector will consist of a silicon pixel sub-detector and a silicon strip sub-detector (from inside to outside). The principles of both sub-detectors have been described in Chapter 3. However, many new technologies (such as smaller silicon sensors, ABC 130nm readout chips, lightweight support structures) will be utilized to enhance the detector capabilities.

The letter of intent (LOI) layout for the ITk detector is shown in Figure B.1. In the figure, the red component is the pixel sub-detector, consisting of 4 barrel layers and 6 endcap disks. The blue component is the strip sub-detector, consisting of 6 barrel layers (the area of the 5th barrel layer is reduced) and 6 endcap disks. The $|\eta|$ coverage is up to 2.5 for the ITk detector, and up to 3.0 for the pixel sub-detector. One thing to note is that, at the time of writing, the LOI layout is one of several layouts being investigated, and the final ITk layout has not been decided.

B.2 Simulation and performance of the ATLAS inner tracker

I worked on simulation and performance of the ITk detector in the ATLAS+ITk software framework. I compared the performance of different detector layouts, non-active material amounts, and types of beam spot, by exploring tracking efficiencies and parameter resolutions using simulation samples. In addition, I also compared the full simulation with the fast simulation, and identified some issues that resulted in a previously unexplained disagreement of the two approaches.

As an example of this work, Figure B.2 shows the d_0 resolutions with different non-active material amounts for electrons, muons and pions. In each figure, the x-axis corresponds to $|\eta|$, and the y-axis corresponds to d_0 resolutions. The green curves are for the default material amount, while the red (black) curves are for decreasing (increasing) the material amount of both the pixel and strip sub-detectors by 30%.

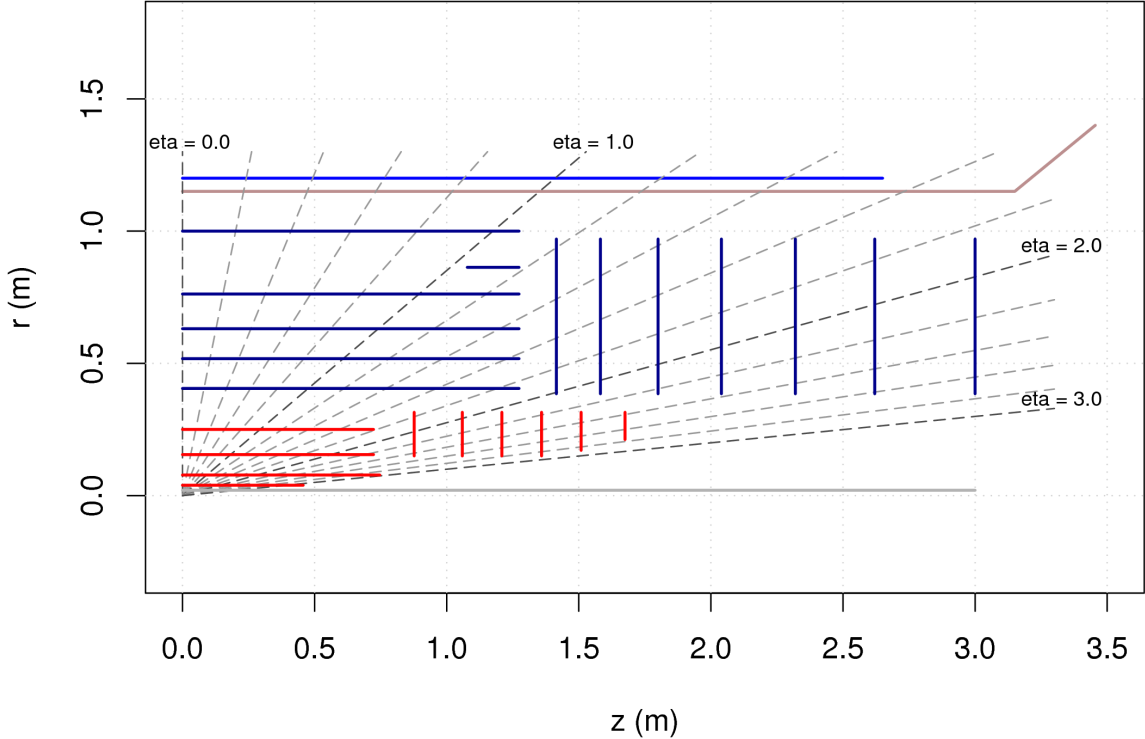


FIGURE B.1: The letter of intent (LOI) layout for the ITk detector.

As can be seen, decreasing material amount improves d0 resolutions, especially for low p_T particles.

B.3 Building silicon module test stands at Duke/ANL

For the ATLAS phase II upgrade, the Duke HEP group is mainly involved in the strip sub-detector, especially the testing of modules. (Each strip module includes ~ 20 readout chips and each readout chip is bonded to ~ 200 silicon strip sensors.) For this, I led the construction of a module test stand at Duke. After building the current test stand with an HSIO (high speed input output) board and an ABCN 250nm single readout chip board, I made the test stand work with the Scientific Linux operating system and conducted tests on the single readout chip board. At the time of writing, I am helping develop a water/glycol cooling system for single module and upgrade the test stand with an Atlys board. (Both the HSIO board and

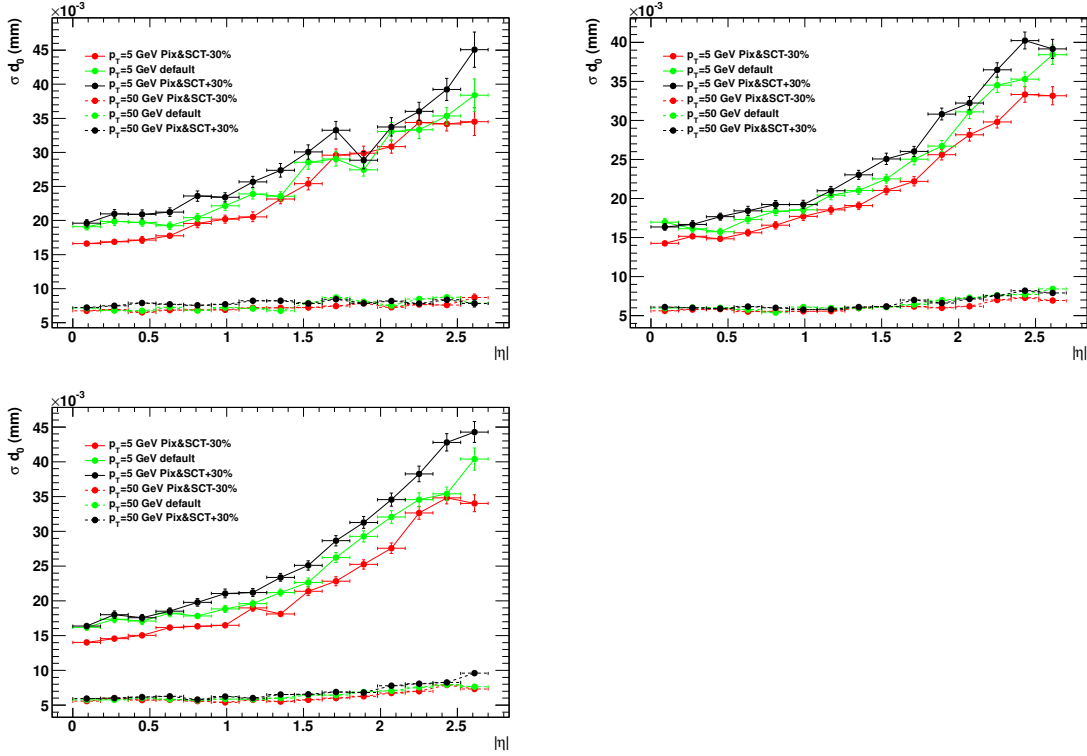


FIGURE B.2: The d_0 resolutions with different non-active material amounts for electrons (top-left), muons (top-right), and pions (bottom-left). The error bars include only statistical uncertainties.

Atlys board are for data acquisition (DAQ) purposes and programmable.) In addition, I also helped the construction of a similar test stand at ANL (Argonne National Laboratory).

Figure B.3 shows the DAQ system setup for the module test stand at Duke. In the photo, there is an ABCN 250nm single readout chip board (test part), and an HSIO board (DAQ board), from top to bottom. In addition, a Xilinx programmer (red) is connected to the HSIO board, which can be used to assign firmware files. The Atlys board and power supplies are not shown in the photo.

Figure B.4 shows the results of a 3-point gain scan on the ABCN 250nm single readout chip board at Duke. The 3-point gain scan is one of the most important tests for the ATLAS silicon detectors. It injects three different charges (0.52fC,

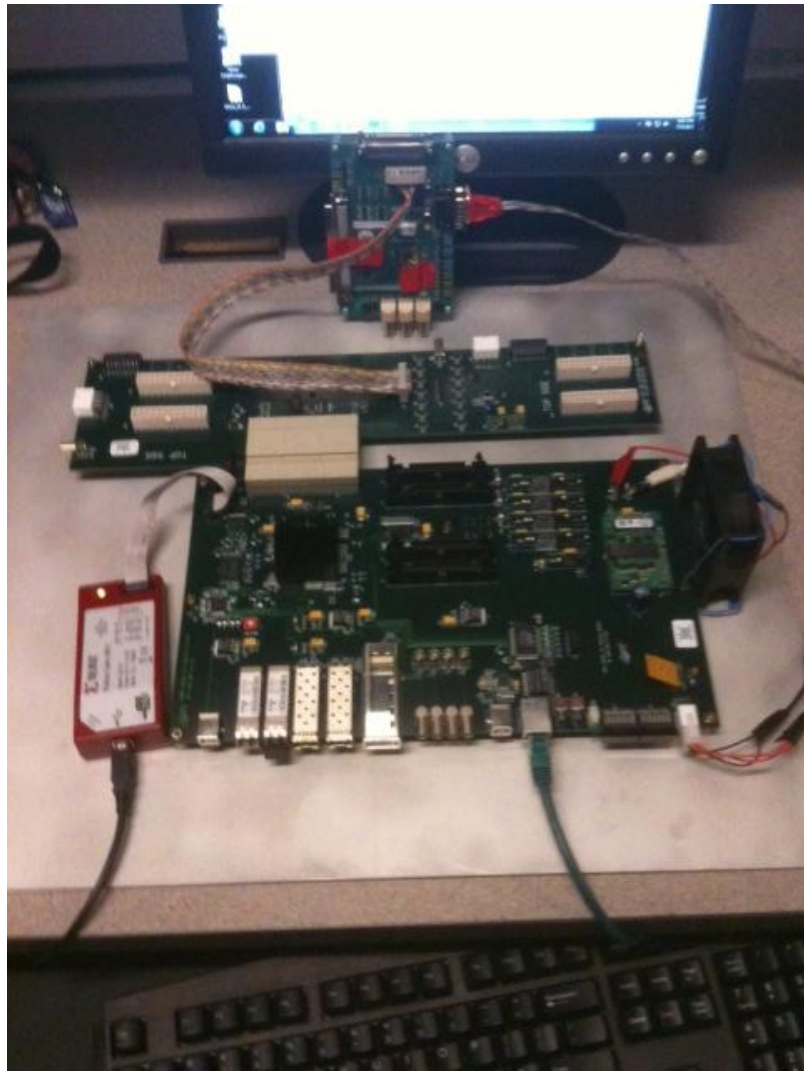


FIGURE B.3: The DAQ system setup for the module test stand at Duke.

1.0fC, 1.48fC), and performs threshold scans (varying the detection threshold of a chip, sending a given number of triggers to the chip, and counting the number of triggers detected) for each injected charge. There are several important parameters associated with the 3-point gain scan:

- V_{t50} (shown in the first row of Figure B.4), the threshold corresponding to a 50% occupancy.
- The output noise, the variance of the threshold distribution.

ATLAS SCT Module Test: Response vs. Channel - Tue Oct 20

Page 1 Run 19 Start Scan 4 Stream 0 Module 0 (ABCNx1_0)

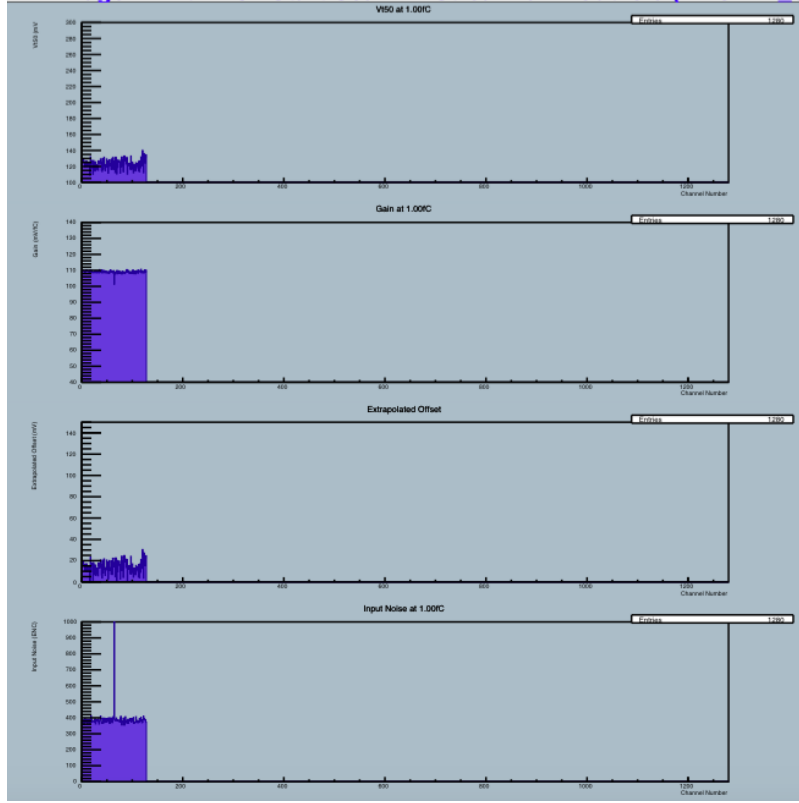


FIGURE B.4: The results of a 3-point gain scan on the ABCN 250nm single readout chip board at Duke.

- The gain (shown in the second row of Figure B.4), from a linear fit of V_{t50} versus injected charges.
- The offset (shown in the third row of Figure B.4), from the above linear fit.
- The input noise (shown in the fourth row of Figure B.4), the result of dividing the output noise by the gain.

The above parameters are measured for every channel (corresponding to every silicon strip sensor) of a chip. The ABCN 250nm single readout chip board at Duke is found to work normally.

B.4 Testing of silicon detectors at CERN

I also played an important role in the silicon detector testing at CERN. I helped develop a CO_2 cooling system, which can be used to test the silicon detector performance in a low temperature environment. Also, tests on silicon detectors were conducted to better understand the noise. In the summer of 2015, I helped move the silicon upgrade facilities to a radiation lab at CERN, and worked on the assembling and recommissioning of the facilities.

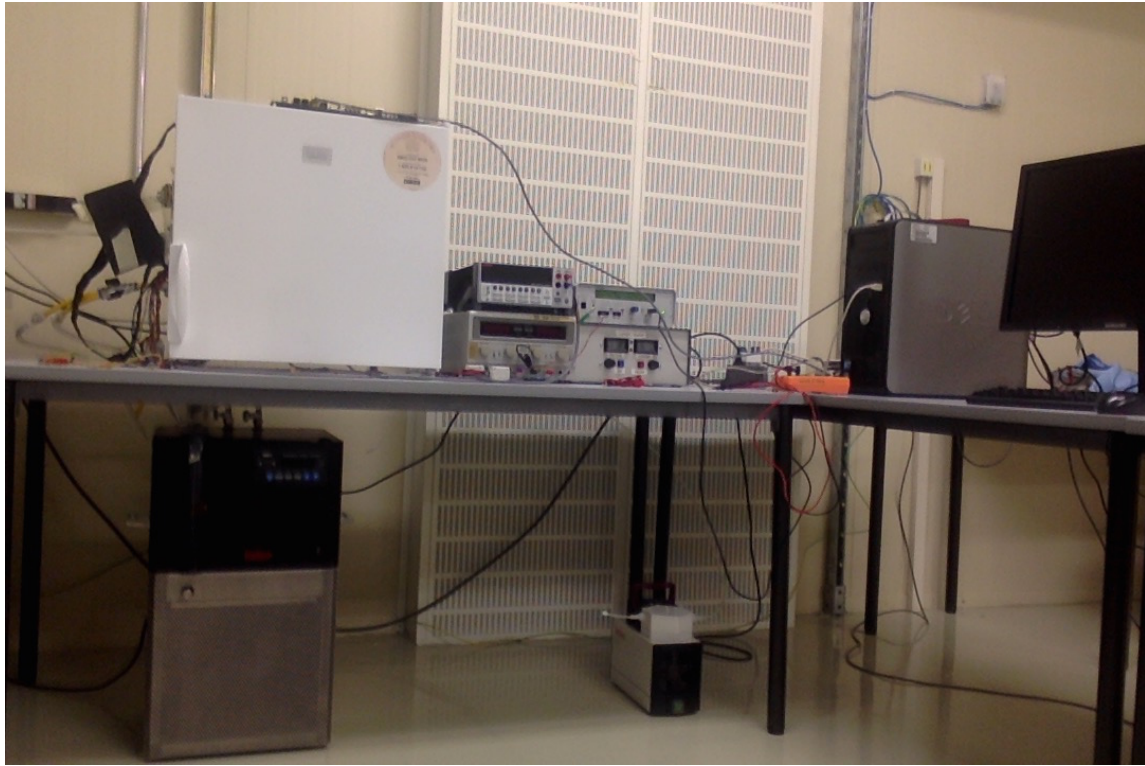


FIGURE B.5: A module test stand at a radiation lab at CERN.

Figure B.5 shows a module test stand at the radiation lab at CERN, which I assembled and recommissioned. In the photo, under the desk is a water cooling chiller and a vacuum pump (from left to right). On the desk is a container (with a silicon module inside), various power supplies, and a DAQ PC (from left to right). In addition, an HSIO board is placed on the top of the container.

Appendix C

Search for Association Production of an Upsilon Meson with a W or Z Boson at CDF

During 2011-2013, I searched for association production of an Upsilon meson (Υ) with a W or Z boson using data from the CDF experiment. The observation of these processes can provide a good test of the non-relativistic QCD models, as well as hints of potential contributions from non-standard-model physics. The search is performed using the $\Upsilon \rightarrow \mu\mu$ decay together with the charged lepton decay modes of the W and Z bosons. Having not seen evidence for $\Upsilon + W/Z$ production, we then calculate cross section limits, which are currently the most sensitive limits for these processes. I was the main analyzer of this analysis, working on signal modeling (Monte Carlo), background estimation (data-driven), event selection, systematic uncertainty calculation, as well as result interpretation. Below is part of the published paper of this analysis.

C.1 Introduction

The standard model production of an upsilon (Υ) meson in association with a W boson or a Z boson is a rare process whose rate was first calculated in Ref. [78], where ΥW and ΥZ production occur through the parton-level processes producing $W + b\bar{b}$ and $Z + b\bar{b}$ final states, in which the $b\bar{b}$ pair may form a bound state (either an Υ or an excited bottomonium state that decays to an Υ). More recently, rates for these processes have been calculated at next-to-leading-order in the strong-interaction coupling for proton-antiproton ($p\bar{p}$) collisions at 1.96 TeV center-of-mass energy and proton-proton collisions at 8 TeV and 14 TeV [79].

The cross sections calculated for ΥW and ΥZ production in $p\bar{p}$ collisions at 1.96 TeV are 43 fb and 34 fb, respectively. These values were calculated at leading-order using the MADONIA quarkonium generator [80] as detailed below and are roughly a factor of ten smaller than the earlier calculations from Ref. [78]. The calculations of these processes are very sensitive to the non-relativistic quantum-chromodynamic (NRQCD) models, especially the numerical values of the long-distance matrix elements (LDME), which determine the probability that a $b\bar{b}$ will form a bottomonium state. Measurements of $\Upsilon + W/Z$ cross sections are important for validating these NRQCD models.

Supersymmetry (SUSY) is an extension of the standard model (SM) which has not been observed. Reference [78] describes some SUSY models in which charged Higgs bosons can decay into ΥW final states with a large branching fraction (\mathcal{B}). Similarly, in addition to the expected decays of a SM Higgs to an ΥZ pair, further light neutral scalars may decay into ΥZ . Therefore, if the observed rate of ΥW and/or ΥZ production is significantly larger than the predicted SM rate, it may be an indication of physics not described by the SM.

In 2003, the CDF collaboration reported [81] a search for the associated produc-

tion of an Υ meson and a W or Z boson. In that analysis, a sample corresponding to 83 pb^{-1} of 1.8 TeV $p\bar{p}$ collision data collected with the Run I CDF detector was used to set upper limits on the production cross sections (σ) at the 95% confidence level (C.L.) of $\sigma(p\bar{p} \rightarrow \Upsilon W) \times \mathcal{B}(\Upsilon \rightarrow \mu^+ \mu^-) < 2.3\text{ pb}$ and $\sigma(p\bar{p} \rightarrow \Upsilon Z) \times \mathcal{B}(\Upsilon \rightarrow \mu^+ \mu^-) < 2.5\text{ pb}$.

Here we present a search for $\Upsilon + W/Z$ production, using a sample corresponding to 9.4 fb^{-1} of 1.96 TeV $p\bar{p}$ collision data collected with the CDF II detector. We use the dimuon decay channel to identify the Υ meson. We use only the electron and muon decay channels of the W and Z bosons, which give the best sensitivities for this search.

C.2 The CDF Detector

The CDF II detector is a nearly azimuthally and forward-backward symmetric detector designed to study $p\bar{p}$ collisions at the Tevatron. It is described in detail in Ref. [82]. It consists of a magnetic spectrometer surrounded by calorimeters and a muon-detection system. Particle trajectories are expressed in a cylindrical coordinate system, with the z axis along the proton beam and the x axis pointing outward from the center of the Tevatron. The azimuthal angle (ϕ) is defined with respect to the x direction. The polar angle (θ) is measured with respect to the z direction, and the pseudorapidity (η) is defined as $\eta = -\ln(\tan \frac{\theta}{2})$. The momentum of charged particles is measured by the tracking system, consisting of silicon strip detectors surrounded by an open-cell drift chamber, all immersed in a 1.4 T solenoidal magnetic field. The tracking system provides charged-particle trajectory (track) information with good efficiency in the range $|\eta| \lesssim 1.0$. The tracking system is surrounded by pointing-geometry tower calorimeters, that measure the energies of electrons, photons, and jets of hadronic particles. The electromagnetic calorimeters consist of scintillating tile and lead absorber, while the hadronic calorimeters are composed of scintillating

tiles with steel absorber. The calorimeter system includes central and plug subdetectors, with the central region covering $|\eta| < 1.1$ and the plug region covering the range $1.1 < |\eta| < 3.6$. The muon system is composed of planar multi-wire drift chambers. In the central region, four layers of chambers located just outside the calorimeter cover the region $|\eta| < 0.6$. An additional 60 cm of iron shielding surrounds this system, and behind that is a second subdetector composed of another four layers of chambers. A third muon subdetector covers the region $0.6 < |\eta| < 1.0$, and a fourth subdetector extends coverage to $|\eta| < 1.5$. Cherenkov luminosity counters measure the rate of inelastic collisions, that is converted into the instantaneous luminosity. A three-level online event-selection system (trigger) is used to reduce the event rate from 2.5 MHz to approximately 100 Hz. The first level consists of specialized hardware, while the second is a mixture of hardware and fast software algorithms. The software-based third-level trigger has access to a similar set of information to that available in the offline reconstruction.

C.3 Monte Carlo and Data Samples

We use a number of quantities based on track and calorimeter information in the event selection. The transverse momentum of a charged particle is $p_T = p \sin \theta$, where p is the particle's momentum. The analogous quantity measured with the calorimeter is transverse energy, $E_T = E \sin \theta$. The missing transverse energy, \cancel{E}_T is defined as $\vec{\cancel{E}}_T = -\sum_i E_T^i \hat{n}_i$, where \hat{n}_i is a unit vector perpendicular to the beam axis and pointing to the center of the i th calorimeter tower. The $\vec{\cancel{E}}_T$ is adjusted for high-energy muons, that deposit only a small fraction of their energies in the calorimeter, and offline corrections applied to the measured energies of reconstructed jets [89] which result from the hadronization of quarks and gluons. We define $\cancel{E}_T = |\vec{\cancel{E}}_T|$. The invariant mass of two leptons is $M_{\ell\ell} = \sqrt{(E_{\ell 1} + E_{\ell 2})^2/c^4 - |\vec{p}_{\ell 1} + \vec{p}_{\ell 2}|^2/c^2}$,

and the transverse mass of a lepton and neutrino (estimated with \not{E}_T) is $M_T = \sqrt{2E_T^\ell \not{E}_T (1 - \cos \xi) / c^3}$ where ξ is the angle between the lepton track and \not{E}_T vector in the transverse plane. For muons, p_ℓ and p_T^ℓ are used rather than their measured energies E_ℓ and E_T^ℓ in the definitions of $M_{\ell\ell}$ and M_T .

The analysis uses events selected with triggers requiring a high- E_T central electron candidate ($E_T > 18$ GeV, $|\eta| < 1.0$) or a high- p_T central muon candidate ($p_T > 18$ GeV/ c , $|\eta| < 1.0$). The integrated luminosity of these samples is 9.4 fb^{-1} . All the search channels include the $\Upsilon \rightarrow \mu\mu$ signal, so we only use data acquired when the muon detectors were operational, resulting in the same integrated luminosity for the electron and muon samples.

We also use a low- p_T dimuon-triggered Υ sample to estimate one of the backgrounds as detailed in Section C.5. The dimuon invariant-mass distribution from this low- p_T sample, whose integrated luminosity is 7.3 fb^{-1} , is shown in Fig. C.1 for the mass range in the region of the Υ resonances.

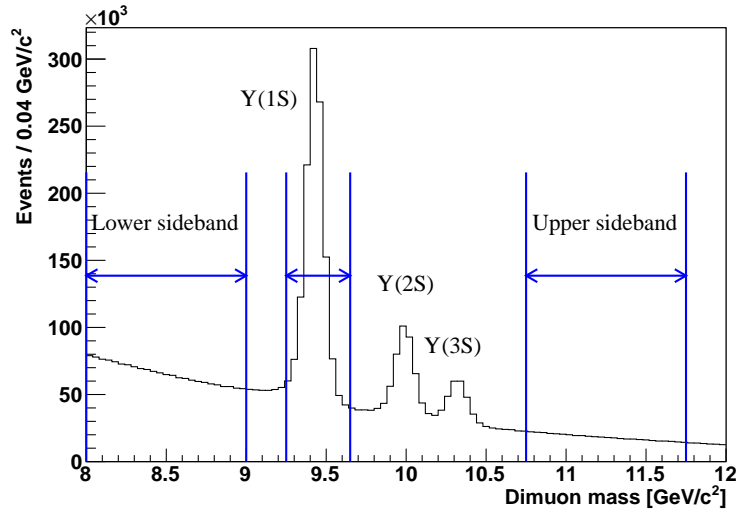


FIGURE C.1: Dimuon invariant-mass spectrum in CDF II data from events contained within the low- p_T dimuon-triggered sample. Shown are the defined Υ signal region and the sideband regions used for background determination.

We produce simulated event samples of the signal processes, ΥW and ΥZ , by first generating events with MADGRAPH [83] and its quarkonium extension MADONIA [80]. We include all ΥW and ΥZ processes from Ref. [78] and the LDME values relevant for the Tevatron from Ref. [84]. An explanation of how LDME values are determined from fits to quarkonia data is given in Ref. [85], although the values obtained in this reference are specific for the LHC. PYTHIA [86] is used to simulate the Υ , W , and Z decays and parton showering. Generated Υ mesons are forced to decay to two muons. We use a GEANT3-based [87] detector simulation to model the response of the CDF II detector [88].

C.4 Event Selection

Events are selected with Υ mesons decaying to muon pairs and decays of vector bosons resulting in at least one electron or muon. In this analysis we have two categories of lepton candidates: low- p_T muon candidates with $1.5 < p_T < 15 \text{ GeV}/c$ from the Υ decay and high- E_T (or p_T) electron (or muon) candidates from the W or Z decay.

High- E_T electron candidates are identified by matching a track to energy deposited within the calorimeter. Muon candidates are formed from charged particle tracks matched to minimum ionizing energy deposition in the calorimeter, which may or may not be matched to track segments in the muon chambers situated behind the calorimeters. Lepton reconstruction algorithms are described in detail elsewhere [91].

Electron candidates are distinguished by whether they are found in the central or forward calorimeters ($|\eta| > 1.1$) where only silicon tracking information is available. The electron selection relies on track quality, track-calorimeter matching, calorimeter energy, calorimeter profile shape, and isolation information. Most muon candidates rely on direct detection in the muon chambers, which are distinguished by their acceptance in pseudorapidity as described above. Remaining muon candidates rely on

track matches to energy deposits consistent with a minimum ionizing charged particle in the central and forward electromagnetic calorimeters respectively, and which fail to have an associated track segment in the muon sub-detectors. All high- E_T (or p_T) leptons are required to be isolated by imposing the condition that the sum of the transverse energy of the calorimeter towers in a cone of $\Delta R \equiv \sqrt{(\Delta\phi)^2 + (\Delta\eta)^2} = 0.4$ around the lepton is less than 10% of the electron E_T (muon p_T).

The analysis uses the high- E_T electron triggered, and high- p_T muon triggered, data sets where events are additionally required to contain $\Upsilon(1S)$ candidates using the Υ decay to two low- p_T muons ($1.5 < p_T < 15 \text{ GeV}/c$). We define the $\Upsilon(1S)$ region as the invariant-mass range $9.25 < M_{\mu\mu} < 9.65 \text{ GeV}/c^2$. We do not use $\Upsilon(2S)$ or $\Upsilon(3S)$ decays. We define two sideband regions, $8.00 < M_{\mu\mu} < 9.00 \text{ GeV}/c^2$ and $10.75 < M_{\mu\mu} < 11.75 \text{ GeV}/c^2$, for obtaining background estimates. Events are required to have at least two low- p_T muon candidates whose invariant mass lies within the $\Upsilon(1S)$ region. To increase the efficiency for reconstructing Υ candidates, we use looser quality requirements on these low- p_T muon candidates than for the high- p_T muon candidates used in the vector-boson reconstruction. In particular, there are no isolation requirements on the Υ muon candidates, and geometrical matching requirements between charged particles in the tracker and track segments in the muon detectors are less stringent. In the small fraction of events (less than 2%) that have more than two low- p_T muons identified, we randomly choose one pair of those muons.

We then look for additional high-energy electron (or muon) candidates consistent with the decay of a vector boson. Events with exactly one high-energy lepton candidate, ℓ , which will henceforth refer to an electron or muon, with E_T (p_T) greater than $20 \text{ GeV} (\text{GeV}/c)$, in addition to the $\Upsilon \rightarrow \mu^+\mu^-$ candidate, and significant missing transverse energy ($\cancel{E}_T > 20 \text{ GeV}$) are selected as $\Upsilon + (W \rightarrow \ell\nu)$ candidates. Such candidates are further required to have a transverse mass in the

range $50 < M_T < 90 \text{ GeV}/c^2$, as expected from a W boson decay. Figure C.2 and Figure C.3 show the distributions of these quantities as predicted from the simulated $\Upsilon + W$ event samples.

Events with two oppositely charged high-energy lepton candidates of same flavor are selected as $\Upsilon + (Z \rightarrow \ell^+ \ell^-)$ candidates. The $\Upsilon + (Z \rightarrow \ell \ell)$ candidates are selected by requiring one additional high- $E_T(p_T)$ electron (muon) candidate with $E_T(p_T) > 20 \text{ GeV} (\text{GeV}/c)$ and a second candidate with the same flavor but opposite charge and $E_T(p_T) > 15 \text{ GeV} (\text{GeV}/c)$. Both additional lepton candidates are required to be isolated and have an invariant mass in the range $76 < M_{\ell\ell} < 106 \text{ GeV}/c^2$. The invariant-mass distribution predicted from the simulated $\Upsilon + (Z \rightarrow \ell \ell)$ event samples is shown in Fig. C.4.

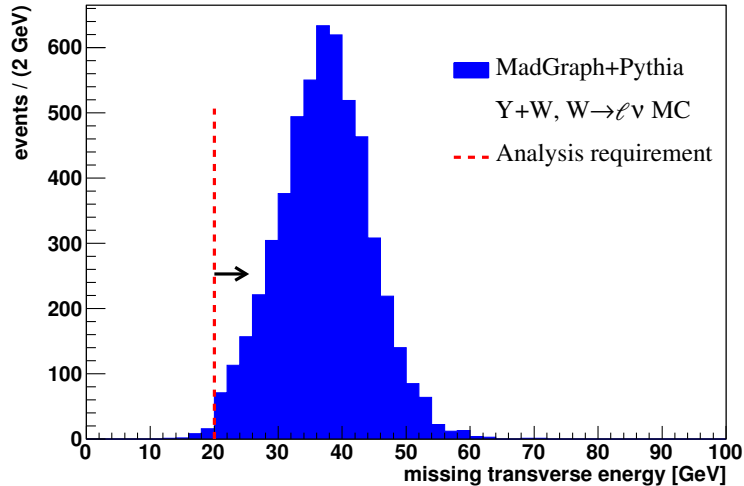


FIGURE C.2: Missing-transverse-energy distributions predicted for signal $\Upsilon + (W \rightarrow \ell \nu)$ events. The distributions are shown for events that satisfy all other event requirements. The scale of the vertical axis is arbitrary.

The total signal efficiencies, after all selection criteria are applied, are determined from simulated event samples to be 1.8% for $\Upsilon + (W \rightarrow e\nu)$, 1.3% for $\Upsilon + (W \rightarrow \mu\nu)$, 1.8% for $\Upsilon + (Z \rightarrow ee)$, and 1.4% for $\Upsilon + (Z \rightarrow \mu\mu)$ events. These efficiencies do not

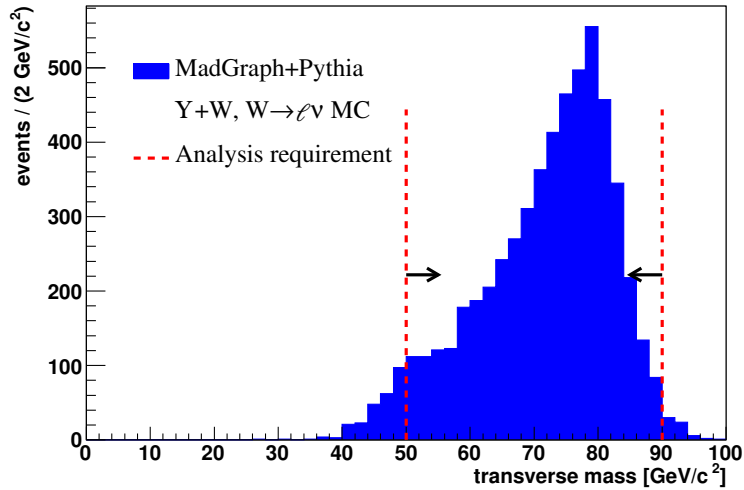


FIGURE C.3: Transverse-mass distributions predicted for signal $\Upsilon + (W \rightarrow \ell\nu)$ events. The distributions are shown for events that satisfy all other event requirements. The scale of the vertical axis is arbitrary.

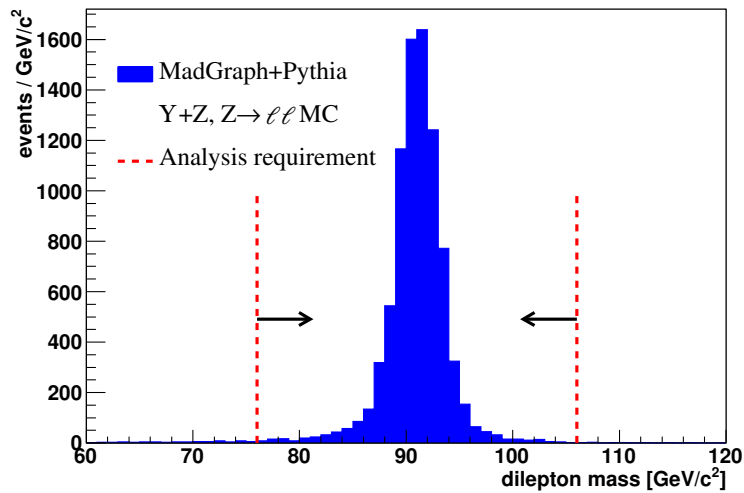


FIGURE C.4: Dilepton invariant-mass distribution predicted for signal $\Upsilon + (Z \rightarrow \ell\ell)$ events. The distribution is shown for events that satisfy all other event requirements. The scale of the vertical axis is arbitrary.

include the branching fractions for $\Upsilon \rightarrow \mu\mu$ and the electronic and muonic decays of the vector bosons. The low acceptances are primarily driven by the geometric acceptance of the drift chamber for the two low- p_T muons from the Υ decay. We expect a small contribution to the $W \rightarrow \ell\nu$ acceptance from $W \rightarrow \tau\nu$ events where the tau lepton decays to an electron or muon. The contribution is determined to be less than 2% of the acceptance, and is therefore neglected. The contribution from $Z \rightarrow \tau\tau$ events to the $Z \rightarrow \ell\ell$ channels is found to be negligible.

Summaries of the selection criteria and their associated efficiencies are given in Tables C.1 and C.2.

Table C.1: Efficiencies for the $(\Upsilon \rightarrow \mu\mu) + (W \rightarrow \ell\nu)$ selection criteria. The individual efficiencies for each requirement, in the given order, are listed with the total at the bottom. The uncertainty on the total efficiency is discussed in the text.

	$\Upsilon + (W \rightarrow e\nu)$	$\Upsilon + (W \rightarrow \mu\nu)$
$\Upsilon(1S) \rightarrow \mu\mu$ candidate	6.8%	6.8%
One additional high- $E_T(p_T)$ isolated e or μ candidate	55%	46%
High- $E_T(p_T)$ lepton candidate is triggerable	55%	52%
$\cancel{E}_T > 20$ GeV	96%	94%
$50 < M_T < 90$ GeV/ c^2	94%	95%
Trigger efficiency	97%	92%
Total	$(1.8 \pm 0.4)\%$	$(1.3 \pm 0.3)\%$

Table C.2: Efficiencies for the $(\Upsilon \rightarrow \mu\mu) + (Z \rightarrow \ell\ell)$ selection criteria. The individual efficiencies for each requirement, in the given order, are listed with the total at the bottom. The uncertainty on the total efficiency is discussed in the text. OS means opposite-sign.

	$\Upsilon + (Z \rightarrow ee)$	$\Upsilon + (Z \rightarrow \mu\mu)$
$\Upsilon(1S) \rightarrow \mu\mu$ candidate	6.7%	7.0%
Two additional OS high- $E_T(p_T)$ isolated e or μ candidates	32%	25%
One of the two high- $E_T(p_T)$ lepton candidates is triggerable	86%	80%
$76 < M_{\ell\ell} < 106$ GeV/ c^2	99%	99%
Trigger efficiency	98%	95%
Total	$(1.8 \pm 0.4)\%$	$(1.4 \pm 0.3)\%$

C.5 Backgrounds

There are two main background contributions to the samples of ΥW and ΥZ signal candidates after the final selection: events containing a correctly identified W/Z candidate and a misidentified Υ candidate (real W/Z + fake Υ) and those with a correctly identified Υ candidate and a misidentified W/Z candidate (real Υ + fake W/Z). Generic dimuon backgrounds, originating predominantly from $b\bar{b}$ production, contribute events in the $\Upsilon(1S)$ mass range and are the primary source of fake Υ candidates. Misidentification of jets as leptons can mimic the decay signatures of W and Z bosons. In the case of Z candidates, where two leptons are required, this background is negligible.

The real W/Z + fake Υ background contributions are estimated by counting the number of W or Z candidate events in the high- p_T lepton data samples that additionally contain a dimuon candidate in the sideband region of the dimuon spectrum (defined in Fig. C.1). An exponential fit to these sideband regions is used to determine a ratio of the areas of the signal to sideband regions, which is then applied to these numbers for an estimate of this background contribution.

The probabilities for reconstructed jets to be misidentified as leptons are measured in jet-enriched data samples as functions of the jet E_T and lepton type, and are corrected for the contributions of leptons from W and Z boson decays, as more fully described in Ref. [90]. To estimate real Υ + fake W/Z background contributions, we select from the low- p_T dimuon data sample events containing a high- E_T jet instead of a high- E_T (p_T) isolated lepton candidate that otherwise satisfy the full selection criteria. Background estimates are obtained using the measured probabilities associated with each of the jets within these events as weighting factors on the potential contribution of each. The low- p_T dimuon sample is relied upon to extract these background estimates because a strong correlation between high- p_T lepton trigger

selection requirements and jet-to-lepton misidentification rates renders the high- p_T lepton data set unsuitable for the chosen methodology. To interpolate between the two samples, additional small corrections are applied to account for differences in the integrated luminosities of the two samples and Υ selection inefficiencies in the low- p_T dimuon sample originating from trigger requirements.

The predicted background contributions to each of the signal samples are summarized in Table C.4. In evaluating the real $Z +$ fake Υ background contribution, no events containing Υ candidates in the sideband mass regions are observed. Background contributions to the corresponding signal samples are therefore estimated by extrapolating from the estimated real $W +$ fake Υ background contributions, using the ratio of Z -to- W cross sections. This makes the assumption that the probability for misidentifying a $\Upsilon(1S)$ is independent of the type of vector boson. In calculating cross-section limits, we also account for small background contributions from ΥZ production to the ΥW samples, originating from events in which one of the two leptons produced in the Z boson decay is not reconstructed.

C.6 Systematic Uncertainties

For determining cross-section limits we incorporate systematic uncertainties on the signal expectation and the background predictions. Systematic uncertainties on the signal expectation include those associated with the integrated luminosity measurement, low- p_T muon identification, high- $E_T(p_T)$ lepton identification, high- $E_T(p_T)$ lepton trigger efficiency, theoretical modeling of the signal, and efficiencies of the event selection criteria. The upsilon-muon identification uncertainty is derived from studies that use data and simulated samples of $J/\psi \rightarrow \mu\mu$ as described in Ref. [92]. Lepton identification and trigger efficiencies are measured using samples of leptonic Z decays [90]. Requirements of $E_T > 20$ GeV ($p_T > 20$ GeV/ c) for electrons (muons) matched to lepton trigger objects ensure a uniform trigger efficiency over the lepton

momentum spectra.

We use the CTEQ6L parton distribution functions (PDFs) [93] for generating the MADGRAPH samples. To estimate the acceptance uncertainty associated with the choice of PDFs, we generate additional samples using MRST PDFs [94] and take the difference in the estimated signal acceptance as the uncertainty.

We vary the bottomonium LDMEs from Ref. [84] by one standard deviation to estimate their effect on the signal acceptance. This procedure results in an additional 6% systematic uncertainty on the signal acceptance. These uncertainties correspond only to those associated with the procedure for computing LDMEs described within the cited reference. Allowing for a wider range of assumptions within the LDME calculations gives rise to additional uncertainties, which are not accounted for in this analysis. However, if an uncertainty of 20% were to be placed on the LDMEs, the cross-section limits we obtain would only increase by about 10%.

With respect to uncertainties associated with event selection criteria, we vary the \cancel{E}_T by $\pm 10\%$ (an estimate of the \cancel{E}_T resolution) in the simulated signal samples to quantify the effect of \cancel{E}_T resolution.

It is possible for the Υ meson and the W or Z boson to originate from different parton-parton interactions in the same $p\bar{p}$ collision. This double-parton-scattering process is difficult to identify, but estimates have been made for several related final states using LHC and Tevatron data (see for example Ref. [95] where J/ψ production in association with a W boson was studied by the ATLAS collaboration). These estimates, together with a calculation using the Υ and vector boson cross sections at the Tevatron collision energy lead to an estimated effect of approximately 15%. Based on lack of knowledge on double-parton scattering, we assign this effect as a systematic uncertainty on the signal acceptance. In Table C.3 we summarize all investigated systematic uncertainties associated with the signal expectation.

Uncertainties on predicted background contributions are also incorporated into

the cross-section limits. For the real W/Z + fake Υ background, we use the statistical uncertainty originating from the small sample size in the sideband regions used for making this estimate. We assign a 50% uncertainty to the real Υ + fake W/Z background based on the application of uncertainties associated with the measured jet-to-lepton misidentification rates.

Table C.3: Systematic uncertainties associated with the signal expectation.

Luminosity	6%
Υ muon identification	4%
High- $E_T(p_T)$ lepton identification	1%
High- $E_T(p_T)$ lepton trigger efficiency	1%
PDFs	12%
LDMEs	6%
Double parton scattering	15%
Event selection efficiency	3%
Total	22%

C.7 Results

Table C.4 summarizes the predicted signal and background contributions, and number of observed events for each of the search samples using data from 9.4 fb^{-1} of integrated luminosity at CDF. We observe one $\Upsilon + (W \rightarrow \ell\nu)$ candidate with a total expected background of 1.2 ± 0.5 events. In the observed $\Upsilon + (W \rightarrow \ell\nu)$ candidate the electron has $p_T = 27.4\text{ GeV}$, and the two muons with an invariant mass in the $\Upsilon(1S)$ region have $p_{T\text{S}}$ of $3.8\text{ GeV}/c$ and $7.1\text{ GeV}/c$. The \cancel{E}_T in this event is 30.8 GeV , which, with the electron gives a transverse mass of $58.1\text{ GeV}/c^2$.

We also observe one $\Upsilon + (Z \rightarrow \ell\ell)$ candidate with a total expected background of 0.1 ± 0.1 events. An event display of the $\Upsilon + (Z \rightarrow \ell\ell)$ candidate is shown in Fig. C.5. This is the first observed $\Upsilon + (Z \rightarrow \ell\ell)$ candidate event at the Tevatron. The two high- p_T muon candidates have an invariant mass of $88.6\text{ GeV}/c^2$, and the two low- p_T

muon candidates have an invariant mass of $9.26 \text{ GeV}/c^2$. All muon candidates are detected in the central region of the detector. The invariant mass of all four muon candidates is $98.4 \text{ GeV}/c^2$. Further properties of the muons in this event are given in Table C.6.

Table C.4: Summary of signal expectation (N_{sig}), background estimations (N_{bg}), and observed events (N_{obs}).

	$\Upsilon + W \rightarrow e\nu$	$\Upsilon + W \rightarrow \mu\nu$	$\Upsilon + W \rightarrow \ell\nu$	$\Upsilon + Z \rightarrow ee$	$\Upsilon + Z \rightarrow \mu\mu$	$\Upsilon + Z \rightarrow \ell\ell$
N_{sig}	0.019 ± 0.004	0.014 ± 0.003	0.034 ± 0.007	0.0048 ± 0.0011	0.0037 ± 0.0008	0.0084 ± 0.0018
N_{bg} (fake Υ)	0.7 ± 0.4	0.4 ± 0.3	1.1 ± 0.5	0.07 ± 0.07	0.04 ± 0.04	0.1 ± 0.1
N_{bg} (fake W/Z)	0.06 ± 0.04	0	0.06 ± 0.04	0	0	0
N_{bg} ($\Upsilon + Z$)	0.0006 ± 0.0001	0.0033 ± 0.0007	0.0039 ± 0.0009			
N_{bg} (total)	0.8 ± 0.4	0.4 ± 0.3	1.2 ± 0.5	0.07 ± 0.07	0.04 ± 0.04	0.1 ± 0.1
N_{obs}	0	1	1	0	1	1

Having observed no clear evidence for a $\Upsilon + W/Z$ signal, we set 90% C.L. and 95% C.L. upper limits on the ΥW and ΥZ production cross sections. We use the branching fractions of $\Upsilon \rightarrow \mu\mu$ (0.0248), $W \rightarrow \ell\nu$ (0.107), and $Z \rightarrow \ell\ell$ (0.0336) from Ref. [96]. A Bayesian technique is employed, described in Ref. [97], where the posterior probability density was constructed from the joint Poisson probability of observing the data in each vector boson decay channel, integrating over the uncertainties of the normalization parameters using Gaussian prior-probability densities. A non-negative constant prior in the signal rate was assumed. The expected and observed limits are shown in Table C.5 and compared to the observed limits from the CDF Run I analysis [81].

C.8 Conclusions

We search for $\Upsilon + W/Z$ production using the leptonic decay channels of the vector bosons and dimuon decay channel of the Υ . The search utilizes the full CDF Run II data set. Having observed no significant excess of events with respect to standard

Table C.5: Cross-section upper limits for ΥW and ΥZ production. This analysis utilizes 9.4 fb^{-1} of CDF Run II data. The CDF Run I analysis utilized 83 pb^{-1} of CDF Run I data.

	ΥW	ΥZ
90% C.L. expected limit (pb)	4.4	9.9
90% C.L. observed limit (pb)	4.4	16
95% C.L. expected limit (pb)	5.6	13
95% C.L. observed limit (pb)	5.6	21
Run I 95% C.L. observed limit (pb)	93	101

Table C.6: Kinematic properties of the muons in the observed $\Upsilon + Z$ candidate displayed in Fig. C.5. Isolation is defined as the sum of calorimeter energy in a cone of $\Delta R = 0.4$ around the muon candidate as a fraction of the muon momentum. The longitudinal position z_0 (along the beam line) of each muon candidate suggest all muons come from the same primary $p\bar{p}$ interaction vertex.

	muon 1	muon 2	muon 3	muon 4
p_x (GeV/c)	-34.6	34.8	0.823	-0.106
p_y (GeV/c)	-14.0	13.8	-6.25	3.29
p_z (GeV/c)	-39.2	10.6	-2.20	-2.56
E (GeV)	54.2	39.0	6.68	4.17
p_T (GeV/c)	37.4	37.5	6.3	3.3
η	-0.92	0.28	-0.34	-0.72
ϕ (rads)	-2.76	0.38	-1.44	1.60
Isolation	0.03	0.00	0.64	0.35
z_0 (cm)	41.2	41.1	41.0	41.3

model predictions, we set 95% C.L. upper limits on the $\Upsilon + W/Z$ cross sections. The limits are $\sigma(p\bar{p} \rightarrow \Upsilon W) < 5.6 \text{ pb}$ and $\sigma(p\bar{p} \rightarrow \Upsilon Z) < 21 \text{ pb}$ which are the most stringent bounds on these processes to date. Under the assumption that potential non-SM physics contributions to the $\Upsilon + W/Z$ final state do not significantly impact the kinematic properties of events, these limits can be interpreted as cross section (times branching ratio to $\Upsilon + W/Z$) limits on non-SM physics processes contributing to this final state. Potential non-standard-model heavy particles decaying to $\Upsilon + W/Z$

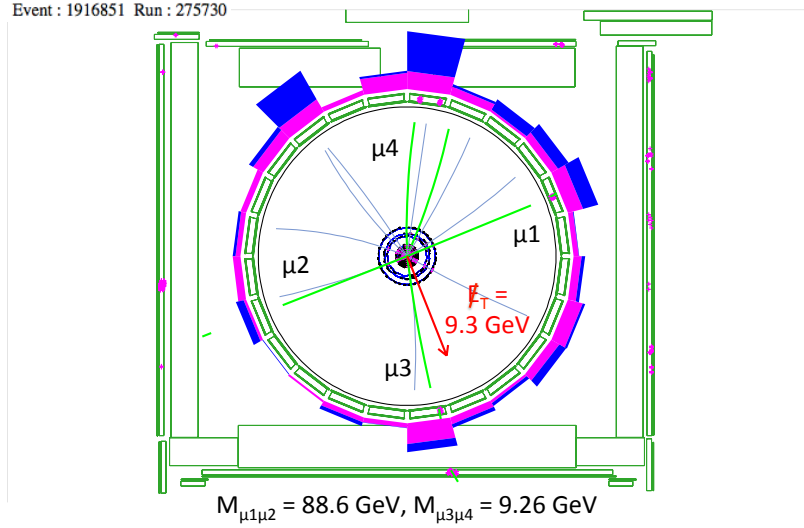


FIGURE C.5: Event display of the observed ΥZ candidate, showing the muon candidates identified from the Υ and Z decays. The view is in the transverse ($r - \phi$) plane of the detector, where the inner core is the silicon vertex tracker, and the larger circle is the outer radius of the drift chamber where the tracks of charged particle with $p_T > 1.5 \text{ GeV}/c$ are shown. The height of the surrounding pink and blue “towers” is roughly proportional to the energy deposits in the electromagnetic and hadronic compartments of the calorimeter, from which the H_T magnitude and direction (red arrow) is computed. Measurement-hits in the muon chambers are shown in the outermost box-shaped structure.

final states are likely to result in leptons that are more central than those from standard-model $\Upsilon + W/Z$ production and therefore provide higher signal acceptance. Hence, the limits presented here can be considered as conservative limits on such processes.

Bibliography

- [1] ATLAS Collaboration, G. Aad et al., *Measurement of the cross section for top-quark pair production in pp collisions at $\sqrt{s} = 7$ TeV with the ATLAS detector using final states with two high- pt leptons*, JHEP **1205** (2012) 059, [arXiv:1202.4892 \[hep-ex\]](https://arxiv.org/abs/1202.4892).
- [2] ATLAS Collaboration, G. Aad et al., *Measurement of the top quark mass in the $t\bar{t} \rightarrow \text{lepton} + \text{jets}$ and $t\bar{t} \rightarrow \text{dilepton}$ channels using $\sqrt{s} = 7$ TeV ATLAS data*, Eur. Phys. J. C **75** (2015) 330, [arXiv:1503.05427 \[hep-ex\]](https://arxiv.org/abs/1503.05427).
- [3] R. S. Chivukula, S. B. Selipsky, and E. H. Simmons, *Nonoblique effects in the $Zb\bar{b}$ vertex from ETC dynamics*, Phys. Rev. Lett. **69** (1992) 575, [arXiv:hep-ph/9204214](https://arxiv.org/abs/hep-ph/9204214).
- [4] R. Chivukula, E. H. Simmons, and J. Terning, *A Heavy top quark and the $Zb\bar{b}$ vertex in noncommuting extended technicolor*, Phys. Lett. B **331** (1994) 383, [arXiv:hep-ph/9404209](https://arxiv.org/abs/hep-ph/9404209).
- [5] J. M. Campbell and R. K. Ellis, *$t\bar{t}W^\pm$ production and decay at NLO*, JHEP **07** (2012) 052, [arXiv:1204.5678](https://arxiv.org/abs/1204.5678).
- [6] M. Garzelli, A. Kardos, C. Papadopoulos, and Z. Trócsányi, *$t\bar{t}W^\pm$ and $t\bar{t}Z$ hadroproduction at NLO accuracy in QCD with Parton Shower and Hadronization effects*, JHEP **11** (2012) 056, [arXiv:1208.2665](https://arxiv.org/abs/1208.2665).
- [7] https://en.wikipedia.org/wiki/Standard_Model.
- [8] Particle Data Group Collaboration, J. Beringer et al., *Review of Particle Physics (RPP)*, Phys. Rev. D**86** (2012) 010001.
- [9] Y. F. et al. (Super-Kamiokande Collaboration), *Evidence for Oscillation of Atmospheric Neutrinos*, Phys. Rev. Lett. **81** (1998) 1562–1567.

- [10] Q. R. A. et al. (SNO Collaboration), *Direct Evidence for Neutrino Flavor Transformation from Neutral-Current Interactions in the Sudbury Neutrino Observatory*, Phys. Rev. Lett. **89** (2002) 011301.
- [11] A. Martin, W. Stirling, R. Thorne, G. Watt, *Parton distributions for the LHC*, Eur. Phys. J. C **63** 189 (2009).
- [12] D. Stump, J. Huston, J. Pumplin, W.-K. Tung, H. Lai, et al., *Inclusive jet production, parton distributions, and the search for new physics*, JHEP **0310** (2003) 046, [arXiv:hep-ph/0303013](https://arxiv.org/abs/hep-ph/0303013) [hep-ph].
- [13] F. Abe et al. (CDF Collaboration), *Observation of top quark production in $p\bar{p}$ collisions*, Phys. Rev. Lett. **74** (1995) 2626, [arXiv:hep-ex/9503002](https://arxiv.org/abs/hep-ex/9503002).
- [14] S. Abachi et al. (D0 Collaboration), *Observation of the top quark*, Phys. Rev. Lett. **74** (1995) 2632, [arXiv:hep-ex/9503003](https://arxiv.org/abs/hep-ex/9503003).
- [15] DONUT Collaboration, K. Kodama et al., *Observation of tau neutrino interactions*, Phys. Lett. **B504** (2001) 218–224, [arXiv:hep-ex/0012035](https://arxiv.org/abs/hep-ex/0012035) [hep-ex].
- [16] ATLAS Collaboration, G. Aad et al., *Observation of a new particle in the search for the Standard Model Higgs boson with the ATLAS detector at the LHC*, Phys. Lett. **B716** (2012) 1–29, [arXiv:1207.7214](https://arxiv.org/abs/1207.7214) [hep-ex].
- [17] CMS Collaboration, S. Chatrchyan et al., *Observation of a new boson at a mass of 125 GeV with the CMS experiment at the LHC*, Phys. Lett. **B716** (2012) 30–61, [arXiv:1207.7235](https://arxiv.org/abs/1207.7235) [hep-ex].
- [18] G. Steigman and M. S. Turner, *Cosmological Constraints on the Properties of Weakly Interacting Massive Particles*, Nucl. Phys. **B253** (1985) 375.
- [19] S. Drell and T.-M. Yan, *Massive Lepton Pair Production in Hadron-Hadron Collisions at High-Energies*, Phys. Rev. Lett. **25** (1970) 316–320.
- [20] K. Melnikov and F. Petriello, *Electroweak gauge boson production at hadron colliders through $\mathcal{O}(\alpha_S^2)$* , Phys. Rev. **D 74** (2006) 114017, [arXiv:hep-ph/0609070](https://arxiv.org/abs/hep-ph/0609070).
- [21] J. M. Campbell, R. K. Ellis, and C. Williams, *Vector boson pair production at the LHC*, JHEP **1107** (2011) 018, [arXiv:1105.0020](https://arxiv.org/abs/1105.0020) [hep-ph].

- [22] M. Cacciari et al., *Top-pair production at hadron colliders with next-to-next-to-leading logarithmic soft-gluon resummation*, Phys. Lett. **B710** (2012) 612–622, [arXiv:1111.5869 \[hep-ph\]](https://arxiv.org/abs/1111.5869).
- [23] M. Czakon, P. Fiedler, and A. Mitov, *Total Top-Quark Pair-Production Cross Section at Hadron Colliders Through $O(\frac{4}{S})$* , Phys. Rev. Lett. **110** (2013) 252004, [arXiv:1303.6254 \[hep-ph\]](https://arxiv.org/abs/1303.6254).
- [24] N. Kidonakis, *Two-loop soft anomalous dimensions for single top quark associated production with a W - or H -*, Phys. Rev. **D82** (2010) 054018, [arXiv:1005.4451 \[hep-ph\]](https://arxiv.org/abs/1005.4451).
- [25] LHC Higgs Cross Section Working Group Collaboration, S. Dittmaier et al., *Handbook of LHC Higgs Cross Sections: 1. Inclusive Observables*, [arXiv:1101.0593](https://arxiv.org/abs/1101.0593).
- [26] J. Campbell, R. K. Ellis, and R. Rentsch, *Single top production in association with a Z boson at the LHC*, Phys. Rev. **D87** (2013) 114006, [arXiv:1302.3856 \[hep-ph\]](https://arxiv.org/abs/1302.3856).
- [27] J. Alwall, P. Demin, S. de Visscher, R. Frederix, M. Herquet, et al., *MadGraph/MadEvent v4: the new web generation*, JHEP **0709** (2007) 028, [arXiv:0706.2334](https://arxiv.org/abs/0706.2334).
- [28] T. Gleisberg, S. Hoeche, F. Krauss, M. Schonherr, S. Schumann, F. Siegert, J. Winter, *Event generation with SHERPA 1.1*, JHEP **0902** (2009) 007.
- [29] L. Evans and P. Bryant, *LHC Machine*, JINST **3** (2008) S08001.
- [30] ATLAS Collaboration, G. Aad et al., *The ATLAS Experiment at the CERN Large Hadron Collider*, JINST **3** (2008) S08003.
- [31] ATLAS Collaboration, G. Aad et al., *The ATLAS Simulation Infrastructure*, Eur. Phys. J. **C70** (2010) 823–874, [arXiv:1005.4568 \[physics.ins-det\]](https://arxiv.org/abs/1005.4568).
- [32] *Monte Carlo Generators*. 2006. [arXiv:hep-ph/0611247 \[hep-ph\]](https://arxiv.org/abs/hep-ph/0611247).
- [33] M. Mangano, M. Moretti, F. Piccinini, R. Pittau, A. Polosa, *ALPGEN, a generator for hard multiparton processes in hadronic collisions*, JHEP 07 001 (2003).
- [34] S. Frixione and B. Webber, *Matching NLO QCD Computations and Parton Shower Simulations*, JHEP 0206:029 (2002).

- [35] P. Nason, *A new method for combining NLO QCD computations with parton shower simulations*, JHEP **11** 040 (2004).
- [36] S. Mrenna, T. Sjostrand, P. Skands, *Pythia 6.4 physics and manual*, JHEP 05 0265 (2006).
- [37] G. Corcella, I. Knowles, G. Marchesini, S. Moretti, K. Odagiri, P. Richardson, M. Seymour, B. Webber, *HERWIG 6: an Event Generator for Hadron Emission Reactions with Interfering Gluons (including supersymmetric processes)*, JHEP 0101 010 (2001).
- [38] B. Andersson, G. Gustafson, G. Ingelman, and T. Sjostrand, *Parton Fragmentation and String Dynamics*, Phys.Rept. **97** (1983) 31–145.
- [39] B. Webber, *A QCD Model for Jet Fragmentation Including Soft Gluon Interference*, Nucl. Phys. **B238** (1984) 492.
- [40] S. Jadach, Z. Was, R. Decker, and J. H. Kuhn, *The tau decay library TAUOLA: Version 2.4*, Comput. Phys. Commun. **76** (1993) 361–380.
- [41] E. Barberio, B. van Eijk, and Z. Was, *PHOTOS: A Universal Monte Carlo for QED radiative corrections in decays*, Comput. Phys. Commun. **66** (1991) 115–128.
- [42] GEANT4 Collaboration, S. Agostinelli et al., *GEANT4: A Simulation toolkit*, Nucl. Instrum. Meth. **A506** (2003) 250–303.
- [43] J. Butterworth, J. Forshaw, and M. Seymour, *Multiparton interactions in photoproduction at HERA*, Zeit. Phys. **C 72** (1996) 637, [arXiv:hep-ph/9601371](https://arxiv.org/abs/hep-ph/9601371).
- [44] ATLAS Collaboration, *The simulation principle and performance of the ATLAS fast calorimeter simulation FastCaloSim*, ATL-PHYS-PUB-2010-013, 2010. <https://cds.cern.ch/record/1300517>.
- [45] ATLAS Collaboration, *ATLAS tunes of Pythia 6 and Pythia 8 for MC11*, ATL-PHYS-PUB-2011-009, July 2011.
- [46] H.-L. Lai, M. Guzzi, J. Huston, Z. Li, P. M. Nadolsky, et al., *New parton distributions for collider physics*, Phys. Rev. **D82** (2010) 074024, [arXiv:1007.2241 \[hep-ph\]](https://arxiv.org/abs/1007.2241).

[47] P. Z. Skands, *Tuning Monte Carlo Generators: The Perugia Tunes*, Phys. Rev. **D 82** (2010) 074018, [arXiv:1005.3457](https://arxiv.org/abs/1005.3457).

[48] G. Bevilacqua, M. Czakon, M. V. Garzelli, A. van Hameren, A. Kardos, C. G. Papadopoulos, R. Pittau, and M. Worek, *HELAC-NLO*, Comput. Phys. Commun. **184** (2013) 986–997, [arXiv:1110.1499](https://arxiv.org/abs/1110.1499) [hep-ph].

[49] ATLAS Collaboration, *Summary of ATLAS Pythia 8 tunes*, ATLAS-PHYS-PUB-2012-003, August 2012.

[50] T. Cornelissen, M. Elsing, S. Fleischmann, W. Liebig, E. Moyse, and A. Salzburger, *Concepts, Design and Implementation of the ATLAS New Tracking (NEWT)*, Tech. Rep. ATL-SOFT-PUB-2007-007, CERN, Geneva, Mar, 2007. <https://cds.cern.ch/record/1020106>.

[51] ATLAS Collaboration, *Performance of primary vertex reconstruction in proton-proton collisions at $\sqrt{s} = 7$ TeV in the ATLAS experiment*, Tech. Rep. ATLAS-CONF-2010-069, CERN, Geneva, Jul, 2010. [http://cds.cern.ch/record/1281344](https://cds.cern.ch/record/1281344).

[52] ATLAS Collaboration, *Electron efficiency measurements with the ATLAS detector using the 2012 LHC proton-proton collision data*, Tech. Rep. ATLAS-CONF-2014-032, CERN, Geneva, Jun, 2014. [http://cds.cern.ch/record/1706245](https://cds.cern.ch/record/1706245).

[53] ATLAS Collaboration, *Measurement of the muon reconstruction performance of the ATLAS detector using 2011 and 2012 LHC proton-proton collision data*, Eur. Phys. J. **C74** (2014) 3130, [arXiv:1407.3935](https://arxiv.org/abs/1407.3935) [hep-ex].

[54] ATLAS Collaboration, *Jet energy measurement and its systematic uncertainty in proton–proton collisions at $\sqrt{s} = 7$ TeV with the ATLAS detector*, Eur. Phys. J. **C 75** (2015) 17, [arXiv:1406.0076](https://arxiv.org/abs/1406.0076).

[55] M. Cacciari, G. P. Salam, and G. Soyez, *The anti- k_t jet clustering algorithm*, JHEP **0804** (2008) 063, [arXiv:0802.1189](https://arxiv.org/abs/0802.1189) [hep-ph].

[56] ATLAS Collaboration, *Commissioning of the ATLAS high performance b-tagging algorithms in the 7 TeV collision data*, ATLAS-CONF-2011-102, 2011. [http://cdsweb.cern.ch/record/1369219](https://cdsweb.cern.ch/record/1369219).

[57] ATLAS Collaboration, *Calibration of the performance of b-tagging for c and light-flavour jets in the 2012 ATLAS data*, ATLAS-CONF-2014-046, 2014. [http://cdsweb.cern.ch/record/1741020](https://cdsweb.cern.ch/record/1741020).

[58] *Calibration of b-tagging using dileptonic top pair events in a combinatorial likelihood approach with the ATLAS experiment*, Tech. Rep. ATLAS-CONF-2014-004, CERN, Geneva, Feb, 2014.

[59] ATLAS Collaboration, G. Aad et al., *Performance of Missing Transverse Momentum Reconstruction in Proton-Proton Collisions at 7 TeV with ATLAS*, Eur. Phys. J. **C72** (2012) 1844, [arXiv:1108.5602](https://arxiv.org/abs/1108.5602) [hep-ex].

[60] ATLAS Collaboration, *Electron and photon reconstruction and identification in ATLAS: expected performance at high energy and results at 900 GeV*, Tech. Rep. ATLAS-CONF-2010-005, CERN, Geneva, Jun, 2010.
<https://cds.cern.ch/record/1273197>.

[61] ATLAS Collaboration, *Tau Reconstruction and Identification Performance in ATLAS*, Tech. Rep. ATLAS-CONF-2010-086, CERN, Geneva, Oct, 2010.
[http://cds.cern.ch/record/1298857](https://cds.cern.ch/record/1298857).

[62] CMS Collaboration, V. Khachatryan et al., *Measurement of top quark-antiquark pair production in association with a W or Z boson in pp collisions at $\sqrt{s} = 8$ TeV*, Eur. Phys. J. **C74** (2014) no. 9, 3060, [arXiv:1406.7830](https://arxiv.org/abs/1406.7830) [hep-ex].

[63] ATLAS Collaboration, *Measurements of normalized differential cross-sections for $t\bar{t}$ production in pp collisions at $\sqrt{s} = 7$ TeV using the ATLAS detector*, Phys. Rev. **D 90** (2014) 072004, [arXiv:1407.0371](https://arxiv.org/abs/1407.0371) [hep-ex].

[64] ATLAS Collaboration, *Measurement of the production cross section of jets in association with a Z boson in pp collisions at $\sqrt{s} = 7$ TeV with the ATLAS detector*, JHEP **07** (2013) 032, [arXiv:1304.7098](https://arxiv.org/abs/1304.7098).

[65] Phi-T GmbH, *NeuroBayes package*, <http://neurobayes.phi-t.de/>.

[66] ATLAS Collaboration, *Measurement of the top quark-pair production cross section with ATLAS in pp collisions at $\sqrt{s} = 7$ TeV*, Eur. Phys. J. **C71** (2011) 1577, [arXiv:1012.1792](https://arxiv.org/abs/1012.1792).

[67] ATLAS Collaboration, G. Aad et al., *Improved luminosity determination in pp collisions at $\sqrt{s} = 7$ TeV using the ATLAS detector at the LHC*, [arXiv:1302.4393](https://arxiv.org/abs/1302.4393) [hep-ex].

[68] ATLAS Collaboration, G. Aad et al., *Electron and photon energy calibration with the ATLAS detector using LHC Run 1 data*, Eur. Phys. J. **C74** (2014) 3071, [arXiv:1407.5063](https://arxiv.org/abs/1407.5063) [hep-ex].

[69] *Jet energy resolution and selection efficiency relative to track jets from in-situ techniques with the ATLAS Detector Using Proton-Proton Collisions at a Center of Mass Energy $\sqrt{s} = 7$ TeV*, Tech. Rep. ATLAS-CONF-2010-054, CERN, Geneva, Jul, 2010.

[70] ATLAS Collaboration, G. Aad et al., *Jet energy resolution in proton-proton collisions at $\sqrt{s} = 7$ TeV recorded in 2010 with the ATLAS detector*, Eur. Phys. J. **C73** (2013) 2306, [arXiv:1210.6210 \[hep-ex\]](https://arxiv.org/abs/1210.6210).

[71] R. D. Ball, V. Bertone, S. Carrazza, C. S. Deans, L. Del Debbio, et al., *Parton distributions with LHC data*, Nucl. Phys. **B 867** (2013) 244–289, [arXiv:1207.1303](https://arxiv.org/abs/1207.1303).

[72] M. Botje, J. Butterworth, A. Cooper-Sarkar, A. de Roeck, J. Feltesse, et al., *The PDF4LHC Working Group Interim Recommendations*, [arXiv:1101.0538 \[hep-ph\]](https://arxiv.org/abs/1101.0538).

[73] G. Cowan, K. Cranmer, E. Gross, and O. Vitells, *Asymptotic formulae for likelihood-based tests of new physics*, Eur. Phys. J. **C 71** (2011) 1554, Erratum: **C 73** (2013) 2501, [arXiv:1007.1727](https://arxiv.org/abs/1007.1727).

[74] C. K, G. Lewis, L. Moneta, A. Shibata, and W. Verkerke, *HistFactory: A tool for creating statistical models for use with RooFit and RooStats*, Tech. Rep. CERN-OPEN-2012-016, Jan, 2012. <https://cds.cern.ch/record/1456844/>.

[75] W. Verkerke and D. Kirkby, *The RooFit toolkit for data modeling*, [arXiv:physics/0306116](https://arxiv.org/abs/physics/0306116).

[76] L. Moneta, K. Belasco, K. Cranmer, S. Kreiss, A. Lazzaro, D. Piparo, G. Schott, W. Verkerke, and M. Wolf, *The RooStats Project*, [arXiv:1009.1003](https://arxiv.org/abs/1009.1003).

[77] ATLAS Collaboration, *Letter of Intent for the Phase-II Upgrade of the ATLAS Experiment*, Tech. Rep. CERN-LHCC-2012-022 LHCC-I-023, CERN, Geneva, Dec, 2012. <https://cds.cern.ch/record/1502664>.

[78] E. Braaten, J. Lee, and S. Fleming, Phys. Rev. D **60**, 091501 (1999).

[79] B. Gong, J. -P. Lansberg, C. Lorce, and J. Wang, J. High Energy Phys. 03 (2013) 115.

[80] P. Artoisenet, F. Maltoni, and T. Stelzer, J. High Energy Phys. 02 (2008) 102.

- [81] D. Acosta *et al.* (CDF Collaboration), Phys. Rev. Lett. **90**, 221803 (2003).
- [82] F. Abe *et al.* (CDF Collaboration), Nucl. Instrum. Methods A **271**, 387 (1988); D. E. Amidei *et al.* (CDF Collaboration), Nucl. Instrum. Methods A **350**, 73 (1994); F. Abe *et al.* (CDF Collaboration), Phys. Rev. D **52**, 4784 (1995); S. Cihangir, G. Gillespie, H. Gonzalez, S. Gonzalez, C. Grimm, M. Guerra, T. Hawke, and M. Hrycyk *et al.*, Nucl. Instrum. Methods A **360**, 137 (1995); R. Blair *et al.* (CDF Collaboration), FERMILAB-DESIGN-1996-01.
- [83] J. Alwall, P. Demin, S. de Visscher, R. Frederix, M. Herquet, F. Maltoni, T. Plehn, D. L. Rainwater, and T. Stelzer, J. High Energy Phys. 09 (2007) 028.
- [84] E. Braaten, S. Fleming, and A. K. Leibovich, Phys. Rev. D **63**, 094006 (2001).
- [85] R. Sharma and I. Vitev, Phys. Rev. C **87**, 044905 (2013).
- [86] T. Sjostrand, S. Mrenna, and P. Z. Skands, J. High Energy Phys. 05 (2006) 026.
- [87] R. Brun, F. Carminati, and S. Giani, CERN-W5013.
- [88] E. Gerchtein and M. Paulini, eConf C **0303241**, TUMT005 (2003).
- [89] D. Acosta *et al.* (CDF Collaboration), Nucl. Instrum. Methods A **461**, 540 (2001).
- [90] T. Aaltonen *et al.* (CDF Collaboration), Phys. Rev. D **88**, 052012 (2013).
- [91] A. Abulencia *et al.* (CDF Collaboration), J. Phys. G **34**, 2457 (2007).
- [92] T. Aaltonen *et al.* (CDF Collaboration), Phys. Rev. Lett. **108**, 151802 (2012).
- [93] J. Pumplin, D. R. Stump, J. Huston, H. L. Lai, P. M. Nadolsky, and W. K. Tung, J. High Energy Phys. 07 (2002) 012.
- [94] A. D. Martin, W. J. Stirling, R. S. Thorne, and G. Watt, Eur. Phys. J. C **63**, 189 (2009).
- [95] ATLAS Collaboration, J. High Energy Phys. 04 (2014) 172.
- [96] J. Beringer *et al.* (Particle Data Group), Phys. Rev. D **86**, 010001 (2012).
- [97] T. Aaltonen *et al.* (CDF Collaboration), Phys. Rev. D **82**, 112005 (2010).

Biography

Chen Zhou was born in Fuzhou, China on June 22, 1988. He attended Peking University and received his Bachelor degree in Physics in 2010. In the same year, he moved to the United States and started his Ph.D. studies at Duke University. He worked on experimental particle physics, under the direction of Prof. Mark Kruse.